Multiplexed Matrix-Assisted Laser Desorption/Ionization-Mass Spectrometry Imaging (MALDI-MSI) Biomarker Discovery

by

Teesha Crystal Luehr
Bachelor of Science (Honours), University of British Columbia, 2015

A Thesis Submitted in Partial Fulfillment
of the Requirements for the Degree of

MASTER OF SCIENCE

in the Department of Biochemistry & Microbiology

University of Victoria

Supervisory Committee

Multiplexed Matrix-Assisted Laser Desorption/Ionization-Mass Spectrometry Imaging (MALDI-MSI) Biomarker Discovery

by

Teesha Crystal Luehr
Bachelor of Science Honours in Chemistry, University of British Columbia, 2015

Supervisory Committee

Dr. Christoph H. Borchers, Department of Biochemistry and Microbiology
Supervisor

Dr. Caren C. Helbing, Department of Biochemistry and Microbiology
Departmental Member

Dr. Ben F. Koop, Department of Biology
Outside Member

Abstract

Supervisory Committee
Dr. Christoph H. Borchers, Department of Biochemistry and Microbiology
Supervisor
Dr. Caren C. Helbing, Department of Biochemistry and Microbiology
Departmental Member
Dr. Ben F. Koop, Department of Biology
Outside Member

The work presented herein is a method optimization for biomolecule detection and identification using Matrix-Assisted Laser Desorption/Ionization-Mass Spectrometry Imaging (MALDI-MSI). MALDI-MSI is a unique form of mass spectrometry that is highly multiplexed; it can simultaneously retain location information of the mass of multiple ions, allowing for correlation of morphology or pathology to reconstructed ion heat maps. There were three main objectives for the research - 1) A method optimization of sample preparation techniques for bottom-up proteomic MALDI-MSI was performed. This included the optimization of tissue wash steps, trypsin digestion incubation times, and matrix deposition techniques. The results included identifying the appropriate pH for the wash steps to optimize trypsin digestion, an overnight trypsin incubation to allow for complete digestion, and the inclusion of MCAEF – Matrix Coating Assisted by an Electric Field – during matrix coating for enhanced spectra. 2) An unbiased statistical data processing workflow for simultaneous processing of multiple datasets was performed. This was done using a thyroid hormone treated tadpole dataset to gain insight into the metabolism of anuran metamorphosis. Results found included a finalized data processing workflow that detected 5000 metabolite features from five organs were detected in pre-metamorphic tadpoles. Of these detected metabolites, 136 were significantly affected upon exposure to thyroid hormone and 64 metabolites were putatively identified. 3) A sample preparation technique for metabolomic analysis of formalin-fixed paraffin embedded (FFPE) colorectal liver metastasis samples was performed. Results included the importance of using a high mass resolution mass spectrometer while emphasizing more appropriate use of fresh-frozen tissue sections for metabolomic analysis.

Table of Contents

List of Tables

List of Figures

List of Tables in Appendix

Dedication

I would like to take this opportunity to thank three people for their continued dedication and support during this research: 1) I would first like to say a special thank-you to my husband, Stephen Luehr. You inspire me to reach my greatest potential in life. Together we will reach the moon, and if not, we'll land somewhere in the stars. 2) Secondly, I would like to thank my 10-year old self. She was an amazingly dedicated young lady who always said she wanted to grow up to be wearing a lab coat and goggles. Here I am today, writing my Masters thesis and about to undertake a PhD, all in biochemistry. The momentum she began brewing has helped power me through the trials and tribulations of this graduate degree. 3) Last but never the least, I would like to thank the graduate students of BCMB. You have stood by my side and helped me grow into not only a stronger researcher, but a stronger person. I am grateful for the lessons learned, the laughs shared, and the drinks consumed! And of course, a quote that has helped me get through this thing we call life: If at first you don't succeed, laugh until you do.

List of Abbreviations

2-MBT - 2-mercaptobenzothiazol

3-HC - 3-hydroxycoumarin

9-AA - 9- aminoacridine

ACN - acetonitrile

ATT - 6-aza-2-thiothymine

BRCA - breast cancer 1 gene

CA125 - cancer 125 protein

CD - cold-inducible RNA binding protein

CEA - carcinoembryonic antigen

CHCA - α-cyano-4-hydroxycinnamic acid

CID - collision induced dissociation

DAN - 1,5-diaminonapthalene

DHAP - 2,5-dihydroxyacetophenone

DHB - 2,5-dihydroxybenzoic

DMAN - 1,8-bis(dimethyl-amino) naphthalene

DNA - deoxyribonucleic acid

DT - dithranol

DTT - dithiothreitol

ESI - Electrospray Ionization

FA - formic acid

FFPE - formalin-fixed and paraffin embedded

FTICR - Fourier transform ion cyclotron resonance

GO - Graphene oxide

H&E - hematoxylin & eosin

HB - hemoglobin

HCD - higher-energy collisional dissociation

HLA - Human Leukocyte Antigen

HPLC - high performance liquid chromatography

hr - hours

IAA - iodoacetamide

ITO - indium-tin oxide

LC MS/MS - Liquid Chromatography-Tandem Mass Spectrometry

LC/MS - liquid chromatography/mass spectrometry

LC-MS/MS - liquid chromatography tandem mass spectrometry

MAD - median absolute deviation

MALDI - matrix-assisted laser desorption/ionization

MALDI-MSI - Matrix-Assisted Laser Desorption/Ionization-Mass Spectrometry Imaging

MCAEF - Matrix Coating Assisted by an Electric Field

min - minutes

MWCNT - Multi-Walled Carbon Nanotube

NaOH - sodium hydroxide

NH_4HCO_3 - ammonium bicarbonate

NH_4OH - ammonium hydroxide

P1RS - phosphatase 1 regulatory subunit

PC - phosphatidylcholine

PCA - principle component analysis

PE - phosphatidylethanolamine

PG - phosphatidylglycerol

PI - phosphatidylinositol

PLS-DA - partial least squares-discriminant analysis

PS - phosphatidylserine

PSA - prostate specific antigen

RNA - ribonucleic acid

SA - sinapinic acid

secs - seconds

SM - sphingomyelin

SPE - solid phase extraction

T S/R - thiosulfate sulfurtransferase/rhodanese-like domain containing protein

T_4 - thyroxine

TFA - trifluoroacetic acid

TH - thyroid hormone

TOF - time-of-flight

Thesis Format and Manuscript Claims

The chapters in this thesis are presented in the format of a manuscript. The first chapter provides a general background and context for the thesis and introduces the rationale behind the thesis objectives. Chapters 2, 3, and 4 are written in a manuscript style and contain an Introduction, Materials & Methods, Results & Discussion, and Conclusions & Future Directions. The final chapter summarizes the data chapters.

Chapter One – Subheading MALDI-MSI: Baker, T.C., Han, J., Borchers, C.H., 2016. Recent advancements in matrix-assisted laser desorption/ionization mass spectrometry imaging. Current Opinion in Biotechnology 43, 62–69. doi:10.1016/j.copbio.2016.09.003 Baker, T.C. performed the literature review wrote the initial manuscript. Han, J. assisted in editing and finalizing the manuscript.

Chapter Three: Luehr, T.C., Koide, E.M., Wang, X., Han, J., Borchers, C.H., Helbing, C.C., 2017. Metabolomic insights into the effects of thyroid hormone on Rana catesbeiana metamorphosis using whole-body Matrix Assisted Laser Desorption/Ionization-Mass Spectrometry Imaging (MALDI-MSI). General and Comparative Endocrinology. Submitted to a special edition issue. Helbing, C.C. designed the exposures. Wang, X. acquired the data under supervision of Han J. Luehr, T.C. performed all data processing and statistical analysis. Luehr, T.C. created all figures and tables for the publication. Luehr, T.C. wrote the manuscript with assistance from Koide, E.M. and Helbing, C.C.

Chapter 1: Introduction

The Need for Biomarkers

Cancer has very few clinical biological markers for aiding in detection and diagnosis of the disease. These biological markers, can be in the form of genetic, transcriptomic, proteomic, and metabolomic biomarkers. Optimally, a biomarker or panel of biomarkers can distinguish minute differences between related diseases that may be difficult to diagnose by a medical practitioner.

The relationship between genetics, transcripts, proteins, and metabolites is diverse. There is an intimate relationship between genes and their eventually affected metabolites. It has been shown that a change in a single base pair in a gene can result in a 10,000 fold change in a metabolite's concentration in the human body.[1–3] Figure 1 shows a schematic diagram of the relationship between genomics, proteomics, and metabolomics. This figure depicts metabolites at the top of the pyramid, indicating its strong influence in our environment and within the human body. Metabolomics are extremely valuable in clinical diagnostics of diseases other than cancer. Examples that include the involvement of metabolites or metabolism include: diagnostic clinical assays (95%)[4], known drugs (89%)[5], drugs derived from pre-existing metabolites (50%)[6], and genetic disorders (30%)[7].

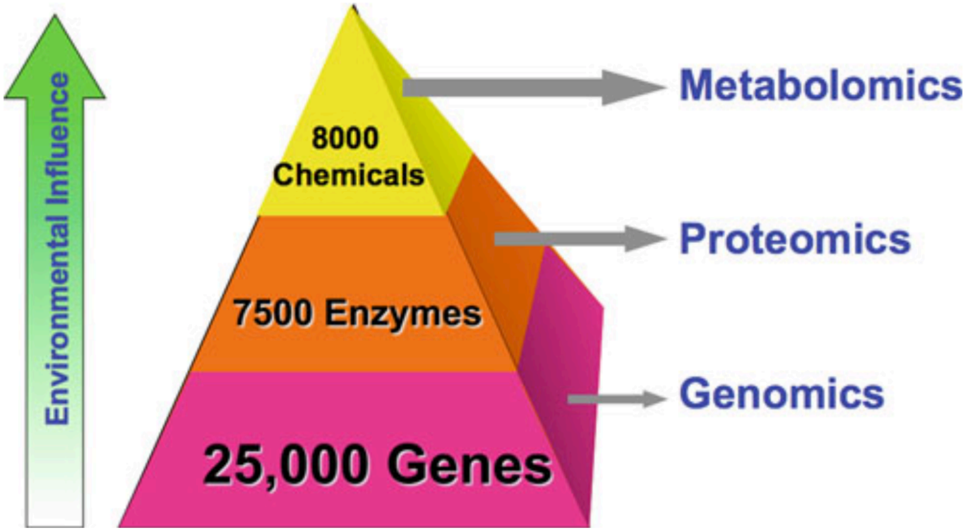

Figure 1 – Image depicting the relationship between genomics, proteomics, and metabolomics and their increasing environmental influence.[3] Image reprinted with permission.

The metabolomic profile is extremely sensitive to changes at the genomic and proteomic levels, resulting in the metabolome acting as a measurable phenotype within an organism (Figure 2). Understanding how the metabolome can give insights into cancer phenotype is a topic of recent research.[8–14] A very large review on lipid signalling, specifically phosphoinositides (PI), has been performed in the last 15 years on the universal impact of lipid signalling in eukaryotes.[15]

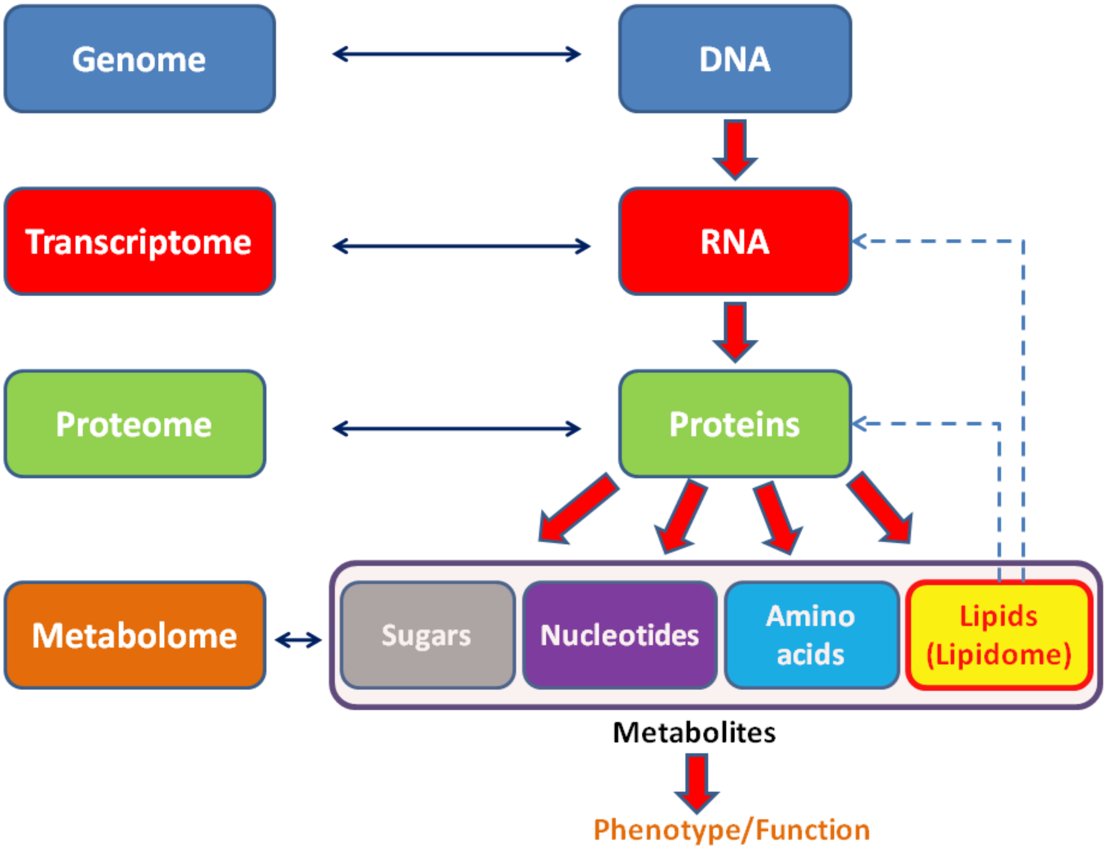

Figure 2 – A schematic diagram showing the relationship between the genome, transcriptome, proteome, and metabolome. The metabolome which is comprised of sugars, nucleotides, amino acids, and lipids, make up a phenotype of an organism. Retrieved from https://en.wikipedia.org/wiki/File:Metabolomics_schema.png

Genetic biomarkers are often used to determine the level of risk a patient has for developing a disease. For example, diabetes has multiple genes in the human leukocyte antigen (HLA) and a variable number of tandem repeats in the insulin gene have both been correlated with type 1 diabetes.[16] Breast cancer has mutations to the breast cancer 1 (BRCA1) and BRCA2 genes have served as risk factors and guides for targeted therapy.[17] Proteomic biomarkers, often detected in a patient's serum, are used for early diagnosis of diseases. Cancer 125 (CA125 - a mucin glycoprotein) concentration is monitored in serum to determine the risk of developing ovarian cancer and aids in determining effective therapy.[18] Metabolomic biomarkers are the key to connecting genetics to the visible phenotype. Recently, a set of metabolomic biomarkers has been proposed for predicting the risk of developing pancreatic cancer.[19] For example, prostaglandin E2 metabolites have been correlated with pancreatic cancer risk.[19] These metabolites were discovered as potential biomarkers due to their presence in the cyclooxygenase 2 pathway, which is known to be upregulated in pancreatic cancer.[19]

The biomarkers discussed above are examples of molecules that can be used in screening, diagnosis, prognosis, and targeted therapy choices of various diseases. However, the limited number of cancer biomarkers have poor specificity in distinguishing between sub-types of cancers. Cancer biomarkers require further study for development of effective clinical tests.

Mass Spectrometry

Mass spectrometry (MS) is an extremely dynamic tool that has the ability to detect nearly any type of compound in a biological sample.[20] MS can determine the exact masses of individual compound which can lead to an identification of the biomolecule.[21] An advantage of using mass spectrometry over other histological methods is that it can concurrently analyze a wide range of masses at the same time, creating a multiplexed analysis within a single tissue.[22] MS as a whole is a valuable technique for use in biomarker discovery and other untargeted methods aiming to characterize unknown compounds in biological samples.[23–28]

In general, mass spectrometers are comprised of three main components: an ionization source to create ions from the introduced sample, an analyzer to separate ions by certain mass characteristics and mass-to-charge ratios, and a detector for recording the abundancies of each mass-to-charge ratio.[29] The two most common ionization sources for proteomic MS analysis are electrospray ionization (ESI) and matrix-assisted laser desorption/ionization (MALDI).[29] The most essential component of a mass spectrometer is the mass analyzer.[29] There are four basic types of mass analyzers: ion trap, time-of-flight (TOF), quadrupole, and Fourier transform ion cyclotron resonance (FTICR) analyzers.

Matrix Assisted Laser Desorption/Ionization

MALDI is a type of mass spectrometry ionization source. MALDI was originally introduced in 1988 as an ionization source as a solution to ionize large macromolecules, such as intact proteins.[30] It is useful for proteins and other large compounds because it is considered a soft ionization source; the desorption and ionization process result in singly charged ions that typically aren’t fragmented from their original state. MALDI is unique to many other ionization techniques in that the sample is introduced to the instrument in a solid state.

As described in the name, this ionization source utilizes a matrix for aiding in both desorption and ionization of the molecules in the biological sample. A matrix is a compound that contains a chromophore that readily absorbs light at the wavelength of the laser.[31] The absorption of radiation causes a vibrational excitation of the matrix, leading to desorption of the matrix and neighbouring non-matrix compounds into the gas phase. Simultaneously, the excitation causes ions to be formed. Many different matrices have been experimented with, each with their own distinct benefits and negative attributes.

MALDI-Mass Spectrometry Imaging

Creation

Ten years after the creation of MALDI as an ionization source, Caprioli and his laboratory group applied this technique directly onto tissue sections for simultaneous *in-situ* detection of biomolecules, known as MALDI mass spectrometry imaging (MALDI-MSI).[32] This application spatially maps the concentration of an analyte by retaining location information on the tissue. A laser is rastered across a tissue section acquiring a full mass spectrum at each laser pixel (Figure 3). As a result, ion heat maps can be reconstructed for each tissue, displaying the relative concentration of an ion across the tissue section. The relative concentration information can be correlated to biology, morphology, histology, or pathology for a greater understanding of the biological context of each ion detected.

Methodology

A visual representation of a MALDI-MSI workflow can be found in Figure 3. In short, the general method applied during a MALDI-MSI experiment is as follows: a biological sample is thinly sliced (5-50 µm) with a microtome or cryostat, the tissue section is placed onto an electrically conductive surface such as a metal MALDI plate or a indium-tin oxide (ITO) coated glass slide. Depending on the type of compounds to be detected there may be some form of on-tissue sample preparation. For example, for detection of tryptic peptides an on-tissue digestion must be performed[33], or for detection of peptides or proteins a small molecule wash must be performed[34]. Next, the tissue is thinly coated with a matrix using a homogenous matrix sprayer or generator. Finally, the tissue is placed into the mass spectrometer for laser irradiation and detection. Each of these steps requires a wide range of optimization based on the tissue type, the class of compounds of interest, and the instrument being used.

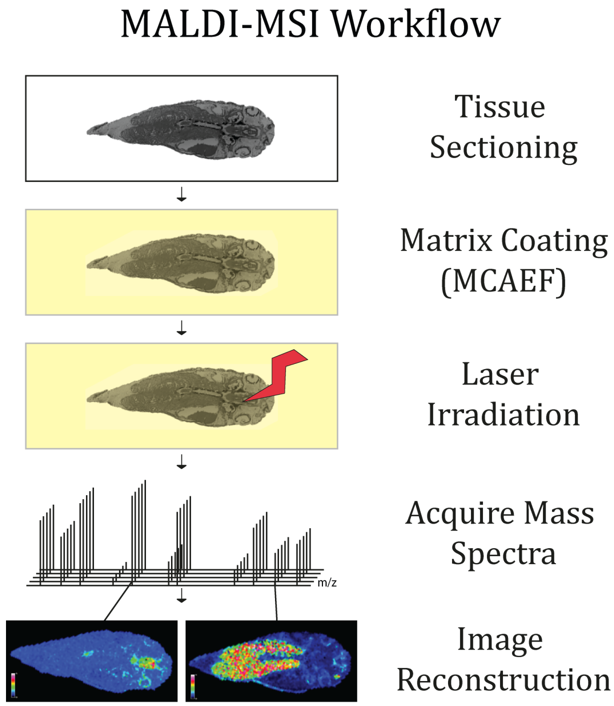

Figure 3 - MALDI-MSI sample preparation workflow including tissue sectioning, matrix coating, laser irradiation, spectral acquisition, and ion heat map image reconstruction.

Matrices

A matrix is used in MALDI to aid in increased desorption of analytes of interest from the conductive surface.[35] Matrices are commonly a UV-absorbing aromatic acids.[35] The compounds absorb the laser pulse resulting in desorption and energy transfer to the analyte for ionization.[35] A list of older, yet still commonly used matrices includes: 2,5-dihydroxybenzoic (DHB), α-cyano-4-hydroxycinnamic acid (CHCA), sinapinic acid (SA), 2-mercaptobenzothiazol (2-MBT), 9- aminoacridine (9-AA), and 2,5-dihydroxyacetophenone (DHAP). One of the most well studies areas of method optimization in MALDI-MSI is determination of which matrix to use for each MALDI-MSI experiment. A recent review in novel matrices was performed.[36] A summary of their application and uses can be found in Table 1. All matrices discussed in this table are for biological use in detecting and quantifying small molecules. This is a result of two major factors: 1) recent MALDI-MSI research has led to a large increased focus on small molecules including lipids and other metabolites, and as a result there is an increased amount of research on useful matrices and 2) older matrices that were optimal for detection of large molecules often had very complex background signals in the low molecular weight region (100-1000 m/z), which created difficulty in detecting small molecules occurring in the same region of the mass spectrum. One matrix of particular note is Quercetin.[37] This matrix was shown to have low volatility under vacuum, low matrix-related ions, and low threshold for laser desorption and ionization.[37] After initial publication, quercetin has been used in other experiments.[38–40] The final results of the experiment found that over 500 lipids were detected in positive and negative ionization mode in porcine adrenal glands, which was the largest number of lipids analyzed in a single MALDI-MSI study at the time of publication.[40]

Table 1 – A summary of recently published novel matrices for MALDI-MSI and their corresponding biological applications adapted from Baker et al. 2016.

(Ionization mode)-Matrix	Application	Instrument	Ref
(+/-)1,5-diaminonapthalene (DAN)	Higher sensitivity of ions in positive mode and rich spectra in negative mode for lipid analysis.	TOF/TOF	[41]
(+)1,7-bis-(4-hydroxy-3-methoxy-phenyl)-hepta-1,6-diene-3,5-dione (Curcumin)	Versatile and multipurpose analysis of pharmaceutical drugs, lipids, peptides, and proteins by promoting ionization	QTOF and HDMS	[42]
(-)1,8-bis(dimethyl-amino) naphthalene (DMAN)	A clean background spectra for analysis of metabolites in negative mode.	TOF/TOF	[43]
(-)1,8-bis(dimethylamino)naphthalene(DMAN)/9-aminoacridine (9-AA)	Reduced chemical noise, and no matrix-clusters for lipid analysis	TOF	[44]
(+)3-hydroxycoumarin (3-HC)/6-aza-2-thiothymine (ATT)	Low amount of background signals for analysis of drugs and single amino acids	TOF	[45]
(-)4-phenyl-α-cyanocinnamic acid amide	Small number of background peaks with matrix suppression for analysis of various lipid classes.	TOF/TOF	[46]
(+) Alternating Multilayer of (-) Graphene oxide (GO) and (+) Multi-Walled Carbon Nanotube (MWCNT)	Electrostatic charge between layers for removal of interference and contamination for analysis of small molecules	TOF	[47,48]

(+) Dithranol (DT)	Higher detection of endogenous lipids in positive mode over commonly used matrices.	FTICR	[49,50]
Quercetin	Lower number of matrix-related ions with a higher detection of lipids.	FTICR	[37]
(+) Two-Dimensional Graphene	Minimal background interference from elemental carbon.	FTICR	[51]

Matrix Deposition

Another area of MALDI-MSI examined in the review referenced above was novel matrix deposition techniques.[36] The overall quality of matrix deposition highly affects the spatial resolution in a MALDI-MSI experiment; matrix deposition needs to be uniform and create relatively small particle sizes for the laser irradiation to be effective. Commonly used matrix deposition techniques include matrix solution spray coating, matrix sublimation, and matrix pre-coating. Matrix spray coating involves a manual or automatic electronic or heat assisted spray generator to uniformly deposit the matrix on top of the tissue. This technique typically creates small, uniform particle sizes (10-15 µm).[52] Matrix sublimation has gained in use in laboratories for its ability to create low-µm particle sizes in a solvent-free manner.[53,54] Sublimation is compatible with all of the previously mentioned common matrices, but requires in-lab optimization of each matrix to achieve optimal performance.[55] The final matrix deposition technique is rather unique and different from typical matrix deposition techniques. The matrix is applied prior to the addition of a tissue section.[56,57] Sublimation reduced matrix deposition time and useful for both high molecular weight analytes such as proteins using SA and for low molecular weight analytes such as lipids and peptides using DHB.[56]

Matrix Coating Assisted by an Electric Field

A novel matrix deposition technique was developed in the Borchers laboratory in 2015: Matrix Coating Assisted by an Electric Field (MCAEF).[38] A diagram of the proposed mechanism can be found in Figure 4. This technique shows a significant increase in both the total number of analytes detected in a MALDI-MSI experiment and the signal to noise ratio of those analytes. This is highly beneficial for untargeted experiments that are aiming to detect large number of analytes. The original proof-of-concept experiment was performed on rat brain and detected and identified 648 lipids in both positive and negative mode as compared to only 344 lipids in both positive and negative mode without MCAEF. In addition, 232 proteins were detected in positive mode as compared to only 199 proteins in positive mode without MCAEF. This technique has been further applied to human prostate cancer for use in intact protein biomarker discovery. A total of 17 proteins have been detected and determined to have significantly different distribution patterns between the cancerous and non-cancerous tissue regions.[58]

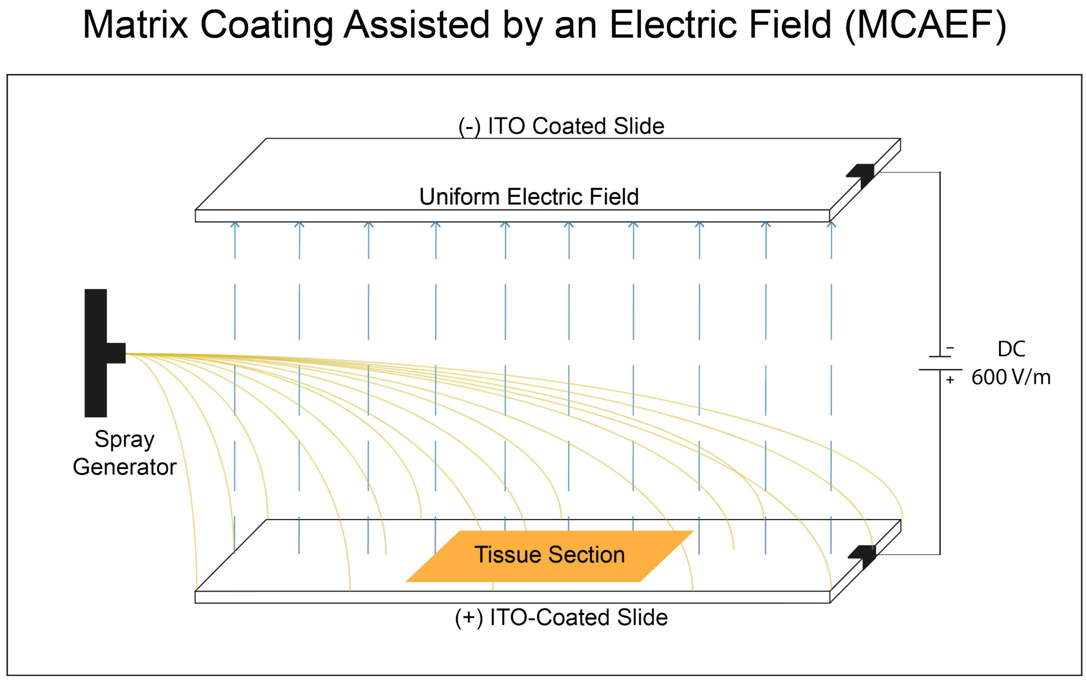

Figure 4 – A diagram of the proposed mechanism of the MCAEF technique developed and used in the Borchers laboratory. Two electrically conductive glass slides facing each other have an applied voltage (600V/m) creating a uniform electric field. This field causes a micro-extraction of charged particles to the surface of the tissue to crystalize with the matrix. Image adapted from Baker et al. 2016.[36]

Mass Analyzers

There are two commonly used mass analyzers for MALDI-MSI: TOF and FTICR. An FTICR mass analyzer is an ion trap style mass analyzer that applies a uniform electric field that matches the cyclotron frequency of the ions in the magnetic field.[59] The uniform electric field excites the ions into a larger orbit that will pass by a detector.[59] The frequencies measured by the detector are converted to m/z using a Fourier transform.[59] A TOF mass analyzer accelerates ions using an electric field.[59] Once ions are at the same potential energy, they advance down a tube where smaller ions reach the detector before larger ones.[60] As a result of their physical design, FTICR analyzers have a higher resolving power for low molecular weight ions, whereas TOF analyzers excel in detecting high molecular weight ions. A recent research publication directly compared the applicability of the two detectors on the same metabolite MALDI-MSI experiment.[61] The conclusion remained the same, instruments with a FTICR detector are far better at resolving and detecting low molecular weight ions, with up to 5 times more low m/z features detected by the FTICR.[61] Both FTICR[62] and TOF[63] have shown to be highly useful tools for biomarker detection using for cancer using MALDI-MSI.

Data Processing

The importance of informatics in research is often underestimated. The need for data processing and interpretation is universal across different areas of research, countries, and languages. The ability to extract meaning from data would be stunted without informatics as acquired data would be restricted to the simplest forms or be left unprocessed.

Informatics is the science and engineering of information systems for processing, analyzing, and implementing data. Bioinformatics is specifically focused on software tools for the processing and understanding of biological data. Bioinformatics tools use computer science, mathematics, statistics, and the biological sciences. Computer scientists, mathematicians, and statisticians create and optimize tools for biological scientists. An open line of communication is needed to develop software for specific purposes. Research labs are becoming vastly interdisciplinary providing the advantage of direct communication between the makers and the users of the software. Informatics tools and statistics have languages of their own and are not divided by continents, but rather by fields of research. Simple statistics, such as standard deviation of the mean, are common among all scientists, but certain statistics used in genomics may not be applicable to microbiologists or bioengineers. For this reason, bioinformatic tools are often limited to a specific niche. However, this becomes beneficial because each piece of software can be highly specialized and optimized for selective data input.

MALDI-MSI produces large data sets that require extensive bioinformatics analysis. Manually searching and mining the data would take an extensive amount of time and would be plagued with user bias. Basic analysis and visualization of heat maps is the first step to processing MALDI-MSI data. Next is reducing the number of heat maps for a dataset to those that are statistically relevant to the experiment. The most commonly mentioned analysis and visualization software are provided by the instrument vendors: FlexImaging (Bruker), ImageQuest (Thermo Fisher Scientific), MSImageView

(Novartis), and Quantinetix (Imabiotech). Unfortunately, few statistical analysis tools are available. SCILS Lab from Bruker and SCILS is an add on software that works seamlessly with FlexImaging to provide multivariate analyses of MSI data. However, both FlexImaging and SCILS Lab software are expensive. MALDIQuant was one of the first free statistical analysis packages for MALDI data, but it is only MALDI specific, not MALDI-MSI specific; interpretation is limited and does not contain the ability to view heat maps. Cardinal is a new R package that has been published in the last year that provides all the necessary components: basic data processing and multivariate statistical analysis of MSI data with the capability of visualizing heat maps of extracted m/z. A literature search of bioinformatic tools relevant to MALD-MSI revealed 28 tools for data conversion, visualization, basic spectral process, and statistical analysis and is summarized in Table 2.

Table 2 – A summary of bioinformatic tools relevant to MALDI-MSI for use in data conversion, visualization, basic spectral process, and statistical analysis modified from Baker et al. 2016.

Abbreviations: ^{F} indicates a free software; ^{P} indicates a paid for software; ^{B} indicates a paid for MATLAB package; ^{G} indicates a downloadable graphical user interface software; ^{R} indicates a R Statistical package; ^{M} indicates a MATLAB package; ^{W} indicates an online web server

Software	**Source**	**Purpose**	**Ref**
MMSIT (MALDI MS Imaging Tool)	Novartis & Applied Biosystems^{FG}	Acquisition	[64]
CreateTarget/AnalyzeThis!	For Bruker TOF/TOF^{FG}	Acquisition and Conversion	[65]
4000 Imaging	Novartis & Applied Biosystems^{FG}	Analysis	[66]
AMASS	University of California^{FG}	Analysis	[67]
Biomap	Novartis & Applied Biosystems^{FG}	Analysis	[68]
Datacube Explorer	MS Imaging Society^{FG}	Analysis	[69]
EXIMS (EXploring Imaging Mass Spectrometry data)	University of Melbourne^{FM}	Analysis	[70]
msiQuant	Uppsala University^{FG}	Analysis	[71]
SpectViewer	MS Imaging Society^{PG}	Analysis	[72]
Axima2Analyze	National Institute of Physiological Sciences, Japan^{FG}	Converter	[73]
raw to imzML converter	MS Imaging Society^{PG}	Converter	[74]
Cardinal	Purdue University^{FR}	Statistical Analysis	[75]
MALDIquant	Institute for Medical Informatics, Statistics and Epidemiology^{FR}	Statistical Analysis	[76]
Multimaging	Imabiotech^{PG}	Statistical Analysis	[77]
omniSpect	The Georgia Institute of Technology^{FM}	Statistical Analysis	[78]
OpenMSI	Lawrence Berkeley National Laboratory^{FW}	Statistical Analysis	[79]
SCiLS Lab	SCiLS and Bruker^{PG}	Statistical Analysis	[80]

MSight	ExPASy^{FG}	Viewing	[81]
mMass	Academy of Sciences of the Czech Republic^{FG}	Viewing and Basic Analysis	[82]
MSiReader	North Carolina State University^{PM}	Viewing and Basic Analysis	[83]
FlexImaging	Bruker^{PG}	Viewing and Exporting	[84]
ImageQuest	Thermo Fisher Scientific^{PG}	Viewing and Exporting	[85]
MALDIVision	Premier Biosoft^{PG}	Viewing and Exporting	[86]
MITICS (MALDI Imaging Team Imaging Computing System)	University of Lille^{FG}	Viewing and Exporting	[87]
MSI.R	Unidad Irapuato^{FR}	Viewing and Exporting	[88]
TissueView	Applied Biosystems^{PG}	Viewing and Exporting	[89]
MSImageView	Novartis & Applied Biosystems^{FG}	Viewing of FlashQuant data	[90]

Bottom-Up Proteomics & Metabolomics in MALDI-MSI

Top-down proteomics is the study and identification of full, intact proteins.[91,92] Top-down proteomics is used for the analysis of post-translational modifications , protein expression, cellular localization, and interactions.[93] However, a large disadvantage of top-down proteomics is that it is limited to analyzing simple mixtures of proteins and struggles with large complex biological samples.[91] There is a lack of protein fractionation methods developed for mass spectrometry.[94] A solution to this problem is to analyze bottom-up proteomics or metabolomics.

Bottom-up proteomics is the study and identification of proteins after enzymatic digestion.[21] Trypsin is commonly used to its high specificity of protein digestion at the C-terminal of arginine and lysine residues.[95] On-tissue tryptic digestion of proteins for localized bottom-up proteomics was first introduced in 2007.[96] Studies have shown it's applicability in traumatized skeletal muscle[80], forensic fingerprint analysis[97], brain ischemia[98], and cancer[99].

Metabolomics is the study of all metabolites in an organism.[100] Metabolomics provides a unique advantage over proteomics in that it more closely resembles a phenotype of an organism.[101] There have been various applications of MALDI-MSI for localization of metabolites including: chronic respiratory diseases[102], localizing leaf metabolites[103], and cancer[104,105].

Both bottom-up proteomics and metabolomics provide new insights into the biochemical mechanisms of an organism. Ideally, if sample size is not a concern, a combination of top-down proteomics, bottom-up proteomics, and metabolomics analysis would be performed.[106]

Challenges in the Field of MALDI-MSI

MALDI-MSI has a high potential for impact in the biological sciences due to its unique ability to spatially localize thousands of mass features from a single tissue section. However, little standardization into sample preparation procedures has been accomplished. Bottom-up proteomics poses its own challenges in adding additional steps to the sample preparation protocol to wash away interfering metabolites and to perform an on-tissue protein digestion. The analysis of metabolites can be useful to gain insights into the phenotype of an organism. Optimization of all sample preparation protocols is critical for ensuring a complete, in-depth analysis of as many compounds as possible within a tissue. Once acquired, statistical processing of data allows for unbiased confirmation of significant results.

Thesis Objectives

The three objectives for this thesis project are:

1. To develop a method for bottom-up proteomic MALDI-MSI analysis of prostate cancer.

    a. This required optimization of experimental protocols for maximum detection of peptides. Experimental protocols included the optimization of metabolite washing, trypsin digestion incubation time, and the application of MCAEF.

2. To develop an unbiased bioinformatics workflow for simultaneous processing of MALDI-MSI datasets of multiple tissue sections using a thyroid hormone treated tadpole imaging dataset.
    a. This required creating a R Statistics Software – Cardinal Package workflow. The processing workflow included spectral processing and multiple statistical analyses to find and confirm significant findings. Both spectral processing and statistical analysis required optimization of multiple parameters based on instrument type, data type, biomolecule analyzed, and experimental set-up.
    b. This required testing to confirm statistical processing workflow was appropriate for simultaneous processing multiple datasets of control and thyroid hormone treated tadpoles for induced metamorphosis.
3. To develop a method for metabolomics MALDI-MSI analysis of FFPE colorectal liver metastasis samples.
    a. This required optimization of sample preparation protocols to be able to detect metabolites in the tissues. This required tackling the issue of using xylene, that is needed for deparaffinization, which also removes most metabolites from the tissue samples.

Chapter 2: Method Optimization of Bottom-Up Proteomic Analysis of Prostate Cancer by MALDI-MSI for Biomarker Discovery

Introduction

It is predicted that 21,000 Canadian men will be diagnosed with prostate cancer in 2017. At 20.7%, prostate cancer has the highest incident rates of any type of cancer.[107] Prostate cancer, along with all other cancers, emit unique proteins that can be used as biomarkers and detected in tissue and blood. Debate is ongoing whether or not the benefits of screening men for prostate cancer biomarkers are outweighed by potential risks of false positive or false negative assay results.[108] Current screening uses an anti-body based method to detect the concentration of the biomarker prostate-specific antigen (PSA), and its derivatives, in serum. PSA was originally discovered and developed as a prostate cancer screening target in 1991.[109] However, PSA tests are declining in use worldwide because of concerns of over cancer diagnosis due to false positive results. PSA tests cannot distinguish between prostate cancer, benign prostate hyperplasia or prostatitis.[35] This results in unnecessary stress and exposure to invasive procedures. A large meta-analysis of 53 individual studies reported over diagnosis rates ranging up to 67% for men of all ages worldwide.[110] As a result, currently in Canada the PSA test is not recommended.[111] There is a need for a biomarker and testing method that has greater sensitivity and specificity for detecting prostate cancer.

Previous studies from the Borchers laboratory on prostate cancer biomarkers included a top-down proteomics approach[58], aimed at discovering significant intact proteins, and a metabolomics approach[39], aimed at discovering significant metabolites. Figure 5 shows reconstructed ion heat maps of the top-down proteomic prostate cancer biomarkers discovered in the experiment.[58] A total of 17 different proteins were shown to have statistically significant differential expression in the cancerous region versus the non-cancerous region of the tissue. Three of these proteins were solely expressed in the cancerous region of the tissue (S100-A9, S100-A10, and S100-A12). Figure 6 shows representative reconstructed ion heat maps of metabolites shown to be of interest in this experiment.[39] Over 600 metabolomic features were shown to have differential expression

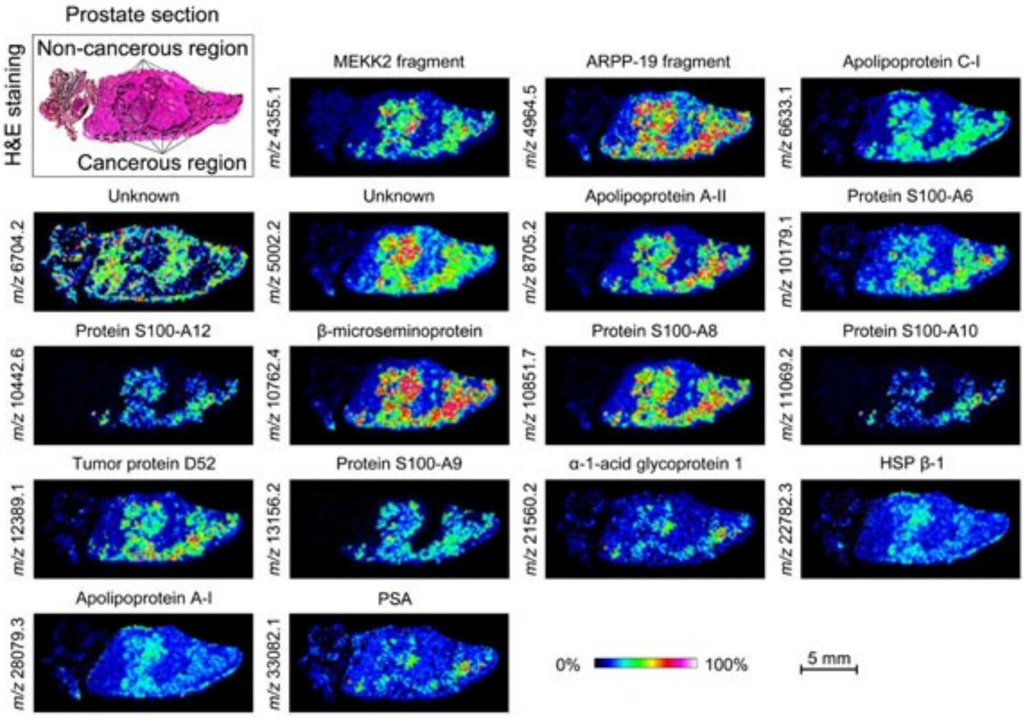

Figure 5 - Reconstructed ion heat maps of proteins shown to have differential expression in the cancerous and non-cancerous regions of a human prostate cancer tissue. Proteins were detected with sinapinic acid as the matrix in positive mode[58]. Image also adapted from Baker et al. 2016.[36] Images are reprinted with permission.

in the cancerous region when compared to the non-cancerous region. Two-hundred fifty metabolites were found only in the cancerous region, 217 metabolites were found only in the non-cancerous region, and 152 metabolites were shown to be significantly changed ($p < 0.05$, *t*-test) between the two regions.

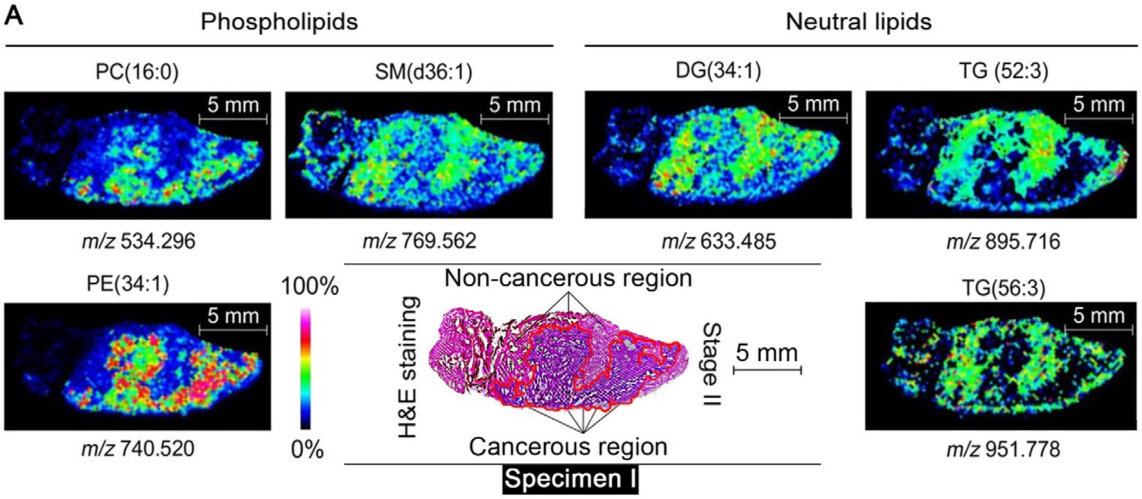

Figure 6 – Reconstructed ion heat maps of metabolites (phospholipids and neutral lipids) shown to be of interest in a human prostate cancer tissues. Metabolites were detected with quercetin as the matrix in both positive and negative ionization mode[39]. Images are reprinted with permission.

These two experimental approaches left room for a third approach to be performed on the human prostate cancer tissues. The next logical step was to perform a bottom-up proteomics experiment in which the proteins from cancerous and non-cancerous tissues are cleaved with trypsin to create tryptic peptides for detection. Trypsin is a protease that specifically cleaves proteins at the carboxyl end of amino acids lysine and arginine. Trypsin is very useful for two main reasons: it creates mass fragments that are in a more favourable mass range for easier detection by mass spectrometers and are basic due to being cleaved at the carboxyl side, creating an easily ionizable location on the peptide. Differential occurrence could enable identification of potential biomarkers.

Bottom-up on-tissue MALDI-MSI had not yet been performed in our laboratory, so no protocol existed. A literature review was performed to determine if standard protocols existed. A summary of this literature search can be found in Supplementary Table 1. Standard method preparation steps include: cutting the tissue, mounting the tissue onto a MALDI compatible surface, drying the tissue, washing the tissue to remove ion-suppressing metabolites, trypsin deposition, trypsin incubation, and matrix deposition.

This data chapter focuses on the development and results of a bottom-up proteomic MALDI-MSI experiment on a human prostate cancer tissue. Optimization of sample preparation parameters found the following results: an additional wash step of 50mM sodium bicarbonate after the standardized steps (70% ethanol, 70% ethanol, 100% ethanol) was favorable due to increasing the pH of the tissue which is optimal for tryptic digestion; a trypsin incubation time of 18 hours to allow complete trypsin digestion; and to include the MCAEF technique with a CHCA matrix deposition for increased spectra quality. A total of 245 peptides belonging to 86 unique proteins were identified using accurate mass matching.

Methods

Samples

The prostate cancer sample used was obtained from BioServe BioTechnologies (Beltsville, MD, USA). The tissue was from a 62 ± 2-year-old male patient during prostate cancer surgical removal, with the patient's informed consent. The tissue was diagnosed at prostate cancer stage II. The tissue was stored at -80 ˚C upon receipt and for the duration of the experiment. The use of anonymized human samples was approved by the Ethics Committee of the University of Victoria.

Reagents

Ammonium bicarbonate (NH_4HCO_3), sodium hydroxide (NaOH), dithiothreitol (DTT), iodoacetamide (IAA), acetic acid, hematoxylin & eosin (H&E), high performance liquid chromatography (HPLC)-grade ethanol, HPLC-grade methanol, liquid-chromatography/mass spectrometry (LC/MS)-grade acetonitrile (ACN), chloroform, xylene, water, trifluoroacetic acid (TFA), and formic acid (FA), quercetin, and CHCA were purchased from Sigma-Aldrich (St. Louis, MO, USA). Sequencing Grade Modified Trypsin was purchased from Promega GmbH (Product number: V5111, Mannheim, Germany). ESI tuning mix was purchased from Agilent (Agilent Technologies, Santa Clara, CA, USA).

Tissue Sectioning

The frozen prostate specimen was sectioned at -24 ˚C in a Microm HM500 cryostat (Waldorf, Germany). Serial sections of 14-µm thickness were thaw-mounted onto ITO-coated glass microscope slides obtained from Bruker Daltonics (Bremen, Germany).

Tissue Washing

As per the literature review presented in the introduction, there were many different wash steps used in various experimental protocols. A "basic wash" is a standardized wash protocol that consists of two sequential washes in 70% ethanol and one wash in 100% (or 95%) ethanol. All wash steps were performed for 30 seconds, unless noted. All washes were performed in 50 mL Eppendorf tubes. All solutions were prepared once for the duration of the method optimization experiment. After washing the tissue was complete, the slide was placed under vacuum for 10 minutes to ensure complete evaporation of the solvents. The following five washes were tested to determine which wash protocol was optimal:

1. basic wash
2. basic wash + 90:9:1 ethanol/acetic acid/water
3. basic wash + 50 mM NH_4HCO_3
4. Carnoy's wash
    1. 70% ethanol
    2. 100% ethanol
    3. 6:3:1 ethanol/chloroform/acetic acid (2 minutes)
    4. 100% ethanol

    5. water
    6. 100% ethanol
5. no wash

Trypsin Digestion

A 20µg pre-weighed amount of trypsin was used for each slide. As per the product information instructions from Promega, 40-µL of 50 mM acetic acid was added to the Eppendorf tube and vortexed for 2 minutes. If necessary, this solution was stored at -4 ˚C until needed. As per the ImagePrep Instruction Manual, once ready for trypsin deposition, 200-µL 50 mM NH_4HCO_3 was added to the Eppendorf tube. This solution was vortexed for another 2 minutes. Two-hundred twenty µL of the solution was transferred to the ImagePrep electronic matrix sprayer (Bruker, Bremen, Germany). The ImagePrep trypsin digestion deposition method was used.

Once trypsin deposition was complete, the slide was immediately transferred to a humidity chamber for the trypsin incubation. It was essential to avoid exposure to air to maintain trypsin activity. The humidity chamber apparatus was a heated water bath with a raised platform in the centre for the slide to sit on and a plastic cover over top of the bath. A small cover was placed on top of the platform to ensure that the slide was not contaminated with falling water drops from the large plastic cover. Once the incubation was complete, slides were dried under vacuum for 20 minutes. The following times were tested for trypsin digestion times:

1. 2 hours

2. overnight (16-18 hours)

Matrix Coating

CHCA was prepared at a concentration of 7 mg/mL in 50% ACN and 0.2% TFA. Typically, a total of 10 mL was made at a time. Slides and tissue sections were coated with the CHCA matrix with the ImagePrep electronic matrix spray generator. The matrix coating was performed with the standard ImagePrep CHCA method.

During matrix coating, the previously described MCAEF technique was applied. A uniform electric field at an intensity of +600 V/m was applied to the tissue in positive-ion mode. An experiment was performed without MCAEF to ensure bottom-up proteomic mass spectra were also enhanced by the technique. This was done by performing a typical matrix coating with the standard ImagePrep instrument that did not have applied voltages or secondary conducive glass slide.

MALDI-MSI

All mass spectra were acquired on an Apex-Qe 12-Tesla hybrid quadrupole-FTICR mass spectrometer ((Bruker Daltonics, Billerica, MA, USA). The instrument was equipped with an Apollo dual-mode ESI/MALDI ion source. The instrument’s laser source was a 355-nm solid-state Smartbeam Nd:YAG ultraviolet laser (Azura Laser AG, Berlin, Germany).

A calibration solution was prepared by adding 10 µL of Agilent “ESI tuning mix” solution with 10 mL of 75% ACN with 0.1% formic acid. The calibration was directly infused into the ESI side of the ion source for instrument calibration. The instrument was calibrated before every experiment performed.

All mass spectra were acquired over the mass range of 200-2200 m/z with a data acquisition size of 512 kilobytes per second. Profiling data was acquired by accumulating twenty scans at 100 laser shots per scan. Profiling spectra were acquired with ApexControl (Bruker, Bremen, Germany). Imaging data was acquired with one scan at 100 laser shots per scan with the minimum raster step size of 200-µm. Imaging spectra were acquired with Apex Control, Hystar Control, and FlexImaging 2.1 (Bruker, Bremen, Germany). Teaching points were generated with a Tipex Wite-Out pen to enable the instrument to have an accurate slide position for spectra acquisition. Profiling data was acquired for each of the different method steps during the method optimization. Profiling data acquired was recorded to be from the cancerous or non-cancerous regions of the tissue. Imaging data was acquired for the final optimized method protocol.

Data Analysis

Profiling mass spectra were processed using DataAnalysis 4.0 (Bruker, Bremen, Germany). Batch internal mass calibration, peak de-isotoping, and monoisotopic peak picking were performed using a customized VBA script within DataAnalysis. Peak alignment was performed with a previously written custom program with LabView development suite with an allowable mass error of 3 ppm. The custom VBA DataAnalysis script and customized program with LabView are described elsewhere.[112]

Imaging mass spectra were viewed with FlexImaging. Using this software, reconstructed ion heat maps were created. Images were exported as JPEG files for viewing. Principle component analysis (PCA) and partial least squares-discriminant analysis (PLS-DA) were performed with MetaboAnalyst 3.0 (http://www.metaboanalyst.ca).[113]

Data Processing Statistical Analysis

Peak lists (m/z and intensity) were exported from multiple replicates and profiling spots from each experiment. Peak lists were exported into CSV format and opened using Microsoft Excel. The total number of spectra included in the bar graphs represents the n-value. Average peak counts were totaled after removing all background signals and peaks that did not meet a signal to noise minimum. Background signal was removed by finding peaks that occurred in 80% of the spectra. Peaks with a signal to noise ratio less than 5 were removed. Peak intensities were averaged from the peaks remaining after the background signal was removed and peaks with a signal to noise ratio of less than 5. Peak lists were imported into R Statistical[114] using R Studio[115]. The mean intensities and counts were calculated along with corresponding standard error of the mean and plotted on a standard bar graph. Statistical analysis included performing a Kruskal-Wallis Rank Sum analysis of variance and a Mann-Whitney U post-hoc test. p-values from the Mann-Witney U test were used for determining significance.

H&E Staining

In-house H&E staining was performed. Each solution was in a glass Coplin jar. The same solvents were used for the duration of the experiment as multiple slides can be stained from the same set of solutions. The following protocol was used:

1. 95% ethanol for 30 seconds
2. 70% ethanol for 30 seconds
3. water for 30 seconds
4. hematoxylin for 2 minutes
5. water for 30 seconds
6. 70% ethanol for 30 seconds
7. 95% ethanol for 30 seconds
8. eosin for 1 minute
9. 95% ethanol for 30 seconds
10. 100% ethanol for 30 seconds
11. xylene for 2 minutes

Protein Extraction

Twenty-five mg of prostate tissue was used for protein extraction based on previously described protocols.[116,117] The human prostate sample was homogenized in 200 µL of water with a Retsch MM400 mixer mill (Haan, Germany) with two 5-mm stainless steel balls for 2 x 1 minute at 30 Hz. Next, 800 µL of 1:3 chloroform/methanol solution was added. This was followed by another homogenization step for 30 seconds at 30 Hz. The stainless-steel balls were removed and then the tube was centrifuged at 16000g for 20 minutes at 4 ˚C (Eppendorf 5425 R, Eppendorf, Mississauga, Canada). The lipid-containing supernatant was discarded. The protein pellet was resuspended in 600 µL of water containing 3% formic acid. The tube was then vortexed for 3 times for 1 minute each to fully re-suspend the protein. The tube was again centrifuged at 16000g for 15 minutes at 4 ˚C. The supernatant was collected using 200 µL gel loading pipette tips and divided equally between two tubes. Protein solutions were dried using a Speed Vac (Savant SPD1010 Thermo Electron Corporation, Waltham, MA, USA). Tubes were stored at -80 ˚C until used.

Protein Digestion

One protein pellet was resuspended in 300 µL of 25 mM DTT/25 mM NH_4HCO_3 and vortexed until dissolved to break the disulfide bonds. The protein solution was then allowed to incubate at 56 ˚C in a Thermomixer (Eppendorf, Hamburg, Germany) at 750 rpm for 50 minutes. Then the alkylation was performed by adding 300 µL of 100 mM IAA/25 mM NH_4HCO_3 and letting sit at room temperature in the dark under tin foil for 45 minutes. To quench the reaction, 15 µL of 1 M DTT/25 mM NH_4HCO_3 was added. Next, 200 µL of 50 ng/µL trypsin in 25 mM NH_4HCO_3 was added. The digestion was allowed to incubate over night at 37 ˚C. Once incubation was complete, the reaction was quenched with 800 µL of 0.2% TFA. The solution was then vortexed for 2 minutes. Next, a Solid Phase Extraction (SPE) was performed with Oasis HLB SPE extraction cartridges (200mg/3mL column, Waters Inc. Milford, MA, USA). The column was first conditioned with 1 mL of methanol then 1 mL of 0.1% TFA. Then 1 mL of protein solution was loaded onto the column. The column was then washed with 3 times 1 mL 0.1% TFA. The protein was eluted with 3 time 600 µL 75% ACN in 0.1 % TFA. The eluates were pooled and dried with a speed vac. The dried protein was then reconstituted in 100 µL of 2% ACN in 0.1% TFA and then a 1 in 100 dilution in 2% ACN in 0.1% TFA to achieve no more than 1 µg on the column at a time with an 8 µL injection volume.

LC-MS/MS

Liquid chromatography tandem mass spectrometry (LC-MS/MS) was performed by loading 8 µL onto a Magic C18-AQ trapping column (100µm I.D., 2 cm length, 5 µm, and 100 Å; Michrom BioResources Inc., Auburn, CA) and separated on an in-house packed Magic C18-AQ capillary column (75µm I.D.×15cm, 5µm, 100Å) at a flow rate of 300nL/min using a Thermo Scientific EASY-nLC II liquid chromatograph. The mobile phase was 2% ACN in 0.1% formic acid (Solvent A) and 90% ACN in 0.1% formic acid (Solvent B). The flow rate was set to 300 nL/minute with one of the following elution gradients: 5% B to 45% B in 45 minutes, 45% B to 80% B in 2 minutes, and 80% B to 100% B in 2 minutes for a total run time of 49 minutes or 5% B to 40% B in 100 minutes, 40% B to 80% B in 5 minutes, 80% B to 100% B in 2 minutes for a total run time of 120 minutes. A built-in equilibration step was performed between each set of injections.

The chromatographic system was coupled to a Orbitrap Fusion (ThermoFisher, San Jose, CA, USA) which has a nano-flow ESI source. A user defined lock mass of 445.12002 m/z (a ubiquitous siloxane contaminant) was used for calibration. The ESI ion source was set to 2550 V with an ion transfer temperature of 275 ˚C. For full scans with no fragmentation, the Orbitrap detector was set to a resolution of 120000 with a normal mass range of 400-2000 m/z and no quadrupole isolation. A dynamic exclusion was performed where ions were excluded after being detected 2 times if occurring within 5 seconds. Ions were excluded from the data for 10 seconds. Data was acquired in positive mode with profile data recorded. The charge states of the ions detected were limited from 2-5 with undetermined charge states not included. The intensity threshold was set to 5.0e4. Decisions for the acquired mass spectra included top speed data dependent mode with the precursor priority set to most intense. For MS/MS both collision induced dissociation (CID) and higher-energy collisional dissociation (HCD) were used with the following settings: collision energy of 35%, with an activation of 0.25 and multi-stage activation off, using the ion trap as the detector with a rapid rate, the automatic gain collector set to 2.0e3 with 1 microscan set to a maximum injection time of 300 ms, and collecting data in centroid mode. Exclusion lists were made by opening the acquired data in Proteome Discoverer 1.4.0.228 software (Thermo Scientific, Bremen, Germany) and creating a list of the high confidence ions. The following methods were run:

1. CID with 49-minute gradient
2. CID with 120-minute gradient
3. CID with 49-minute gradient and exclusion list
4. HCD with 49-minute gradient
5. HCD with 120-minute gradient
6. HCD with 49-minute gradient and exclusion list

LC-MS/MS Data Analysis

Raw data files were analyzed with Proteome Discoverer to generate peak lists for database searching. Protein identification was carried out with an in-house Mascot 2.2

server searching Uniprot_Human (all entries) with the following settings: allowable missed trypsin cleavages of 2, a maximum fragment tolerance of 0.6 Da, a maximum precursor tolerance of 10 ppm, a static modification of carbamidomethylation (C), and dynamic modifications of deamidation (N, Q) and oxidation (M). Percolator was used to validate peptide assignments with the following settings: maximum delta Cn of 0.05, a strict false discovery rate of 0.01 and a relaxed false discovery rate of 0.05. All six acquired datasets were exported to excel together.

Accurate Mass Matching for MALDI-MSI Peptide ID and Protein Assignment

A general workflow for accurate mass matching can be found in Figure 7. Exported peak lists from MALDI-MSI data and exported peak lists from LC-MS/MS data were color coded and combined into a single excel column. After sorting all m/z values from highest to lowest, a ppm calculation was performed between all neighbouring MALDI-MSI and LC-MS/MS values. All m/z values that matched with under 5 ppm error were considered to be an accurate mass match for peptide identification and protein assignment.

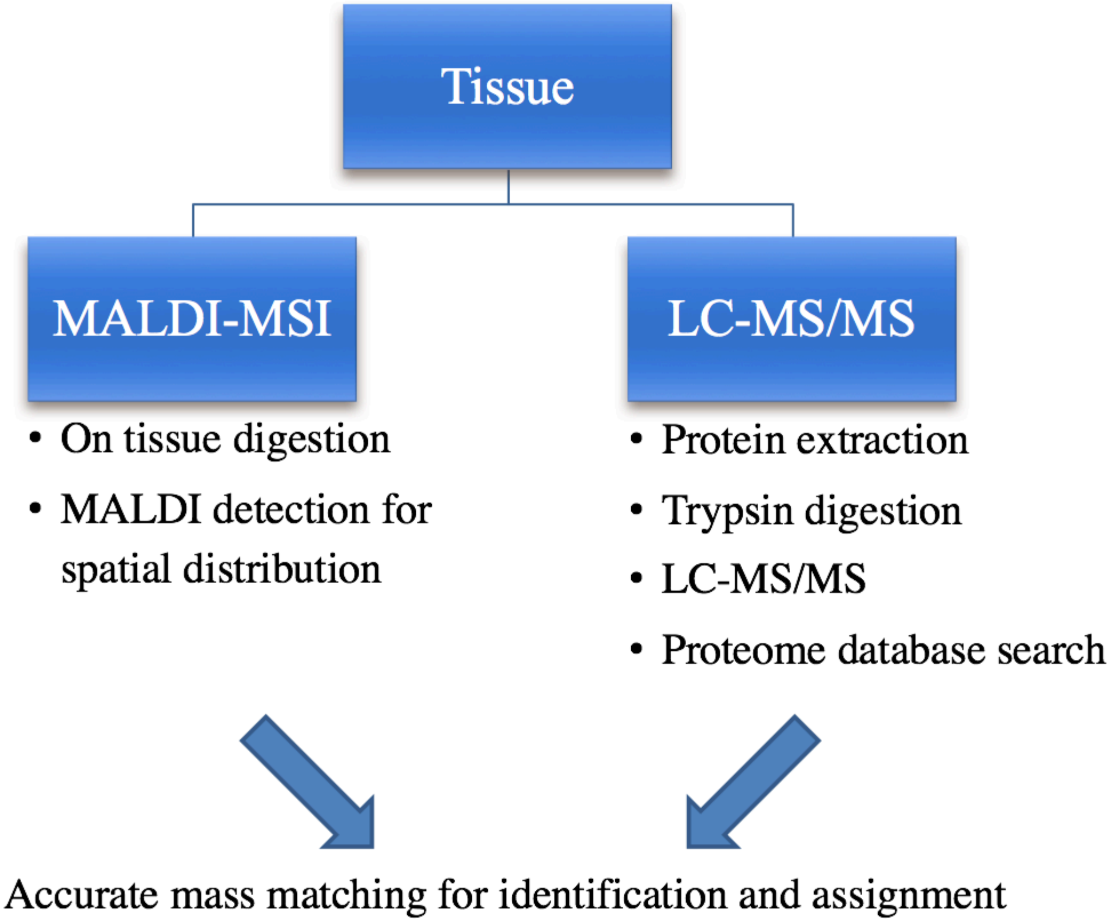

Figure 7 – Workflow used for accurate mass matching between MALDI-MSI and LC-MS/MS data for peptide identification and protein assignment

Results & Discussion

Tissue Wash Optimization

After performing a literature review, it was apparent that different laboratories used various wash protocols to remove metabolite and other organic small molecules from the tissue that may cause ion suppression. The four most common washes were compared against a dataset with no wash step. The no wash step was performed to act as a baseline to determine the total amount of ion suppression caused by the background molecules. As seen in Figure 8, all washes except the basic wash significantly increased the average

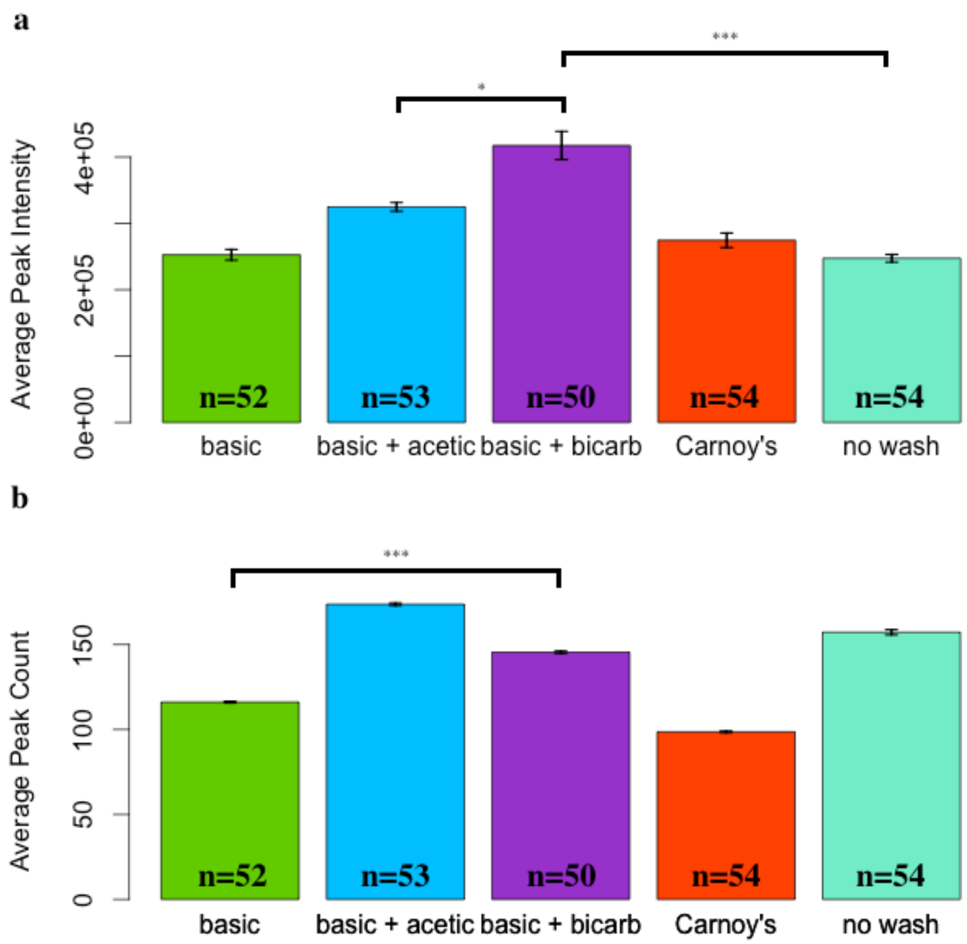

Figure 8 – (a) Average peak intensity and (b) average peak count of the MALDI-MSI wash optimization experiment on prostate cancer tissue. Detail for each wash can be found in the Methods section. Not all significant comparisons shown on graph. Detailed p-values can be found in Supplementary Table 2.* $p < 0.05$, ** $p < 0.01$, and *** $p < 0.001$

peak intensity (p-values <2e-16, <2e-16, and 1.9e-5, respectively). All p-values calculated by a Mann Whitney U test can be found in Supplementary Table 2. Of note is the significant increase of the peak intensity of the basic wash + 50 mM sodium bicarbonate in comparison to the no wash experiment and the basic wash + 50 mM acetic acid wash. It is predicted that the increased peak intensity of the sodium bicarbonate wash is due to decreased ion suppression due to background signals from lipids and other metabolites. The increased peak intensity of the sodium bicarbonate wash compared to the acetic acid wash aided in the final decision of using a sodium bicarbonate wash (p-value 0.017). A significantly higher peak count for the no wash experiment compared to the basic wash and Carnoy's wash (p-value 0.0093 and 0.0015, respectively) amplifies the prediction of having background and metabolite signals in the spectra. An additional reasoning behind choosing the sodium bicarbonate wash was because the step immediate after the wash step is trypsin digestion, which performs optimally at a slightly basic pH, which is aided by sodium bicarbonate rather than the acetic acid or Carnoy's wash. The method preparation and instrument parameters were optimized for peptides, meaning peak intensities may not be strong for metabolites. However, they will still be detected and can cause not only an artificially high peak count, but cause ion suppression for peptide signals. Ideally the sodium bicarbonate wash would have shown the highest peak intensity and highest peak count. Unfortunately, the acetic acid wash showed a significantly higher peak count than the bicarbonate wash (p-value 0.0034). Due to the trypsin digestion potentially being affected by the pH, the sodium bicarbonate wash was given preference. It was confirmed that the sodium bicarbonate wash showed significantly higher peak counts in comparison to only using a basic wash (p-value 0.0034).

Trypsin Digestion Incubation Time Optimization

The literature review also revealed an inconsistency in trypsin digestion incubation time. Two hours was more common for formalin-fixed and paraffin embedded (FFPE) tissue trypsin digestion, however it was used occasionally for fresh-frozen tissue. Overnight digestion (18 hours) was more common for fresh-frozen tissue. Comparison of peak intensities and peak counts gave for differing results (Figure 9). The overnight

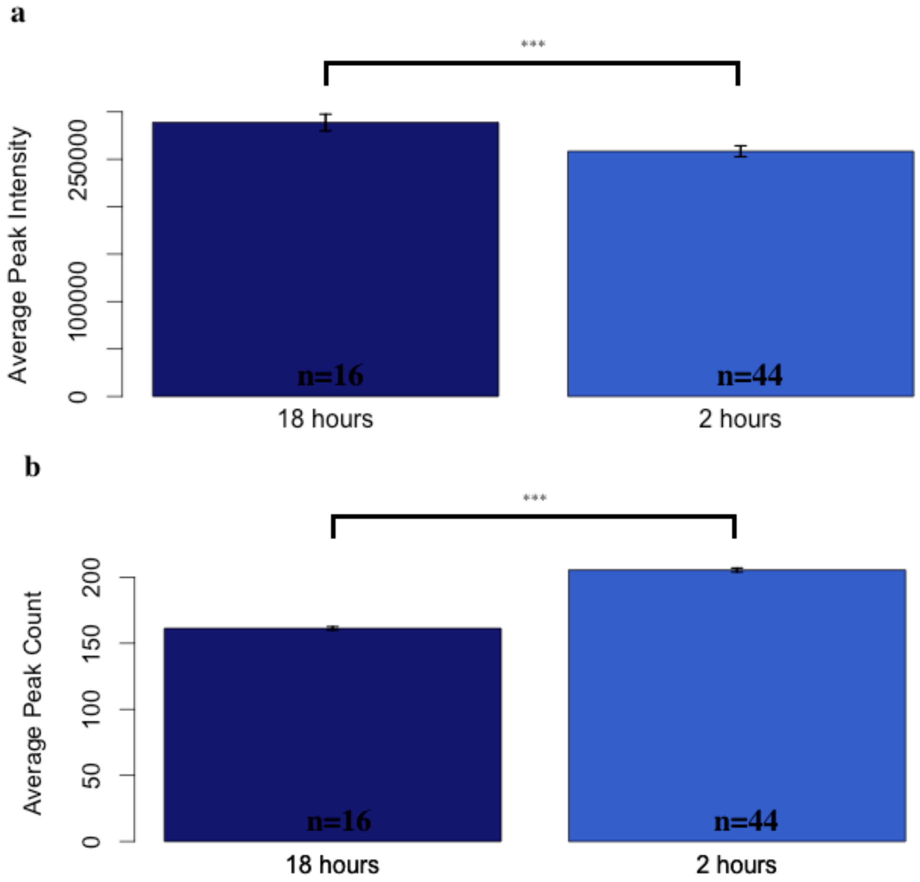

Figure 9 – (a) Average peak intensity and (b) average peak count of the MALDI-MSI trypsin digestion incubation time experiment on prostate cancer tissue. Details for each incubation time can be found in the Methods section. Detailed p-values can be found in Supplementary Table 2.* $p < 0.05$, ** $p < 0.01$, and *** $p < 0.001$

digestion had a significantly higher peak intensity (p-value <2.2e-16), whereas the 2-hour digestion had a significantly higher peak count (p-value 0.00043). However, since average peak intensity was given priority in the tissue wash optimization, the average peak intensity was given priority again for this optimization. This was chosen because increasing the intensity of low concentration peptides that could be potential biomarkers is favourable. Therefore, an 18-hour trypsin digestion incubation time was chosen as the optimal step. This also agreed with the more common literature incubation time for fresh-frozen tissues.

Confirmation of MCAEF Optimization

The Borchers' laboratory had previously published multiple articles describing that MCAEF gives for enhanced mass spectra[38,39,58]. This was confirmed for bottom-up proteomic MALDI-MSI experiments by comparing a dataset with MCAEF to a dataset without MCAEF. The first step of this comparison was to perform a Principle Component Analysis (PCA) (Figure 10) and Partial Least Squares-Discriminant Analysis (PLS-DA) Figure 11. Upon first view of the PCA scores plot (Figure 10), it appears the datasets with MCAEF and without MCAEF are not different at all. However, upon deeper analysis, this can be expected from a PCA scores plot. The two datasets, with MCAEF and without MCAEF, are from the same tissue containing the same cancerous and non-cancerous regions. Therefore, it can be expected that the spectra from these two datasets will look very similar to each other and may not be separated in a PCA analysis. The overlap in the PCA analysis is a result of the style of statistical analysis that a PCA is; a PCA does not incorporate original groupings of the inputted data. As a result, a PLS-DA was

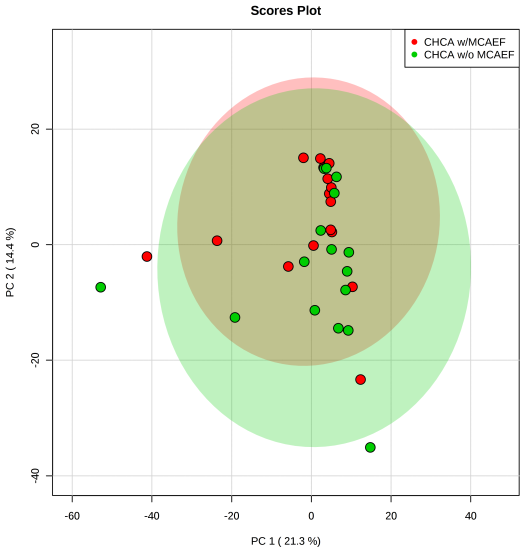

Figure 10 – The scores plot from a Principle Component Analysis test for the MALDI-MSI bottom-up proteomic prostate cancer optimization experiment. Data are with MCAEF and without MCAEF during matrix deposition. Details on the MCAEF set up can be found in the Methods section.

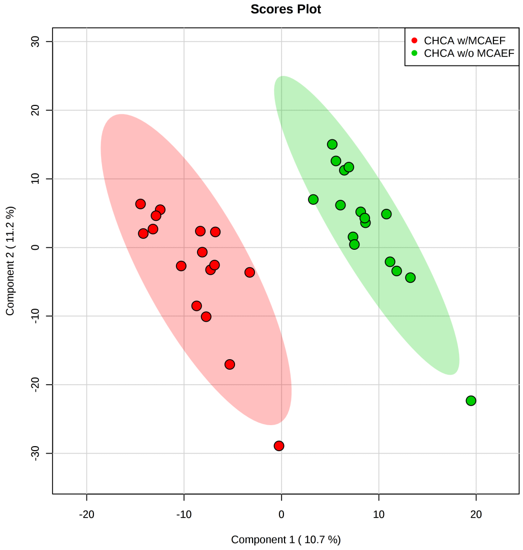

Figure 11 – The scores plot from a Partial Least Squares-Discriminant Analysis test for the MALDI-MSI bottom-up proteomic prostate cancer optimization experiment. Data are with MCAEF and without MCAEF during matrix deposition. Details on the MCAEF set up can be found in the Methods section.

performed. A PLS-DA does incorporate the original groupings of the data. If the two datasets were unable to separate in a PLS-DA, this would indicate that they are in fact not different in any way (peak intensity or peak count). As seen in the PLS-DA scores plot, the datasets with MCAEF and without MCAEF are separated from each other (Figure 11), confirming that the MCAEF technique creates different spectra in the dataset. The second step of this comparison is to confirm that the MCAEF technique is enhancing the spectra of the datasets. This was done by comparing the average peak intensities and average peak counts between MCAEF and non-MCAEF experiments (Figure 12). The Mann Whitney U test confirmed that the MCAEF technique was statistically significant in increasing both the peak intensity (p-value <2.2e-16) and peak count (6.4e-05). This demonstrates that the use of the MCAEF technique provides enhances spectra for bottom-up proteomic MALDI-MSI experiments.

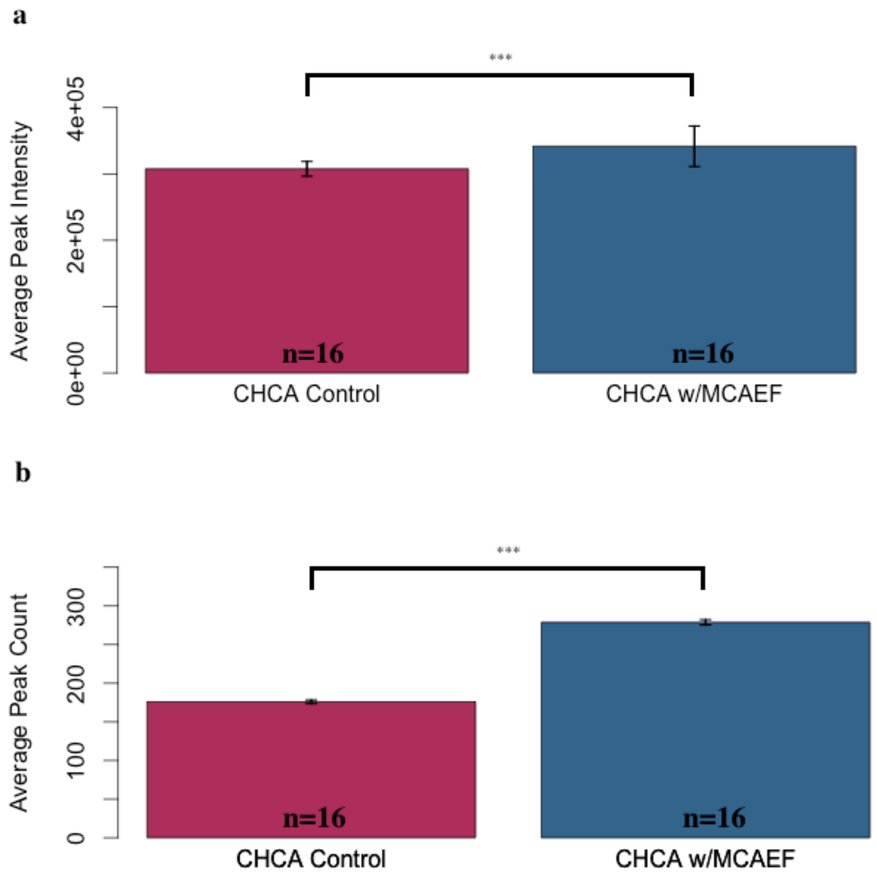

Figure 12 – (a) Average peak intensity and (b) average peak count of the MALDI-MSI MCAEF optimization experiment on prostate cancer tissue. Details for the MCAEF set up can be found in the Methods section. Detailed p-values can be found in Supplementary Table 2.* $p < 0.05$, ** $p < 0.01$, and *** $p < 0.001$

Accurate mass matching for peptide identification and protein assignment

The final step in the prostate cancer bottom-up proteomic MALDI-MSI experiment was to determine what peptides and proteins were present in the tissue. After identification and assignment, the aim is to find potential biomarkers that can differentiate between the cancerous and non-cancerous of the tissue. After combining data from the MALD-MSI wash optimization and trypsin digestion incubation optimization experiments and accurate mass matching to 5 ppm to the LC-MS/MS data, a total of 245 peptides were identified belonging to a total of 86 unique proteins. The complete list of peptide identifications and protein assignments can be found in Supplementary Table 6.

Many known proteins that have been associated previously with prostate cancer were detected, such as PSA and S100. As seen in the bottom right hand image in Figure 13, the cancerous region of the tissue is the darker pigmented region near the bottom half of the tissue. Figure 13 contains reconstructed ion heat maps of various peptide mass features that showed differentiation between the cancerous and non-cancerous regions of the tissue. Most of the peptide mass features had increased relative intensities in the cancerous region, but some peptide mass features were decreased in the cancerous region. Protein assignments are included if available. Representative mass spectra are shown in Figure 14 of cancerous and non-cancerous regions in the prostate cancer tissue analyzed. Visual differences can be seen right away between the two spectra.

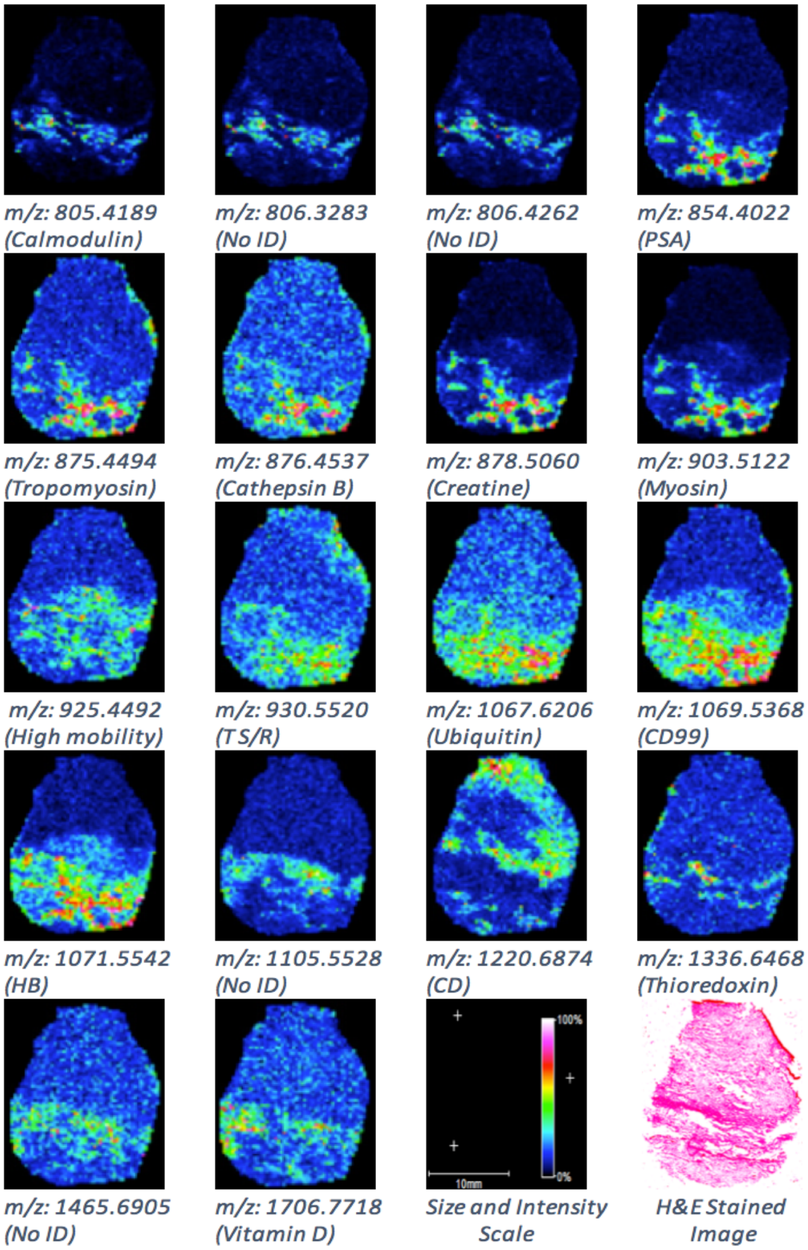

Figure 13 – Reconstructed ion heat maps from the bottom-up proteomic MALDI-MSI prostate cancer experiment. Peptide mass features shown differentiate between the cancerous and non-cancerous regions. The size and intensity scale, along with an H&E image can be found in the bottom right hand corner.
Abbreviations: CD – cold-inducible RNA binding protein; HB – hemoglobin; P1RS – phosphatase 1 regulatory subunit; PSA – prostate specific antigen; T S/R – thiosulfate sulfurtransferase/rhodanese-like domain containing protein

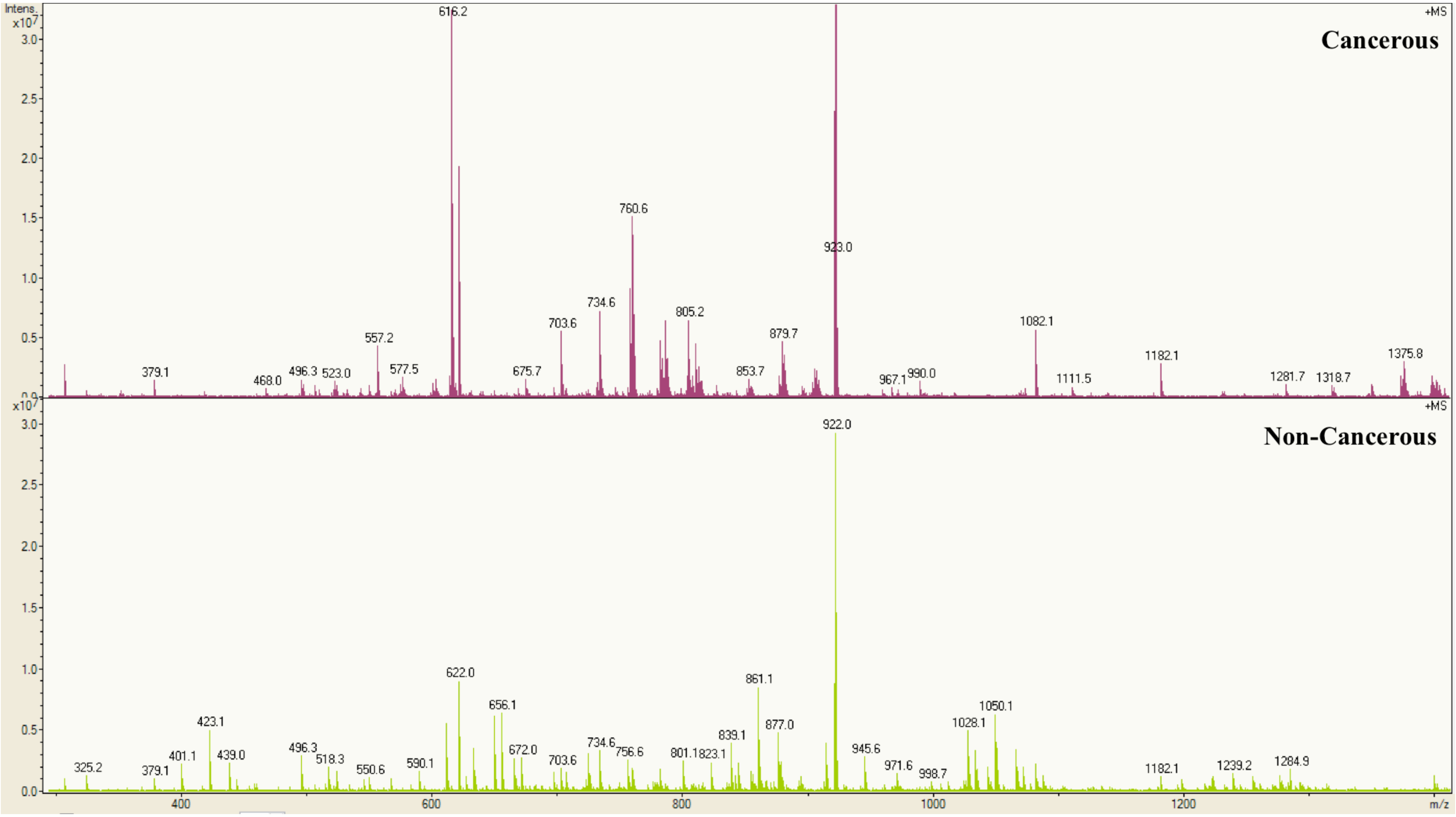

Figure 14 – Representative bottom-up proteomic mass spectra acquired MALDI-MSI from (top) cancerous and (bottom) non-cancerous regions of the prostate cancer tissue.

Conclusions & Future Directions

A literature review of the current protocols used for bottom-up proteomics on fresh-frozen tissue using MALDI-MSI revealed that there are many different approaches taken. The steps in the protocol that differed the most were the tissue wash step and the trypsin digestion incubation step. These two steps were chosen for optimization with the fresh-frozen prostate cancer tissues. Additionally, the MCAEF technique had not yet been applied to bottom-up proteomic MALDI-MSI, so this step was also investigated during the optimization experiment.

Results found that all wash steps do remove metabolites and other small organic molecules that can cause ion suppression in the mass spectra. It is important to include some form of wash step. The wash step chosen as optimal was the basic wash (2 times with 70% ethanol and 1 time with 100% ethanol, all for 30 seconds) plus an additional 30 second wash with 50 mM sodium bicarbonate. This was chosen as it gave for an optimized average peak intensity, was the most common additional wash step, and adjusted the pH of the tissue to slightly basic, which is optimal for trypsin digestion. As for the trypsin digestion incubation time, the optimal time was chosen to be 18-hours. This was chosen as it is again more common in the literature, as well as it gave for an increased average peak intensity. In depth analysis of the MCAEF technique showed that using MCAEF does give for enhanced spectra compared to acquired data without MCAEF.

After optimization, MALDI-MSI data was accurate mass matched to a LC-MS/MS dataset that was acquired from the fresh-frozen prostate cancer tissue. A total of 245 peptides were identified which resulted in 86 unique proteins to be assigned (Supplementary Table 6). Many of the detected peptide mass features were differentially expressed between the cancerous and non-cancerous regions of the prostate cancer tissue.

Future experiments could take the optimized protocol developed in this experiment and apply it to a larger scale dataset. Ideally, a minimum of 30 different prostate cancer tissues would be analyzed. This larger dataset would allow for a greater and more in-depth understanding of the different molecules that are affected by prostate cancer. If enough tissue was available for the experiment, a "meta-omic" approach could be taken, using the protocols from the previous experiments of top-down proteomics and metabolomics, and the current experimental protocol for bottom-up proteomics, aiming to find a general pathway affected by prostate cancer. An additional direction that could be taken with the experiment, if resources are available, would be to perform a greater statistical analysis directly on the imaging data, rather than on profiling data. This would allow statistical analysis and direct data visualization to be combined for a better correlation to the pathology of the cancerous tissue.

Chapter 3: Metabolomic insights into the effects of thyroid hormone on *Rana catesbeiana* metamorphosis using whole-body Matrix Assisted Laser Desorption/Ionization-Mass Spectrometry Imaging (MALDI-MSI)

Introduction

Postembryonic modifications must occur for the proper development of many vertebrate organisms. For humans, this period after embryogenesis is crucial for proper brain development, lung maturation and the modification of all other organs to prepare the fetus for life outside of the womb. A dramatic demonstration of the importance of this post embryonic development is frog metamorphosis where an aquatic herbivorous tadpole transitions to a (semi-)terrestrial carnivorous frog. Metamorphosis leads to extensive modifications including resorption of the tail, formation of legs, switching from ammonotelic to ureotelic nitrogenous waste excretion, maturation of bone, and further development of the central nervous system.[118,119] These comprehensive adaptations occur independently yet in synchrony for each organ allowing for a smooth transition between niches.

The complex array of physiological changes that occur in vertebrate postembryonic development are driven by hormone signaling. In the case of frogs, such as the North American bullfrog, *Rana [Lithobates] catesbeiana,* thyroid hormone (TH) is the sole signaling molecule to initiate the changes that occur in metamorphosis[118] In the early pre-metamorphic stages of development, the tadpole has a thyroid gland but is functionally athyroid. However, it is competent to respond to exogenous TH triggering a precocious metamorphosis.[118,120] This feature makes this species a model organism for experimental manipulation to study TH signaling and postembryonic development.

TH initiates metamorphosis by interacting with nuclear receptors to induce tissue-specific gene expression programs.[119,121] Due to this mechanism of action, anuran metamorphosis research has focused primarily in the realm of genomics and transcriptomics. These types of studies provide the necessary foundation required for understanding the mechanisms of metamorphosis induction. Metabolomics, however, is essential to unlocking the answers to phenotypic and physiological responses in the initiation of this complex developmental program. As of yet, only two studies have been performed to examine the frog metabolome. Ichu et al. recently performed the first wide-scale metabolomic study of *R. catesbeiana* and frog metamorphosis.[122] This research utilized tadpole serum to create a system wide picture of the metabolomic changes that occur throughout the stages of natural metamorphosis. Thousands of metabolites were involved in this extensive development program which could mostly be classed into the arginine and purine/pyrimidine, cysteine/methionine, sphingolipid, eicosanoid metabolism, and urea cycle pathways. Another metabolomics study by Suzuki et al. looked at the earlier initiation events that occur in TH-induced metamorphosis focusing on the lipid components of *R. catesbeiana* tadpole liver and found there was no significant changes in glycerophospholipid composition after three or seven days of TH treatment.[123] This treatment did, however, affect the fatty acid saturation altering the properties of the cell membrane. Although these studies both contributed greatly to further the understanding of how metabolic pathways are involved in metamorphosis neither considered how the pleiotropic effects of TH signaling in metamorphosis affect the fates of each organ in a different manner. Insight into these differences is critical to uncovering the mechanisms involved in the coordination of tissue responses.

The metabolome is complex, especially when considering the amount of chemical diversity between different classes of compounds. Commonly-used mass spectrometry techniques such as Liquid Chromatography-Tandem Mass spectrometry (LC MS/MS) have the ability to simultaneously detect and quantify a large variety of chemical structures including peptides, sugars, ketones, amino acids, lipids, toxins, drugs, and xenobiotics. These techniques, however, require a homogenized sample, therefore, different tissues must either be processed separately or whole-body samples are used but tissue-specific information on compounds of interest is sacrificed. Matrix-Assisted Laser Desorption/Ionization-Mass Spectrometry Imaging (MALDI-MSI) is used for its ability to retain location information during data acquisition. This technique has been adapted to allow for whole-body MALDI-MSI.[124,125] This challenging area of research has been successfully performed on only a few species including: mice[126–128] and zebrafish[129]. However, no whole-body MALDI-MSI experiments have been performed on amphibians. We report the first successful demonstration of the use of MALDI-MSI on whole-body sections of tadpoles to identify tissue-specific metabolite profiles that are significantly affected during TH-induced metamorphosis.

A recently developed technique, Matrix Coating Assisted by an Electric Field (MCAEF), by the Borchers laboratory is used to acquire enhanced spectra.[38] A schematic diagram can be found in Figure 15. This technique increases both the total ion count in a mass spectrum as well as signal to noise ratio by up to 5 times. This technique has been applied for the metabolite analysis in porcine adrenal glands[38], a proteomic analysis of prostate cancer[58], and a metabolomics analysis of prostate cancer[39]. This technique was used for the current experiment.

Using this technique, we were able to examine the distinctive metabolite profiles in five organs and detect over 5000 metabolites. Of these, 136 were significantly affected by TH signaling revealing the first glimpse of the dynamic nature of the metabolomic environment in metamorphic tadpole tissues.

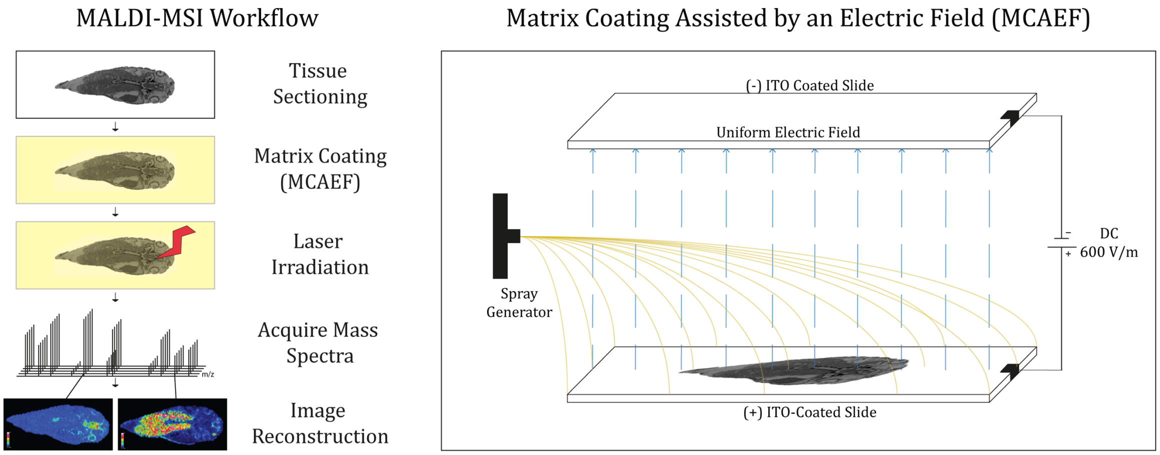

Figure 15 – (Left) A MALDI-MSI workflow depicting tissue sectioning onto a glass slide, homogenous matrix coating using the MCAEF technique, rastered laser irradiation across the tissue, and ion heat map image reconstruction based on the acquired mass spectra (Right) A diagram of the MCAEF technique during matrix coating to enhance both the total number of features detected and their corresponding intensities for a single experiment.

Methods

Animals

Premetamorphic Taylor and Kollros stages[130] III-V *Rana catesbeiana* tadpoles of mixed sex were caught locally by Westwind Sealab Supplies in Victoria (BC, Canada) and were maintained in accordance with the guidelines of the Canadian Council on Animal Care and the University of Victoria under permit #2011-030. The exposures were set up in 8 L polypropylene buckets containing three tadpoles per bucket. There were two experimental groups: a control group which were immersed in 400nM sodium hydroxide (NaOH) (ACP Chemicals Inc., Saint-Leonard, QC) and a treatment group which received 50 nM thyroxine (T_4; Sigma-Aldrich, Oakville, ON, Catalog #T2501, CAS 6106-07-6) in 400 nM NaOH. Both exposures took place for 48 h at 24°C, pH 6.8-7.0. Euthanasia was performed using 0.1% (w/v) tricaine methanesulfonate (MS-222) (Syndel Laboratories Ltd., Vancouver, BC) buffered with 25 mM sodium bicarbonate (Bio Basic Canada Inc., Markham, ON). Six tadpoles from each exposure were randomly selected for MALDI-MSI analysis. Tadpoles were frozen on dry ice immediately after euthanasia and then stored at -80 ˚C prior to sectioning.

Tissue Sectioning and Matrix Coating

Tissues were prepared as previously described.[40] A workflow is presented in Figure 15. Tadpoles were cryostatically sectioned to 25 µm at -20 C in a Microm HM500 cryostat and thaw mounted onto indium-tin oxide (ITO)-coated glass slides (Bruker Daltonics, Bremen, Germany). For metabolomic studies, no wash step is performed on the tissues.

Optical images were captured prior to matrix deposition on an Epson Perfection 4490 Photo Scanner. Quercetin (2.6 mg/mL in 80% methanol and 0.01% ammonium hydroxide; Sigma Aldrich, St. Louis, USA) was deposited using the MCAEF technique (as described above) in an ImagePrep (Bruker Daltonics, Bremen, Germany) automated electronic matrix sprayer. Matrix coatings were comprised of a 3-sec spray, 60 sec incubation, and a 90-sec drying per cycle with a total of 30 cycles.

MALDI-MSI

MALDI-MSI data were acquired on an Apex-Qe 12-T Hybrid Quadrupole-Fourier transform ion cyclotron resonance (FTICR) instrument in positive ionization and detection modes. Data were acquired with Bruker's apex Control FlexImaging software. Spectra mass ranges included m/z from 200 to 2300 with broadband detection and a data acquisition size of 1024 kilobytes per second. The instrument was equipped with an Apollo dual-mode electrospray ionization (ESI)/MALDI ion source, with a 355 nm and 200 Hz solid-state Smartbeam Nd:YAG UV laser (Azura Laser AG, Berlin, Germany). The diluted ESI tuning mix (Agilent Technologies, Santa Clara, CA) solution was prepared in 60:40 isopropyl alcohol: water, both containing 0.1% formic acid for calibration of the instrument. For imaging, a raster step size of 200 μm was used with 100 laser shots summed per array position.

Data Processing

In order to determine objective borders between tissue types within a tadpole, spatial segmentation was performed. This was done by exporting data from FlexImaging to .img format and then imported into Cardinal package[75] using R[114] and RStudio[115]. Spectral pre-processing steps included: normalization by total ion count, baseline reduction in blocks of 50 m/z, peak picking based on a signal to noise ratio of 3, peak alignment across pixels to 5ppm, and peak filtering to remove mass features that occurred in less than 2% of all pixels. Spatial segmentation using spatial shrunken centroids was used for separating pixels into groups by comparing the similarity and differences of the profile in each mass spectrum. A total of 20 segments were chosen. Segmented images were then compared to optical images for tissue type identification. The following five tissue types were reliably identified using this method in all tadpole sections: brain, eye, liver, notochord, and tail muscle.

Using the previously identified tissue types, five individual spectra from each tissue were exported from FlexImaging to Bruker's DataAnalysis 4.0. For batch internal mass calibration, peak deisotoping, monoisotopic "peak picking", and peak alignment, a customized VBA script was used as described elsewhere.[112] Exported CSV files were aligned to 3 ppm and summarized for each of the five tissue types for each tadpole. FlexImaging 2.1 was used to reconstruct ion heat map images of detected metabolite mass features. Prior to image extraction, mass spectra were normalized to have the y-mean:y-max ratio set to 0.5. This is done to exclude noise from the ion heat map images for better visualization. Absolute intensities for each metabolite mass feature were individually chosen to most accurately show the intensities across the tadpoles. The scale chosen for each mass feature is independent of other mass features.

Statistical analysis and annotation

Non-parametric Mann-Whitney U analysis was performed on each metabolite mass feature comparing control to TH-exposed tadpoles to determine significant ($p < 0.05$) features. Mass features that occurred in less than three TH-treated tadpoles or less than three control tadpoles are not considered as a guaranteed detection or putative identification for the purposes of this experiment because they are not statistically robust enough. Measured mass features (m/z values) from both the statistically robust total detected as well as the significantly changing were matched to the MassTRIX database[131,132] to attain possible metabolite identities. $[M+H]^+$, $[M+K]^+$, and $[M+Na]^+$ ion forms were allowed for positive-ion mode during database searching with an allowable mass error of ± 3ppm.

Results & Discussion

The Cardinal R package was very applicable for the type of data processing necessary for such a large dataset. Manual interpretation and data processing of the twelve tadpoles would have taken a considerable amount of time and most likely been plagued with user bias. Something unique about the Cardinal package is that it performs spectral processing directly to the imaging spectra. Typically, in an experiment, only profiling data is submitted to spectral processing and imaging data is left relatively un-touched prior to exporting the reconstructed ion heat maps. The spectral processing workflow used for the current experiment was as follows: normalizing to the total ion count of the spectra, baseline reduction in blocks of 50, peak picking with a simple algorithm and a signal to noise ratio of 3, peak alignment to 5 ppm across all spectra for a single tissue, and peak filtering to remove mass features that occur in less than 2% of all spectra for a single tissue. During the peak alignment step, the data is converted to centroid peaks rather than profiling peaks. This spectra processing was very beneficial to perform prior to statistical analysis. The processing workflow is shown in Figure 16 depicting the average mass

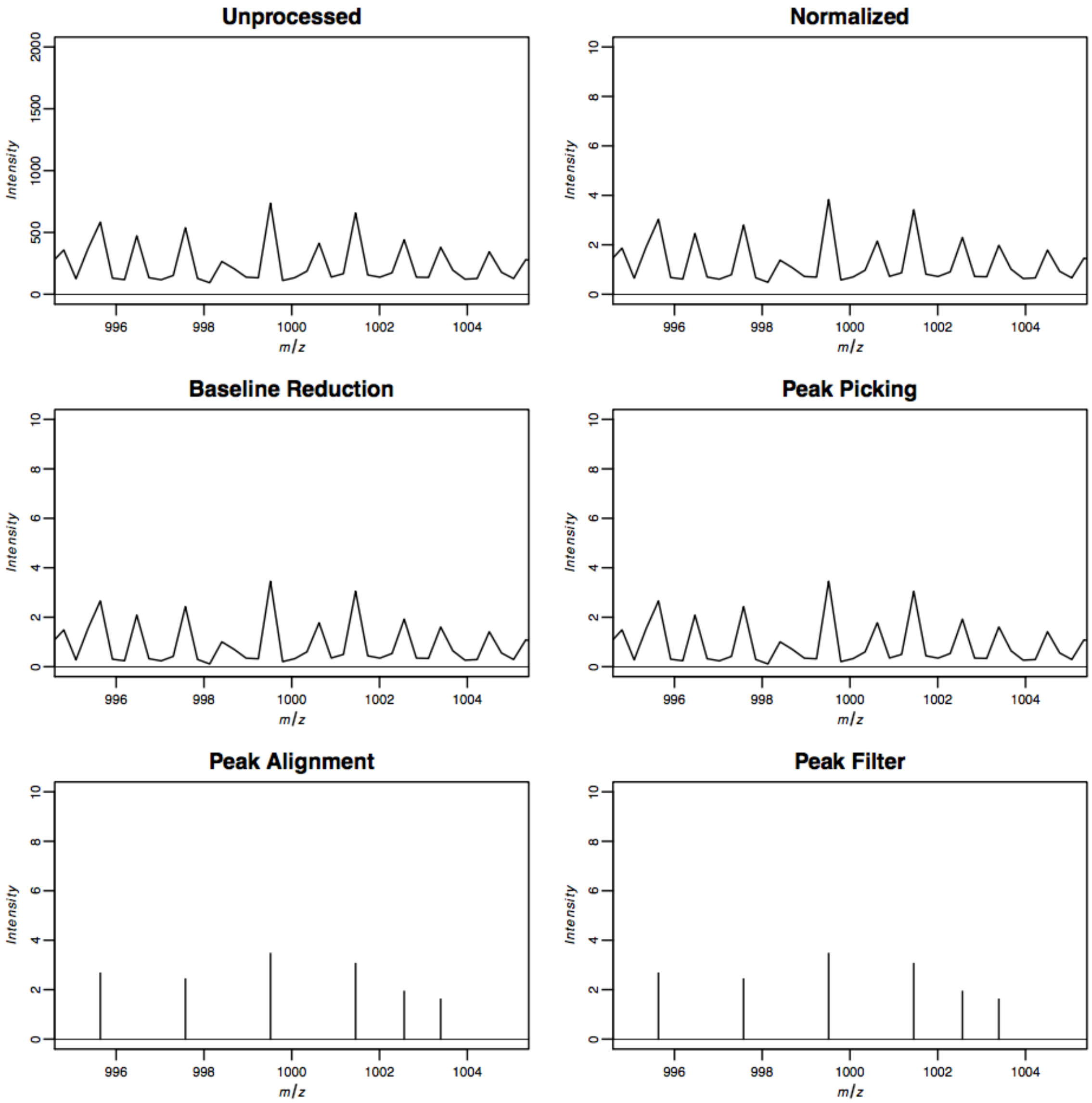

Figure 16 - A representative image of spectra processing performed by the Cardinal package on the tadpole imaging data. Spectra shown are average spectra across the entire tissue.

spectra across a tissue for representative tadpole. Special note was focused on the mass features at ~1001.45 m/z. This mass was selected for monitoring as it was a relatively low intensity mass feature but localized to the eye and brain region of the tadpole. As a confirmation, the Cardinal reconstructed ion heat maps were viewed at each step during the spectral processing to confirm this mass feature was not lost (Figure 17).

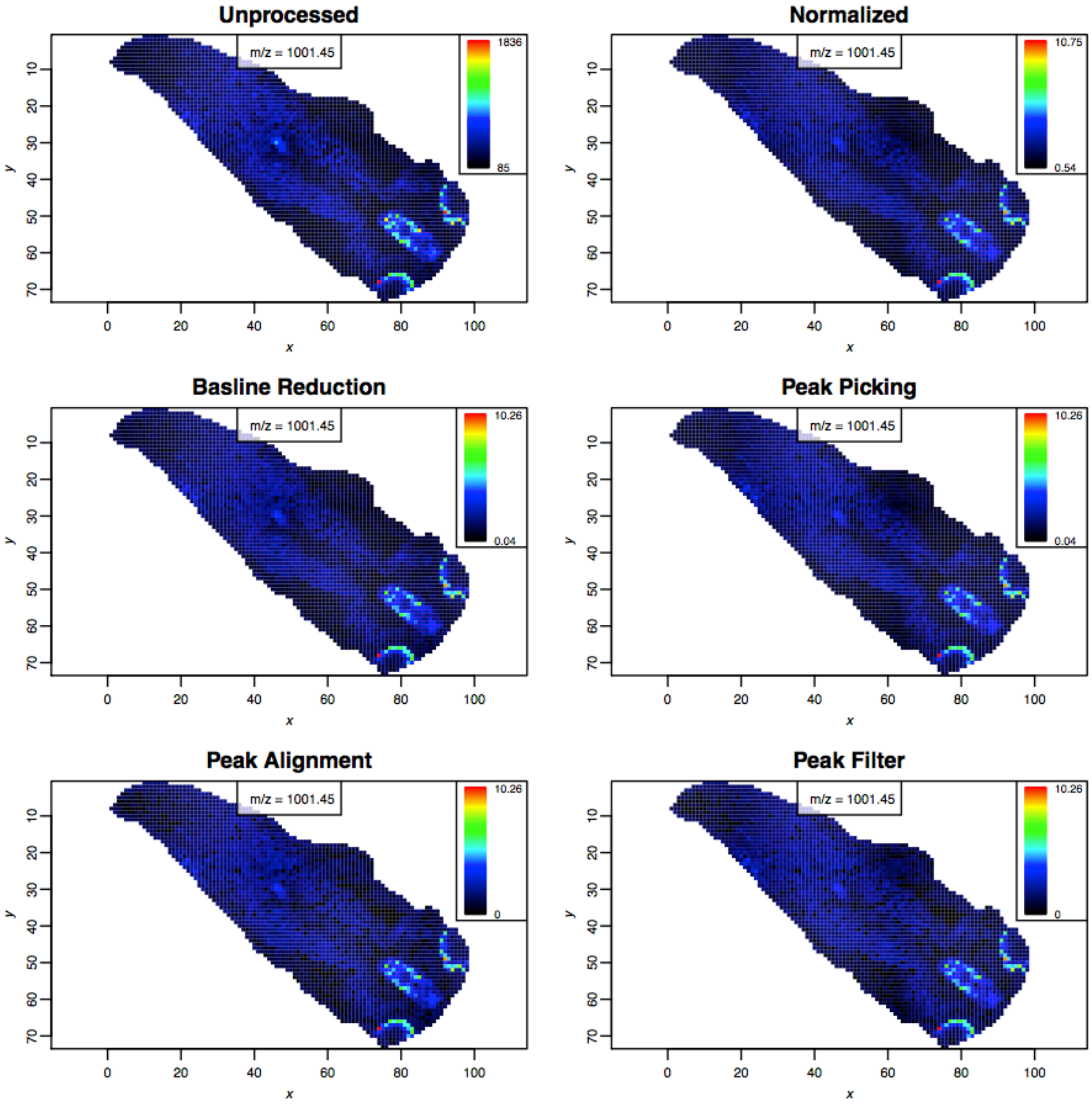

Figure 17 – A representative image of Cardinal reconstructed ion heat maps during spectral processing performed by the Cardinal package on the tadpole imaging data.

Once spectral processing was complete, the next step was to move onto statistical analysis. Spatial segmentation is a process similar to Principle Component Analysis that creates different segments that each individual spectrum is classified into based on the profile of the spectra, including both m/z and intensity in the profile. As imaging datasets contain not only m/z and intensity information, but also relative x- and y-coordinates of the spectra, an additional level of information is incorporated into the statistical analysis. Spatial shrunken centroids, which is a spatial segmentation based on k-means clustering was performed. The k-means clustering spatial segmentation was also available in the Cardinal package, however due to the size and complexity of the imaging datasets, the spatial shrunken centroids segmentation was chosen.

There was a total of three parameters that needed to be optimized for the spatial segmentation: *r*, which is the radius of spectra around the spectrum of interest that is used for profile comparisons for the classification; *k*, which is the total number of segments that the imaging dataset will be classified into; and *s*, which is a ± value used to create a variable number of segments in the imaging dataset, if the algorithm has too many or has run out of segments during classification of the spectra. An *r* value of 2 and 3 and a *k* value of 15 and 20 were tested during optimization (Figure 18). The *s* value was not optimized as the Cardinal R package documentation highly recommended a value of 2 when managing ~20 segments. Careful examination of the different tissue sections of interest (brain, eye, liver, notochord, and tail muscle) was made to ensure that all of the tissues were present in the spatial segmentation and no tissues were lost to a larger grouping. The final set of parameters was chosen to be *r*=2, *k*=20, *s*=2. This set of parameters was used for all spatial segmentations performed in this experiment.

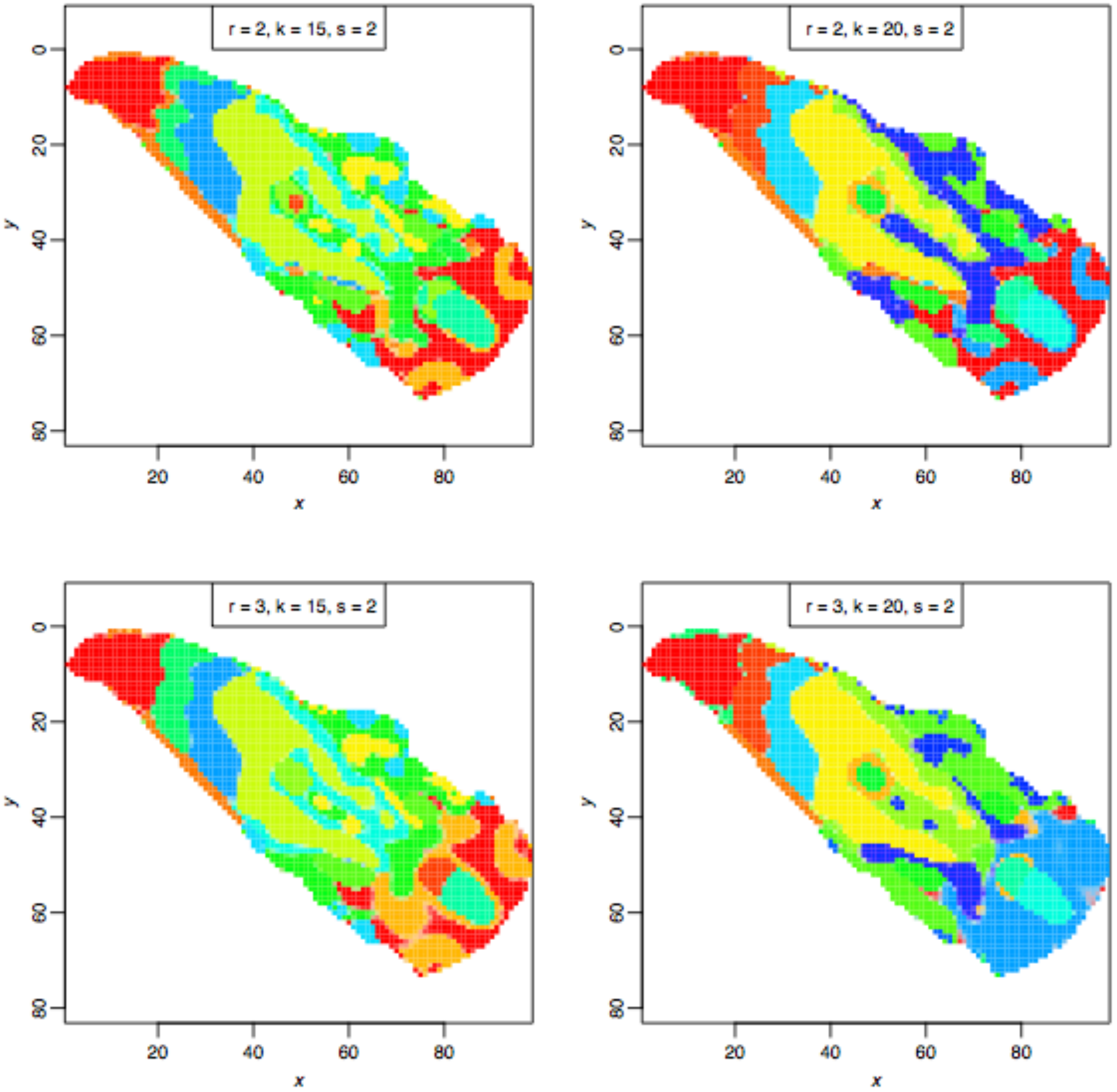

Figure 18 – Cardinal spatial segmentation images using different values for the *r* (radius) parameter and *k* (number of segments) parameter during spatial segmentation optimization.

After the final spatial segmentation parameters were chosen, segmentation was performed to all twelve tadpole imaging datasets. Various outputs from the spatial segmentation could be viewed or exported based on what the purpose of the spatial segmentation was to the user. For this experiment, the aim was to find metabolite mass features that were statistically significant in different tissues of the tadpole after thyroid hormone induced metamorphosis. For this reasoning, the average mass spectrum for segments of interest were viewed. This was for the general purpose of seeing if there were any regions of the spectra from one segment that showed strong differences compared to other segments (Figure 19). Another useful export from the spatial segmentation is a value labelled “t-statistic”. This is a numerical rating given to each mass feature in the spectrum for an individual segment that indicates its relative importance in creating that segment. Mass features with a higher t-statistic value were more influential to separating that tissue apart from the remaining tissue in the tadpole than other mass features. Figure 19 shows a representative tadpole and the brain tissue segment from the spatial segmentation. Both the average mass spectrum and t-statistic value graph are shown. The t-statistic values for each tissue of interest for all twelve tadpoles was exported so that a general list of mass features influential to the tissues of interest could be created.

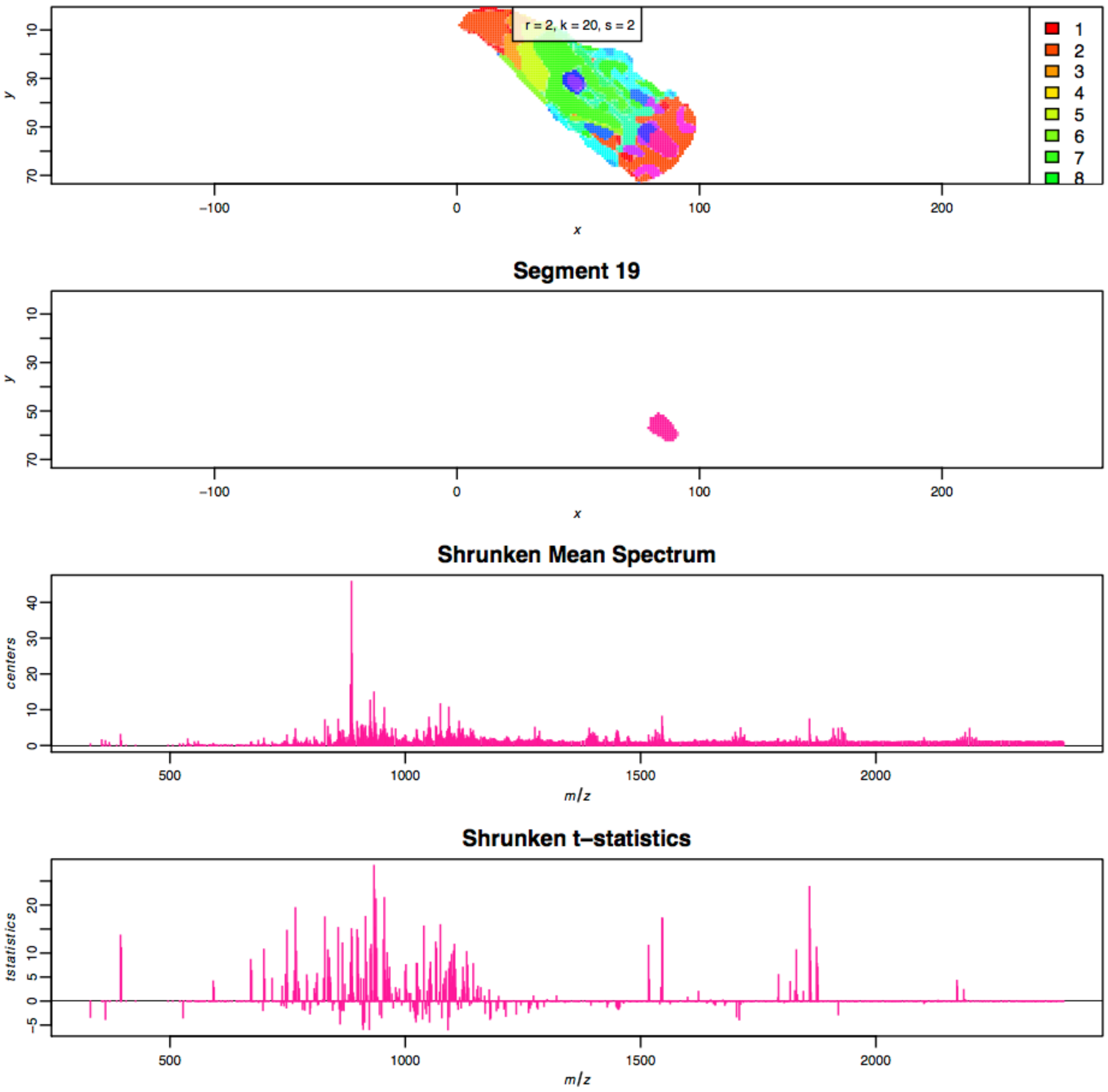

Figure 19 – Representative exports from the Cardinal package including (top image) the total segmentation; (second image) an individual segment, for this example it is the brain; (third image) the mean spectrum from the individual segment from the shrunken spatial segmentation; and (bottom image) the t-statistic value for each mass feature relative to the individual segment

Spatial segmentation was critical for determining which spectra belonged to which tissue in each tadpole. Spectra were not exported directly from Cardinal and the spatial segmentation because these spectra had been averaged across the entire tissue and no longer retained the high mass resolution characteristic from the FTICR detector. The spatial segmentation images were used for direct comparison when exporting individual spectra from FlexImaging to DataAnalysis for further in-depth spectra analysis and metabolite mass feature putative identification. Over 5,000 metabolite mass features, that were present in at least three of the six control and three of the six TH-treated tadpoles, were detected (Table 3). The brain, eye, liver, notochord, and tail muscle, each had ~1,000 mass features, including those which were unique to the individual tissue (Figure 20) and others that were common between multiple tissues. Less than half of these mass features detected in each tissue were given a putative annotation using MassTRIX. One hundred and thirty-six of the total the mass features detected differed significantly upon TH treatment (Table 3). After submission to the MassTRIX metabolomic database, 64 of these significant mass features were putatively identified (Table 3). The full list of significant and putatively identified metabolite mass features can be found in Supplementary Table 7. Out of the five tissues of interest, notochord had the most significantly changing mass features as well as the most putatively identified metabolites. In contrast, the liver, which had a similar total mass feature count to the notochord had the least significantly changing and identified metabolites (Table 3).

Table 3 – A summary of the number of metabolite mass features detected in each tissue type in all tadpoles in positive mode. *Total number of mass features detected in a minimum of 3 tadpoles in each of the control and treatment groups. **Significantly different mass features based on Mann-Whitney U post-hoc analysis with a p-value < 0.05.

Tissue	**# of metabolites detected***	**# of significant****	**# of down-regulated**	**# of up-regulated**	**# of significant putative ID’s**
brain	1210	16	5	11	4
eye	1121	26	18	8	10

liver	799	8	6	2	2
notochord	1059	54	12	42	33
tail muscle	1035	32	27	5	15

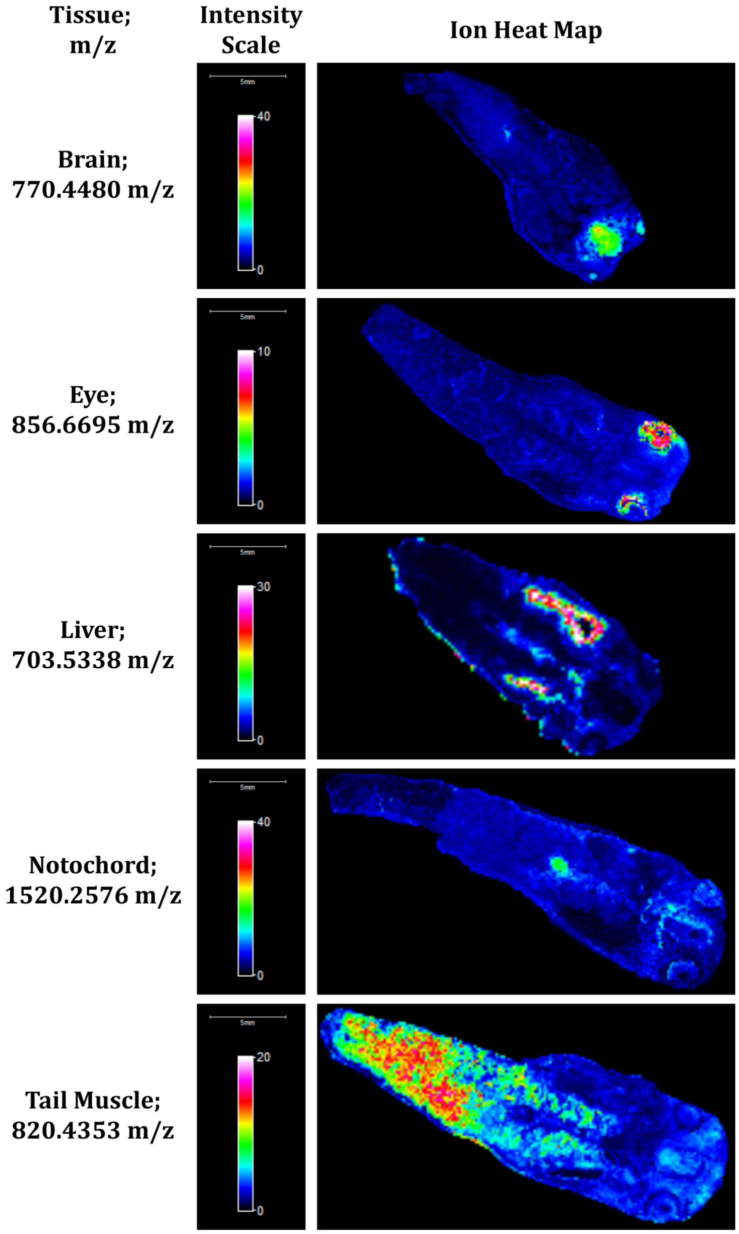

Figure 20 – Representative reconstructed ion heat maps of metabolites that localize to a single tissue of interest. Ion heat maps were chosen from any of the twelve tadpoles as a representation of the localization of the metabolite mass feature.

There was an even split between up or down regulated metabolites that differed significantly upon TH treatment, with 68 increasing and 68 decreasing. Within the particular organs, however, there were more mass features significantly increasing in the brain and the notochord, whereas there were more mass features significantly decreasing in the tail muscle, liver and eye. Representative boxplot graphs of intensities from

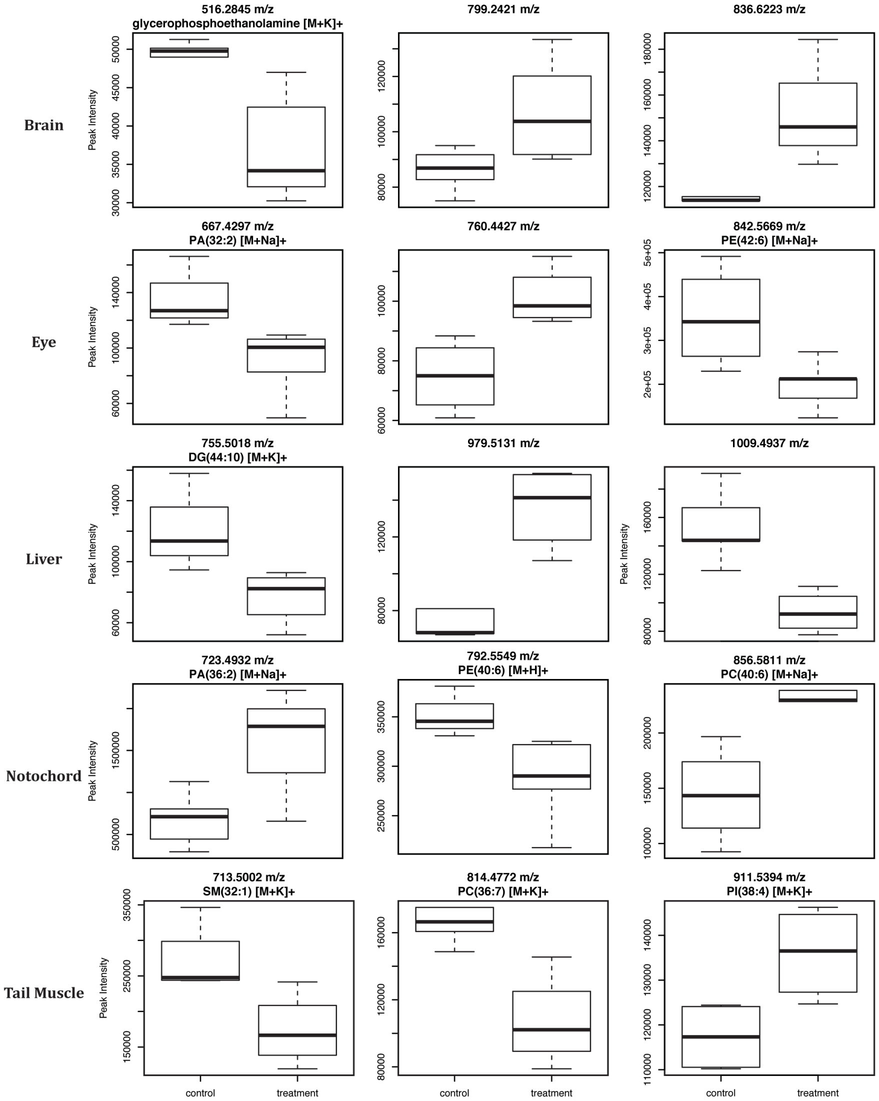

Figure 21 – Representative boxplot graphs of significant (MWU, $p < 0.05$) metabolite mass features from: A) brain, B) eye, C) liver, D) notochord, and E) tail muscle tissues. Feature characteristics including m/z, putative identifications are indicated at the top of each graph. The thick bar represents the median and the whiskers represent the median absolute deviation (MAD).

significant metabolite mass features are shown in Figure 21. All graphs shown in this figure are significant, $p < 0.05$. These are paired with reconstructed ion heat maps (Figure 22) allowing visualization of the tissue specific relative abundancies of mass features between tadpoles. Graphs and heat maps shown are a subset of the total number of significant mass features and were chosen to demonstrate the general trends of both increasing and decreasing intensities of the metabolite mass features after treatment with TH.

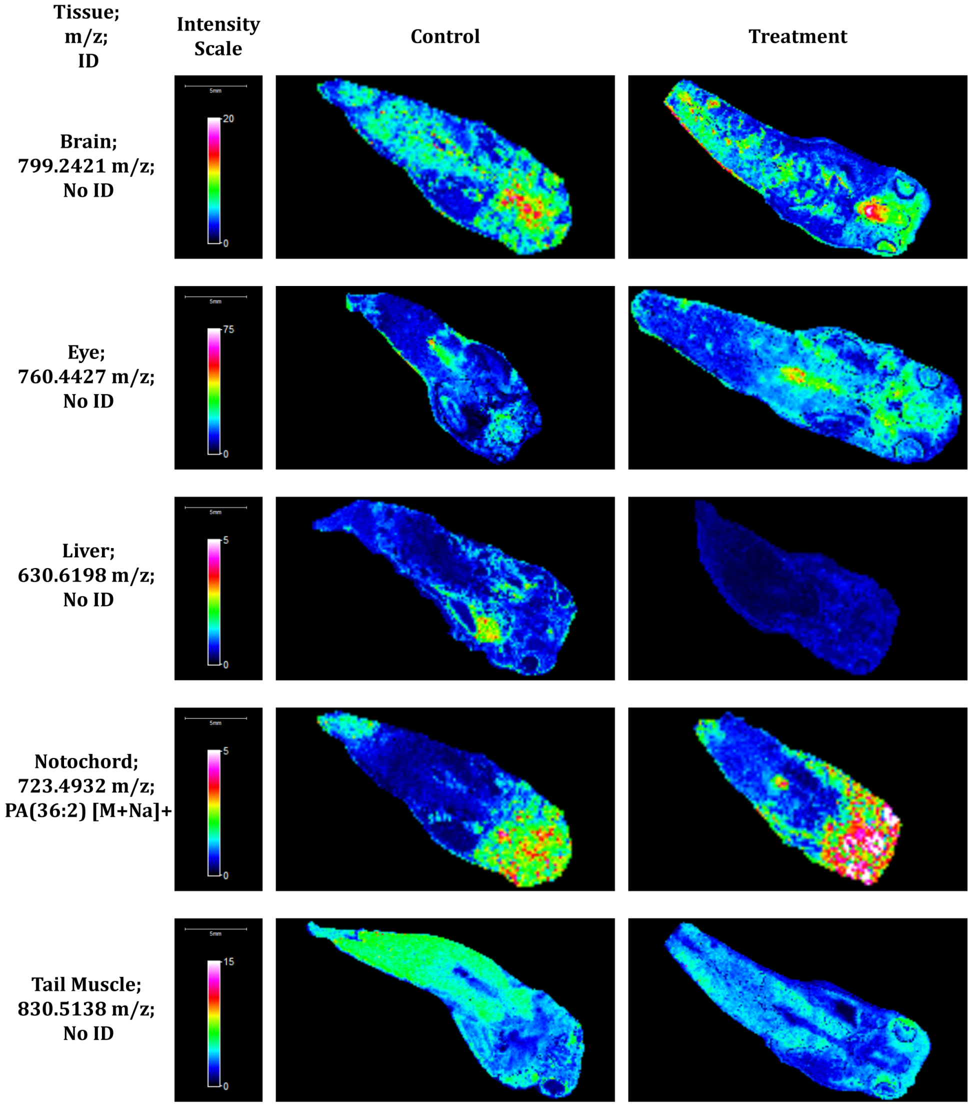

Figure 22 – Representative reconstructed ion heat maps of metabolites from each tissue region of interest (brain, eye, liver, notochord, and tail muscle). One ion heat map was

chosen from the set of control tadpoles and one ion heat maps was chosen from the set of thyroid hormone treated tadpoles. Each metabolite mass feature chosen was found to be significantly increased or decreased after thyroid hormone treatment ($p < 0.05$). Visualization of the mass features shows the localization of each metabolite to a specific tissue region and its increase or decrease in the treatment tadpoles.

The putative identification of mass features highlighted a few key metabolites of interest. All putative identifications, along with median peak intensities and corresponding median absolute deviation (MAD) values can be found in Supplementary Table 7. A high percentage of the total identified mass features in each of the organs were lipophilic compounds, mainly the membrane associated phospholipids: phosphatidylcholines (PCs) phosphatidylethanolamines (PEs) phosphatidylserines (PSs), phosphatidylinositols (PIs), and phosphatidylglycerols (PGs). Due to the identical mass-to-charge ratios of the many structural isomers of these compounds they were only identified to their class, total number of carbons, and total number of double bonds. In each of the organs these lipid compounds also made up a high proportion of the significantly differing metabolites. Other significantly changing metabolites of interest that were putatively annotated were sphingomyelins (SMs) which were changing in all tissues except the liver. As well, heme was decreased in the liver. Representative boxplot graphs and reconstructed ion heat maps of these metabolite mass features can be found in Figure 23.

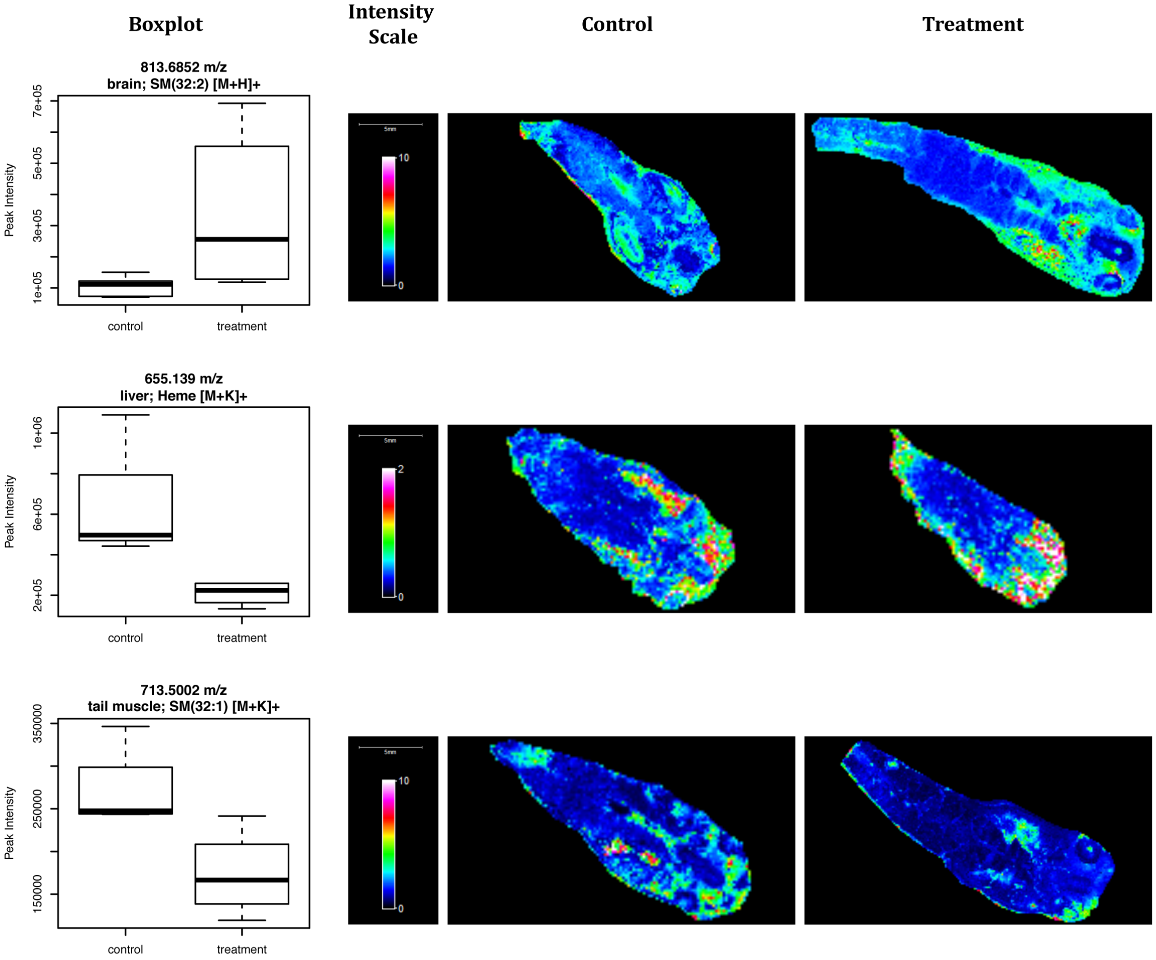

Figure 23 – Representative boxplot graphs and representative reconstructed ion heat maps of metabolites of special biological interest. Feature characteristics including m/z, putative identifications are indicated at the top of each graph. The thick bar represents the median and the whiskers represent the median absolute deviation. One ion heat map was chosen from the set of control tadpoles and one ion heat maps was chosen from the set of thyroid hormone treated tadpoles. Each metabolite mass feature chosen was significantly increased or decresed after thyroid hormone treatment ($p < 0.05$).

Metamorphosis is an extensive process where drastic physiological and biochemical changes occur allowing the transition of a tadpole to a frog. This expansive reconstruction of a fully differentiated animal involves tight regulation and synergism of each different tissue and organ as they undergo cellular reprogramming, proliferation, and apoptosis. Although this TH-induced process is instilled genetically, through the modulation of TH response genes, the resultant phenotypic changes can be measured through metabolomics.

The present study used MALDI-MSI to capture a snapshot of the metabolomic environment in metamorphosis-induced tadpoles. Thousands of different mass features were detected highlighting the high resolution of this technique. Of the total mass features detected and annotated, a high proportion were lipophilic molecules corroborating what was found in the serum metabolome of *R. catesbeiana*[122] as well as the human metabolome[133] giving a higher degree of confidence in accuracy of mass feature detection. Of the 5000 mass features detected, only 136 metabolites were found to show significant difference between control and thyroid hormone treatment. Of the significant metabolites, only 64 were putatively identified, making biological interpretation more difficult and illustrating the need for improvement of metabolomic databases

The ability of MALDI-MSI to retain location information of detected mass features allows for visualization of the pleiotropic effects of TH signaling in each tissue upon the induction of metamorphosis. The metamorphic program is known to be established in the transcriptome at 48 h.[134] By this time point TH response genes are induced and metamorphosis can no longer be stopped by inhibitors.[135] The transcriptomic changes that occur result in downstream alterations of the metabolomic environment which can be seen as the phenotypic response to the initiation of metamorphosis. In the present study, we show that there are metabolomic changes occurring in each organ at 48 h of TH-induced metamorphosis. The total count of significantly changing metabolites was substantially lower than what was detected in the previous metabolomics study of the serum by Ichu et al.[122] Ichu et al. detected a total of 4528 metabolites, of which 3329 were found to be significantly changed upon thyroid hormone treatment.[122] It should also be considered that the data for the present study was acquired only in positive mode which misses all the mass features that favor negative ionization.

Each organ has a different fate in metamorphosis and responds locally to TH which is shown by the ability for individual organs to respond to TH in culture.[135–137] This direct response of the tissue is reflected in the present study by the distinct changes in the metabolomic profiles of the eye, brain, notochord, liver, and tail muscle upon TH treatment. The tissue with the most significantly differing mass features was the notochord. This tissue plays a very important role in vertebrate embryogenesis with involvement in depicting body axis orientation[138], patterning of surrounding tissues and providing structure throughout development[139]. Its role in postembryonic development, however, has not been well studied. In the caudal end of the animal, the notochord must undergo programmed cell death along with the tail. The notochord also plays an integral role in the proper development and segmentation of the spinal cord.[140] The multiple roles that it likely plays in metamorphosis explains the presence of 42 up-regulated metabolite mass features compared to only 12 down-regulated metabolite mass features of the notochord to TH.

One of the most overtly dramatic physiological changes that occur in the transition to a frog is the resorption of the tail. This involves the coordination of the different types of tissue including epidermal, muscular, nervous, and structural, to all undergo highly regulated programmed cell death simultaneously. A higher number of metabolite mass features are down-regulated in the tail muscle (27 down-regulated compared to only 5 up-regulated) likely reflecting the arrest of many cellular processes to conserve energy as continuation of growth and differentiation is unnecessary. One of the many metabolic features that were specifically affected in the tail muscle was the decrease in SM. The important role that SMs play in lipid signaling is becoming more appreciated in recent years. One of their signaling pathways includes their catabolism to ceramide which is likely involved in the decision for cells to undergo apoptosis in the tail muscle.[141,142]

Unlike the tail muscle, which is not present after metamorphosis, other tissues are present in both the tadpole and the frog but are completely reprogrammed to accommodate the niche transition that occurs. One such organ is the liver which undergoes major remodeling to switch from an ammonotelic to a ureotelic system of nitrogen excretion as well as a transition from larval to adult hemoglobin.[143,144] This reprogramming is seen in the transcriptome where after 48 h of TH exposure there is a massive transcriptomic response.[145] Under the same conditions at the metabolomic level, however, there was only eight mass features that significantly changed upon TH treatment. A similar limited response to TH was found by Suzuki et al. with respect to PC, PE, PI, PG and PS composition in the *R. catesbeiana* liver after 72 h of treatment.[123] The response of this organ to TH may still be at the transcriptomic level with metabolite changes not yet manifesting at this early time point like the many liver metabolic changes that occur closer to metamorphic climax.[119] One metabolite of interest that significantly responded to TH in the liver was heme. The observation of downregulation may be because heme oxygenase activity in the liver, involved in heme catabolism, increases by 2-fold after 48 h of TH exposure.[146] As well, it may be a resultant metabolic product of the transition from larval to adult hemoglobin that occurs in metamorphosis.[143]

Another organ that is extensively remodeled is the brain to accommodate changes in locomotion and behavior. The parts of the brain associated with the tissues undergoing apoptosis degenerate. Concurrently, nerves associated with limbs and the various reprogrammed tissues must be synthesized.[119] The complicated reconstruction of the brain is demonstrated in its metabolomic response to TH. The degenerating regions of the brain lead mostly to the downregulation of metabolites. The *de novo* constructed regions, however, are associated more with the upregulation of metabolites. One such upregulated metabolite is SM. There are two main routes of SM signaling that have been well studied. The pro-apoptotic conversion to ceramide, mentioned above, and the conversion to sphingosine-1-phosphate which is involved in inflammation and angiogenesis.[147] As cells are either undergoing apoptosis or being synthesized in the brain during this period it is likely that SMs play a crucial role in both pathways. In the parallel postembryonic period of humans, TH signaling is crucial for proper development of the brain and disruption can lead to serious developmental disorders such as cretinism.[148,149]

Although all the different tissues respond very distinctively to TH signaling, phospholipids seem to play an important role throughout the tadpole. All the tissues except for the limited response of the liver, had either up or down regulation or both of varying classes of PCs, PIs, PGs, PEs and PSs. These lipophilic compounds make up the largest portion of significantly changing metabolites in response to TH treatment, as presented in the current study, as well as in natural metamorphosis.[122] This indicates that that they most likely are very important in metamorphosis. Their role in this very complex process, however, is not well understood. Changes in up or down regulation of these lipids likely correlate with switching of cell types in the tissues that are being reprogrammed, as different cell types have different requirements for membrane fluidity and structure. In the case of the tail muscle, the majority of the phospholipids are decreasing likely representing the decrease in cells due to programmed cell death.

Conclusions & Future Directions

The current MALDI-MSI study was successful in giving insights into the metabolome of TH-induced metamorphosis in *R. catesbeiana*. The next steps of metabolomic research on the metamorphosing tadpole will be to increase total number of metabolites identified and annotated by performing a secondary analysis of the tadpole tissue by LS-MS/MS.[40,122] Each of the five organs of interest, which are all set for different fates, respond independently to TH signaling given the differences in metabolites that were identified as well as the general differentiation of mass feature regulation. These discoveries demonstrate the pleiotropic effects of TH-signaling throughout the pre-metamorphic tadpole and provide a basis for what metabolic pathways are critical in the initiation of metamorphosis.

Chapter 4: Method Optimization of Metabolomic Analysis of Formalin Fixed Paraffin Embedded Colorectal Liver Metastasis by MALDI-MSI for Biomarker Discovery

Introduction

Colorectal cancer is within the group of cancers that are leading for both incidence and mortality rates for women and men worldwide.[107] Colorectal cancer has rates of 14.5% and 11.5%, for incidence rates in men and women, respectively and 12.0% and 11.3% for mortality rates in men and women, respectively, in Canada.[107] These rates put colorectal cancer in the highest three cancers in Canada. This trend is also seen in previous Canadian cancer statistics.[150,151] As a result, there are just over 5,000 deaths predicted in Canada from this cancer alone in 2017.

The easiest way to increase quality of life and survival rates is to have accurate screening tests and early detection methods. However, diagnosis and prognosis tests for these cancers are limited. Carcinoembryonic antigen (CEA) is a colorectal cancer biomarker that initially showed efficient use for therapy prognosis, but has recently been shown to have normal concentrations in stage I colorectal cancer and an inability to differentiate between benign and malignant polyps, inflammatory conditions, and gastric or pancreatic cancers.[152] A need for novel biomarkers to create effective blood screening and prognosis tests is imperative.

Studies to date focus on finding a single genomic, proteomic, or metabolomic biomarker for a disease. This mindset of research can be problematic, because genes, proteins, and metabolites all work together, and therefore should be research as a whole. A new concept for biomarker discovery is “meta-omics”. This large-scale analysis would look for multiple genes, proteins, and metabolites that highly correlate to each other through biochemical mechanisms.[153] Panels of genes, proteins, and metabolites from meta-omic studies have a higher potential for the development of cancer screening tests.

Formalin-fixed and paraffin embedded (FFPE) tissues are the gold standard for preservation in a clinical setting. Once preserved, samples are safe from degradation and can be stored at room temperature for an indefinite amount of time. The downside of FFPE preservation is that formalin causes random inter- and intra-molecular crosslinking to occur between proteins, ribonucleic acid (RNA), and deoxyribonucleic acid (DNA) within the tissue.[154] Paraffin embedding allows for the tissues to be later sliced thinly with a microtome for morphology and pathology studies. However, as paraffin is a wax, FFPE samples cannot be introduced to a mass spectrometer without the paraffin being removed. A common goal among the mass spectrometry community was to unlock FFPE tissues for molecular analysis. Proteomic mass spectrometry research on FFPE tissues began with cleaving the protein crosslinks within the tissue by enzymatic digestion.[155] This experiment worked with homogenized tissue and a liquid introduction of the tissue to the mass spectrometer. Shortly after this experiment was published, an on-tissue enzymatic digestion technique was combined with heat induced antigen retrieval and applied to a MALDI-MSI experiment.[156] This experiment was successful in detecting various proteins from the sample and paved the way for protein analysis of FFPE tissues. A summary of bottom-up proteomic MALDI-MSI experiments that have recently been performed can be found in Supplementary Table 3, Supplementary Table 4, and Supplementary Table 5. This table focuses on protocols that have steps that are novel or differ greatly from other protocols.

More recently, focus was placed on metabolomics analysis of FFPE tissues. This is considered to be quite difficult, as the process of antigen retrieval and paraffin removal often washes away the majority of metabolites from a tissue. This is primarily due to the paraffin removal step which requires xylene, a strong organic solvent, to remove the wax from the tissue. Three experiments by the same research group have been published that analyzed metabolites in FFPE tissues. The first publication was a proof-of-principle experiment to show that it was possible to analyze metabolites in FFPE tissues.[157] A comparison was made between the metabolomics analysis of a tissue that had been split for fresh frozen and FFPE found a 72% overlap between the metabolomics profiles.[157] The second publication was a formal protocol in the journal Nature Protocols.[158] This publication went into great detail to describe each step required for the analysis of metabolites in FFPE tissues.[158] The third publication focused on comparing the suitability of different instruments for metabolomics analysis of FFPE tissues.[61] This experiment compared a Time of Flight (TOF) mass spectrometer to a Fourier-Transform Ion Cyclotron Resonance (FTICR) mass spectrometer and found that FTICR instruments outperform TOF for low-mass analyses.[61]

Methods

Reagents

Xylene, quercetin, HPLC-grade methanol, HPLC-grade ethanol, and ammonium hydroxide (NH_4OH) were purchased from Sigma-Aldrich (St. Louis, MO, USA). ESI tuning mix was purchased from Agilent (Agilent Technologies, Santa Clara, CA, USA).

Samples

After attempted communication with multiple professors at McGill University, a successful collaboration was made with Dr. Mark Basik from his biobank samples of colorectal liver metastasis. All samples in the biobank are FFPE and stored at room temperature. Tissues were sectioned on a microtome to 5-µm and water-mounted onto ITO-coated slides. Tissues were heat-fixed to the slide at 42 ˚C and then stored at room temperature. Sets of 10 pre-sectioned tissues on ITO-coated slides were sent from McGill from the following patients: four colorectal liver metastasis samples with tumour cellularity ranging from 25-70% with two of the samples coming from the same patient but different tumour. Samples were anonymized prior to receiving them and contained no patient data. University of Victoria Anonymized Human Biological Materials Ethics (Protocol Number 16-434) and University of Victoria Biosafety (Registration Number 85268-004) were obtained for use of the tissues.

Deparaffinization

Paraffin embedding was removed by washing the tissues in fresh xylene two times for 5 minutes each in Coplin jars. After removing the slide from the xylene, it was allowed to air dry for a minimum of 10 minutes in a fume-hood while matrix deposition was set up.

Matrix Coating

Quercetin was prepared in a concentration of 2.6 mg/mL in 80% methanol in 0.1% NH_4OH. The quercetin matrix was deposited using an ImagePrep electronic matrix spray generator. Typically, a total of 10 mL was made at a time. As quercetin is not a standardized matrix, an in-house developed matrix coating method was used (30 cycles of 3 second spray, 60 second incubation, and 90 second drying time). The MCAEF technique was used during matrix deposition. A uniform electric field at an intensity of +600 V/m was applied to the tissue in positive-ion mode and negative-ion mode (Figure 4).

MALDI-MSI

All mass spectra were acquired on an Apex-Qe 12-Tesla hybrid quadrupole-FTICR mass spectrometer ((Bruker Daltonics, Billerica, MA, USA). The instrument was equipped with an Apollo dual-mode ESI/MALDI ion source. The instrument’s laser source was a 355-nm solid-state Smartbeam Nd:YAG ultraviolet laser (Azura Laser AG, Berlin, Germany).

A calibration solution was prepared by adding 10 µL of Agilent "ESI tuning mix" solution with 10 mL of 75% ACN with 0.1% formic acid. The calibration was directly infused into the ESI side of the ion source for instrument calibration. The instrument was calibrated before every experiment performed.

All mass spectra were acquired over the mass range of 200-2200 m/z with a data acquisition size of 512 kilobytes per second. Imaging data was acquired with one scan at 100 laser shots per scan with the minimum raster step size of 200-µm. Imaging spectra were acquired with Apex Control, Hystar Control, and FlexImaging 2.1 (Bruker, Bremen, Germany). Teaching points were generated with a Tipex Wite-Out pen to enable the instrument to have an accurate slide position for spectra acquisition.

H&E Staining

H&E stains were provided by the Basik laboratory with the samples that were provided. A standard H&E staining protocol was followed. A pathologist marked the cancerous regions with a blue marker.

Data Analysis

Reconstructed ion heat maps were viewed and created using FlexImaging. Using this software, reconstructed ion heat maps were created. Images were exported as JPEG files for viewing.

Statistical analysis and spatial segmentation of imaging data was done by exporting data from FlexImaging to .img format and then imported into Cardinal package [75] using R [114] and RStudio [115]. Spectral pre-processing steps included: normalization by total ion count, baseline reduction in blocks of 50 m/z, peak picking based on a signal to noise ratio of 3, peak alignment across pixels to 5ppm, and peak filtering to remove mass features that occurred in less than 2% of all pixels. Spatial segmentation using spatial shrunken centroids was used for separating pixels into groups by comparing the similarity and differences of the profile in each mass spectrum. A total of 10 segments were chosen as this gave for the best separation of the pathologist pre-defined cancerous regions.

Individual mass spectra from the imaging datasets were exported from FlexImaging and were then processed using DataAnalysis 4.0 (Bruker, Bremen, Germany). Batch internal mass calibration, peak de-isotoping, and monoisotopic peak picking were performed using a customized VBA script within DataAnalysis. Measured mass features were matched to the MassTRIX database[131,132] to attain possible metabolite identities. $[M+H]^+$, $[M+K]^+$, and $[M+Na]^+$ ion forms were allowed for positive ionization mode and [M-H]- ion form was allowed for negative ionization mode during database searching with an allowable mass error of ± 3ppm.

Results & Discussion

FFPE tissues were rather difficult to work with. The most troubling aspect of the tissues was the paraffin removal step. Xylene is a very strong organic solvent that works very well to remove the paraffin wax from the tissue, but at the same time it also removes metabolites and lipids present in the tissue.[157] The goal of this experiment was to determine if there were any remaining metabolites in the tissue, and if these metabolites were able to differentiate between the pathologist defined cancerous regions.

Figure 24 depicts the major results of the experiment. This diagram shows optical images, H&E stains, total segmentation images, cancerous segmentation images, and representative ion heat map images of MALDI-MSI metabolomic datasets from two colorectal liver metastasis samples in (A) positive ionization mode and (B) negative ionization mode. Optimizing the segmentation parameters was difficult to separate out a cancerous region that resembled the pathologist defined cancerous regions from the H&E images. A total of 10 segments with variable of ±2 and a radius of 2 were chosen for final parameters. The number of segments was chosen as 10 to allow for background segments to be pulled out, as well as the natural heterogeneity of human tissue to be accounted for. Experimentation was performed with 5 more and 5 less segments and 10 segments showed to have the highest correlation with the defined cancerous regions without adding or removing too much of the regions. One note to point out is that the H&E image was performed on a tissue section that was an unknown number of sections away from the tissue sections that had MALDI-MSI performed. Cancer tumours are heterogeneous and

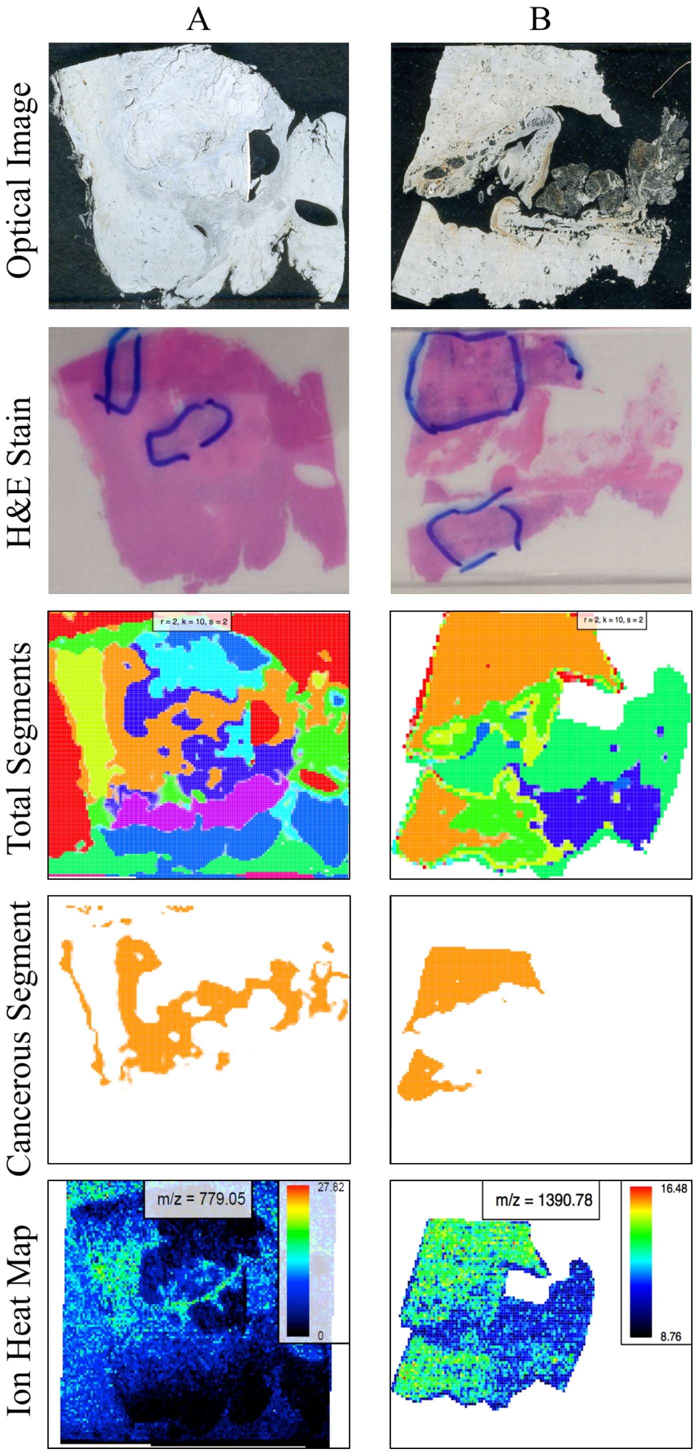

Figure 24 – MALDI-MSI metabolomic images of (A) a colorectal liver metastasis sample analyzed with quercetin in positive ionization mode and (B) a colorectal liver metastasis sample analyzed with quercetin in negative ionization mode. Images include the optical image, an H&E stained image, total segmentation image, the individual cancerous segment image, and a representative reconstructed ion heat map of an influential metabolite mass feature.

cancerous tissue. However, a general region of tumour can be inferred. As a result, one segment from each tissue was determined to contain the majority of the cancerous tissue, as shown in Figure 24. Two mass features that were determined to be influential in creating the cancerous segment were chosen for reconstructed ion heat maps and shown in the bottom of Figure 24. It can be seen in these ion heat maps that the metabolites have a relatively low abundance and are delocalized across the tissue. However, it can still be seen that these mass features have relatively similar localization patterns to the defined cancerous regions.

Representative spectra from these two cancerous regions can be found in Figure 25. These spectra are marked with some of the identified metabolite mass features from the MassTRIX database. An interesting point of the two spectra in Figure 25 is that the relative intensities are set to 20%, meaning that the viewed peaks in the spectra all have rather low intensities. This is due to the xylene wash removing the majority of the high intensity metabolites from the tissue. Due to the high resolving power of the FTICR detector, low intensity metabolites are still able to be detected above the lower limit of detection for the instrument. Also interesting is that the positive ionization spectra has a higher number of peaks and an overall greater peak intensity. As this was a preliminary experiment, a conclusive answer to this observation was not obtained. Further optimization and a greater number of replicates would possibly lead to an answer to why more peaks are detected with higher intensity in positive mode.

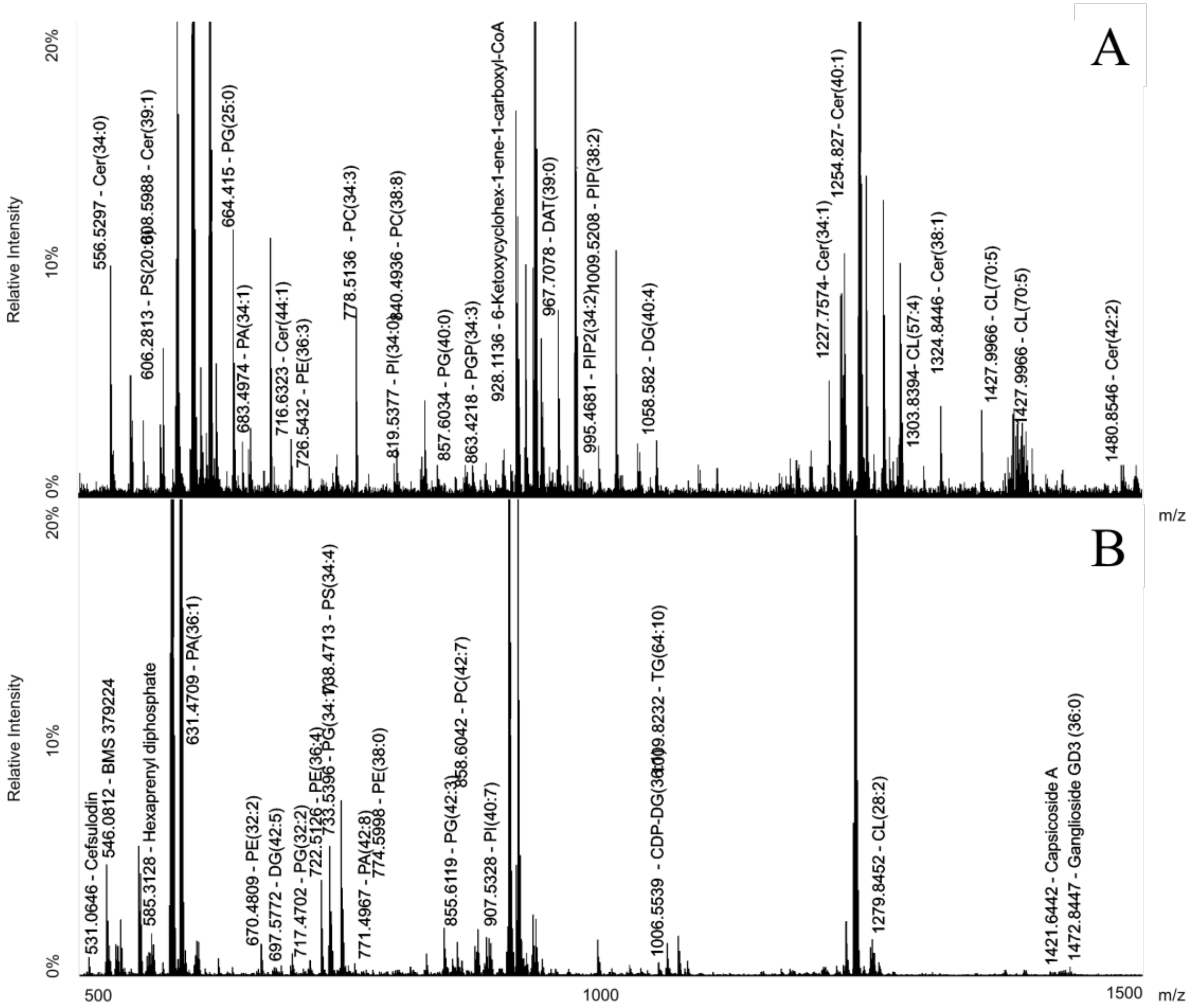

Figure 25 – Representative spectra from MALDI-MSI metabolomic dataset of (A) a colorectal liver metastasis sample analyzed with quercetin in positive ionization mode and (B) a colorectal liver metastasis sample analyzed with quercetin in negative ionization mode.

Conclusions & Future Directions

This experiment was successfully able to detect and identify metabolites from a MALDI-MSI dataset acquired from FFPE tissues. There was a general difficulty with the xylene washes, however, low abundance metabolites were still detected due to the high resolving power of the FTICR detector. This experiment was successful in detecting and identifying metabolites in both positive and negative ionization mode, as compared to the literature experiments that only contained negative ionization mode.[157,158] An aspect that was in agreement from a publication from the same laboratory was that FTICR detector was necessary for detecting low abundance and low intensity mass features from the tissue.[61]

Future experiments that would aid in understanding the metabolomic MALDI-MSI analysis of FFPE tissues could include an LC-MS/MS analysis of the xylene wash to determine which metabolite were washed away during the paraffin removal step. This could simply be done by drying down the xylene wash and reconstituting in the mobile phase then running a general LC-MS/MS metabolite analysis on the sample. It would be interesting to see which metabolites are seen in both the on-tissue MALDI-MSI data as well as the xylene wash. Another aspect that could have been added to the current experiment would be to perform an H&E stain of the tissue after the MALDI-MSI dataset was acquired. This could potentially remove some discrepancy between the H&E stained images provided and the MALDI-MSI ion heat maps. However, a pathologist would still be needed to accurately define the cancerous region on the new H&E stained image.

Once these additional steps have been added to the experiment, a more intensive and large sample size dataset would be required to determine biomarkers that are statistically relevant in determining cancer from non-cancer tissue. A minimum of 30 samples would be best for this larger scale experiment, but as always, the more samples the better. This larger sample size could potentially reveal a metabolomic pathway that is present in colorectal liver metastasis. Additionally, if the sample size was large enough and there were enough tissue sections, proteomic analyses could also be performed. This could lead to a potential meta-omic analysis that could find links between proteins and metabolites that are affected by colorectal liver metastasis. Originally a bottom-up proteomic approach was within the scope of the current experiment. This lead to the full literature search of bottom-up FFPE experiments found in Supplementary Table 3, Supplementary Table 4, and Supplementary Table 5. Unfortunately, time and the number of tissues available was a limiting factor and this aspect of the project was not completed.

Chapter 5: Conclusions & Future Directions

The three data chapters included in this thesis have an overarching theme of the optimization of sample preparation methods and data processing workflows related to MALDI-MSI. MALDI-MSI is an extremely useful technique for the multiplexed analysis of thousands of mass features. A difficult aspect of MALDI-MSI is the extremely large amounts of data that need an unbiased analysis to sift out the biologically relevant mass features. An optimized sample preparation can lead to a higher number of biologically significant mass features in the final dataset. On the other hand, a data processing workflow that is catered specifically to each dataset is also crucial for finding the biologically significant mass features. Both aspects were researched throughout this thesis. Sample preparation methods for the analysis of bottom-up proteomics in prostate cancer tissues and metabolomics in colorectal liver metastasis FFPE tissues were undertaken in Chapters Two and Four, respectively. Results of these chapters revealed mass features that were localized to the general cancerous regions of the tissues analyzed. However, conclusions from these experiments deemed it necessary to have a greater number of cancerous samples for general biomarker discovery. A workflow for data processing and statistical analysis was developed in Chapter Three. The result of the curated workflow found many different metabolites affected by thyroid hormone during metamorphosis. The research presented in this thesis was successful in exploring sample preparation methods and greatly optimizing data processing for MALDI-MSI analyses.

Bibliography

(1) Jakobs, C.; Schweitzer, S.; Dorland, B. Galactitol in Galactosemia. *Eur. J. Pediatr.* **1995**, *154* (S2), S50–S52.

(2) Bory, C.; Boulieu, R.; Chantin, C.; Mathieu, M. Diagnosis of Alcaptonuria: Rapid Analysis of Homogentisic Acid by HPLC. *Clin. Chim. Acta.* **1990**, *189* (1), 7–11.

(3) Wishart, D. S. Chapter 11 - Systems Biology Resources Arising from the Human Metabolome Project. In *Genetics Meets Metabolomics: from experiment to systems biology*; Suhre, K., Ed.; Springer New York, 2012; pp 157–176.

(4) Bell, C. Clinical Guide to Laboratory Tests. 3rd Edition. Norbert W. Tietz, Ed. *Transfusion* **2009**, *35* (11), 972–972.

(5) Wishart, D. S. Metabolomics: Applications to Food Science and Nutrition Research. *Trends Food Sci. Technol.* **2008**, *19* (9), 482–493.

(6) Mahidol, C.; Ruchirawat, S.; Prawat, H.; Pisutjaroenpong, S.; Engprasert, S.; Chumsri, P.; Tengchaisri, T.; Sirisinha, S.; Picha, P. Biodiversity and Natural Product Drug Discovery. *Pure Appl. Chem.* **1998**, *70* (11).

(7) Hamosh, A.; Scott, A. F.; Amberger, J.; Bocchini, C.; Valle, D.; McKusick, V. A. Online Mendelian Inheritance in Man (OMIM), a Knowledgebase of Human Genes and Genetic Disorders. *Nucleic Acids Res.* **2002**, *30* (1), 52–55.

(8) Chan, A. K. C.; Bruce, J. I. E.; Siriwardena, A. K. Glucose Metabolic Phenotype of Pancreatic Cancer. *World J. Gastroenterol.* **2016**, *22* (12), 3471–3485.

(9) Moreno-Sánchez, R.; Saavedra, E.; Gallardo-Pérez, J. C.; Rumjanek, F. D.; Rodríguez-Enríquez, S. Understanding the Cancer Cell Phenotype beyond the Limitations of Current Omics Analyses. *FEBS J.* **2016**, *283* (1), 54–73.

(10) Nordgren, K. K.; Skildum, A. J. The Deep End of the Metabolite Pool: Influences on Epigenetic Regulatory Mechanisms in Cancer. *Eur. J. Clin. Invest.* **2015**, *45 Suppl 1*, 9–15.

(11) Grunt, T. W. Interacting Cancer Machineries: Cell Signaling, Lipid Metabolism, and Epigenetics. *Trends Endocrinol. Metab.* **2017**.

(12) Kwon, H.; Oh, S.; Jin, X.; An, Y. J.; Park, S. Cancer Metabolomics in Basic Science Perspective. *Arch. Pharm. Res.* **2015**, *38* (3), 372–380.

(13) Liang, C.; Qin, Y.; Zhang, B.; Ji, S.; Shi, S.; Xu, W.; Liu, J.; Xiang, J.; Liang, D.; Hu, Q.; et al. Energy Sources Identify Metabolic Phenotypes in Pancreatic Cancer. *Acta Biochim. Biophys. Sin. (Shanghai).* **2016**, *48* (11), 969–979.

(14) Koriem, K. M. M. A Lipidomic Concept in Infectious Diseases. *Asian Pac. J. Trop. Biomed.* **2017**, *7* (3), 265–274.

(15) Balla, T. Phosphoinositides: Tiny Lipids with Giant Impact on Cell Regulation. *Physiol. Rev.* **2013**, *93* (3), 1019–1137.

(16) Purohit, S.; She, J.-X. Biomarkers for Type 1 Diabetes. *Int. J. Clin. Exp. Med.* **2008**, *1* (2), 98–116.

(17) Walsh, M. F.; Nathanson, K. L.; Couch, F. J.; Offit, K. Genomic Biomarkers for Breast Cancer Risk. *Adv. Exp. Med. Biol.* **2016**, *882*, 1–32.

(18) Felder, M.; Kapur, A.; Gonzalez-Bosquet, J.; Horibata, S.; Heintz, J.; Albrecht, R.; Fass, L.; Kaur, J.; Hu, K.; Shojaei, H.; et al. MUC16 (CA125): Tumor Biomarker to Cancer Therapy, a Work in Progress. *Mol. Cancer* **2014**, *13*, 129.

(19) Cui, Y.; Shu, X.-O.; Li, H.-L.; Yang, G.; Wen, W.; Gao, Y.-T.; Cai, Q.; Rothman, N.; Yin, H.-Y.; Lan, Q.; et al. Prospective Study of Urinary Prostaglandin E2 Metabolite and Pancreatic Cancer Risk. *Int. J. cancer* **2017**.

(20) Aichler, M.; Walch, A. MALDI Imaging Mass Spectrometry: Current Frontiers and Perspectives in Pathology Research and Practice. *Lab. Invest.* **2015**, *95* (4), 422–431.

(21) Han, X.; Aslanian, A.; Yates, J. R. Mass Spectrometry for Proteomics. *Curr. Opin. Chem. Biol.* **2008**, *12* (5), 483–490.

(22) Vandell, V. E.; Limbach, P. Overview of Biochemical Applications of Mass Spectrometry. In *Encyclopedia of Spectroscopy and Spectrometry*; Elsevier, 2017; pp 514–516.

(23) Parker, C. E.; Borchers, C. H. Mass Spectrometry Based Biomarker Discovery, Verification, and Validation - Quality Assurance and Control of Protein Biomarker Assays. *Mol. Oncol.* **2014**, *8* (4), 840–858.

(24) Prieto, D. A.; Johann, D. J.; Wei, B.-R.; Ye, X.; Chan, K. C.; Nissley, D. V; Simpson, R. M.; Citrin, D. E.; Mackall, C. L.; Linehan, W. M.; et al. Mass Spectrometry in Cancer Biomarker Research: A Case for Immunodepletion of Abundant Blood-Derived Proteins from Clinical Tissue Specimens. *Biomark. Med.* **2014**, *8* (2), 269–286.

(25) Crutchfield, C. A.; Thomas, S. N.; Sokoll, L. J.; Chan, D. W. Advances in Mass Spectrometry-Based Clinical Biomarker Discovery. *Clin. Proteomics* **2016**, *13* (1), 1.

(26) Lu, M.; Faull, K. F.; Whitelegge, J. P.; He, J.; Shen, D.; Saxton, R. E.; Chang, H. R. Proteomics and Mass Spectrometry for Cancer Biomarker Discovery. *Biomark. Insights* **2007**, *2*, 347–360.

(27) Melnik, A. V; da Silva, R. R.; Hyde, E. R.; Aksenov, A. A.; Vargas, F.; Bouslimani, A.; Protsyuk, I.; Jarmusch, A. K.; Tripathi, A.; Alexandrov, T.; et al. Coupling Targeted and Untargeted Mass Spectrometry for Metabolome-Microbiome-Wide Association Studies of Human Fecal Samples. *Anal. Chem.* **2017**, *89* (14), 7549–7559.

(28) Wu, A. H. B.; Colby, J. High-Resolution Mass Spectrometry for Untargeted Drug Screening. *Methods Mol. Biol.* **2016**, *1383*, 153–166.

(29) Aebersold, R.; Mann, M. Mass Spectrometry-Based Proteomics. *Nature* **2003**, *422* (6928), 198–207.

(30) Karas, M.; Hillenkamp, F. Laser Desorption Ionization of Proteins with Molecular Masses Exceeding 10,000 Daltons. *Anal. Chem.* **1988**, *60* (20), 2299–2301.

(31) Clark, A. E.; Kaleta, E. J.; Arora, A.; Wolk, D. M. Matrix-Assisted Laser Desorption Ionization-Time of Flight Mass Spectrometry: A Fundamental Shift in the Routine Practice of Clinical Microbiology. *Clin. Microbiol. Rev.* **2013**, *26* (3), 547–603.

(32) Caprioli, R. M.; Farmer, T. B.; Gile, J. Molecular Imaging of Biological Samples: Localization of Peptides and Proteins Using MALDI-TOF MS. *Anal. Chem.* **1997**, *69* (23), 4751–4760.

(33) Casadonte, R.; Caprioli, R. M. Proteomic Analysis of Formalin-Fixed Paraffin-Embedded Tissue by MALDI Imaging Mass Spectrometry. *Nat. Protoc.* **2011**, *6* (11), 1695–1709.

(34) Deininger, S.-O.; Cornett, D. S.; Paape, R.; Becker, M.; Pineau, C.; Rauser, S.; Walch, A.; Wolski, E. Normalization in MALDI-TOF Imaging Datasets of Proteins: Practical Considerations. *Anal. Bioanal. Chem.* **2011**, *401* (1), 167–181.

(35) Flatley, B.; Malone, P.; Cramer, R. MALDI Mass Spectrometry in Prostate Cancer Biomarker Discovery. *Biochim. Biophys. Acta* **2014**, *1844* (5), 940–949.

(36) Baker, T. C.; Han, J.; Borchers, C. H. Recent Advancements in Matrix-Assisted Laser Desorption/ionization Mass Spectrometry Imaging. *Curr. Opin. Biotechnol.* **2016**, *43*, 62–69.

(37) Wang, X.; Han, J.; Chou, A.; Yang, J.; Pan, J.; Borchers, C. H. Hydroxyflavones as a New Family of Matrices for MALDI Tissue Imaging. *Anal. Chem.* **2013**, *85* (15), 7566–7573.

(38) Wang, X.; Han, J.; Yang, J.; Pan, J.; Borchers, C. H. Matrix Coating Assisted by an Electric Field (MCAEF) for Enhanced Tissue Imaging by MALDI-MS. *Chem. Sci.* **2015**, *6* (1), 729–738.

(39) Wang, X.; Han, J.; Hardie, D. B.; Yang, J.; Pan, J.; Borchers, C. H. Metabolomic Profiling of Prostate Cancer by Matrix Assisted Laser Desorption/ionization-Fourier Transform Ion Cyclotron Resonance Mass Spectrometry Imaging Using Matrix Coating Assisted by an Electric Field (MCAEF). *Biochim. Biophys. Acta* **2017**, *1865* (7), 755–767.

(40) Wang, X.; Han, J.; Pan, J.; Borchers, C. H. Comprehensive Imaging of Porcine Adrenal Gland Lipids by MALDI-FTMS Using Quercetin as a Matrix. *Anal. Chem.* **2014**, *86* (1), 638–646.

(41) Thomas, A.; Charbonneau, J. L.; Fournaise, E.; Chaurand, P. Sublimation of New Matrix Candidates for High Spatial Resolution Imaging Mass Spectrometry of Lipids: Enhanced Information in Both Positive and Negative Polarities after 1,5-Diaminonapthalene Deposition. *Anal. Chem.* **2012**, *84* (4), 2048–2054.

(42) Francese, S.; Bradshaw, R.; Flinders, B.; Mitchell, C.; Bleay, S.; Cicero, L.; Clench, M. R. Curcumin: A Multipurpose Matrix for MALDI Mass Spectrometry Imaging Applications. *Anal. Chem.* **2013**, *85* (10), 5240–5248.

(43) Ye, H.; Gemperline, E.; Venkateshwaran, M.; Chen, R.; Delaux, P.-M.; Howes-Podoll, M.; Ané, J.-M.; Li, L. MALDI Mass Spectrometry-Assisted Molecular Imaging of Metabolites during Nitrogen Fixation in the Medicago Truncatula-Sinorhizobium Meliloti Symbiosis. *Plant J.* **2013**, *75* (1), 130–145.

(44) Calvano, C. D.; Monopoli, A.; Ditaranto, N.; Palmisano, F. 1,8-bis(dimethylamino)naphthalene/9-Aminoacridine: A New Binary Matrix for Lipid Fingerprinting of Intact Bacteria by Matrix Assisted Laser Desorption Ionization Mass Spectrometry. *Anal. Chim. Acta* **2013**, *798*, 56–63.

(45) Shanta, S. R.; Kim, T. Y.; Hong, J. H.; Lee, J. H.; Shin, C. Y.; Kim, K. P. K.-H.; Kim, Y. H.; Kim, S. K.; Kim, K. P. K.-H. A New Combination MALDI Matrix for Small Molecule Analysis: Application to Imaging Mass Spectrometry for Drugs and Metabolites. *Analyst* **2012**, *137* (24), 5757–5762.

(46) Fülöp, A.; Porada, M. B.; Marsching, C.; Blott, H.; Meyer, B.; Tambe, S.; Sandhoff, R.; Junker, H.-D.; Hopf, C. 4-Phenyl-α-Cyanocinnamic Acid Amide: Screening for a Negative Ion Matrix for MALDI-MS Imaging of Multiple Lipid Classes. *Anal. Chem.* **2013**, *85* (19), 9156–9163.

(47) Kim, Y.-K.; Na, H.-K.; Kwack, S.-J.; Ryoo, S.-R.; Lee, Y.; Hong, S.; Hong, S.; Jeong, Y.; Min, D.-H. Synergistic Effect of Graphene oxide/MWCNT Films in Laser Desorption/ionization Mass Spectrometry of Small Molecules and Tissue Imaging. *ACS Nano* **2011**, *5* (6), 4550–4561.

(48) Kim, Y.; Min, D. Fabrication of Alternating Multilayer Films of Graphene Oxide and Carbon Nanotube and Its Application in Mechanistic Study of Laser Desorption/ionization of Small Molecules. *ACS Appl. Mater. Interfaces* **2012**, *4* (4), 2088–2095.

(49) Le, C. H.; Han, J.; Borchers, C. H. Dithranol as a MALDI Matrix for Tissue Imaging of Lipids by Fourier Transform Ion Cyclotron Resonance Mass Spectrometry. *Anal. Chem.* **2012**, *84* (19), 8391–8398.

(50) Le, C. H.; Han, J.; Borchers, C. H. Dithranol as a Matrix for Matrix Assisted Laser Desorption/ionization Imaging on a Fourier Transform Ion Cyclotron Resonance Mass Spectrometer. *J. Vis. Exp.* **2013**, No. 81, e50733.

(51) Friesen, W. L.; Schultz, B. J.; Destino, J. F.; Alivio, T. E. G.; Steet, J. R.; Banerjee, S.; Wood, T. D. Two-Dimensional Graphene as a Matrix for MALDI Imaging Mass Spectrometry. *J. Am. Soc. Mass Spectrom.* **2015**, *26* (11), 1963–1966.

(52) Nazari, M.; Bokhart, M. T.; Muddiman, D. C. Whole-Body Mass Spectrometry Imaging by Infrared Matrix-Assisted Laser Desorption Electrospray Ionization (IR-MALDESI). *J. Vis. Exp.* **2016**, No. 109, e53942.

(53) Hankin, J. A.; Barkley, R. M.; Murphy, R. C. Sublimation as a Method of Matrix Application for Mass Spectrometric Imaging. *J. Am. Soc. Mass Spectrom.* **2007**, *18* (9), 1646–1652.

(54) Yang, J.; Caprioli, R. M. Matrix Sublimation/recrystallization for Imaging Proteins by Mass Spectrometry at High Spatial Resolution. *Anal. Chem.* **2011**, *83* (14), 5728–5734.

(55) Gemperline, E.; Rawson, S.; Li, L. Optimization and Comparison of Multiple MALDI Matrix Application Methods for Small Molecule Mass Spectrometric Imaging. *Anal. Chem.* **2014**, *86* (20), 10030–10035.

(56) Grove, K. J.; Frappier, S. L.; Caprioli, R. M. Matrix Pre-Coated MALDI MS Targets for Small Molecule Imaging in Tissues. *J. Am. Soc. Mass Spectrom.* **2011**, *22* (1), 192–195.

(57) Yang, J.; Caprioli, R. M. Matrix Pre-Coated Targets for High Throughput MALDI Imaging of Proteins. *J. Mass Spectrom.* **2014**, *49* (5), 417–422.

(58) Wang, X.; Han, J.; Hardie, D. B.; Yang, J.; Borchers, C. H. The Use of Matrix Coating Assisted by an Electric Field (MCAEF) to Enhance Mass Spectrometric Imaging of Human Prostate Cancer Biomarkers. *J. Mass Spectrom.* **2016**, *51* (1), 86–95.

(59) Loo, J. A. The Tools of Proteomics. *Adv. Protein Chem.* **2003**, *65*, 25–56.

(60) Stewart, D.; Dhungana, S.; Clark, R.; Pathmasiri, W.; McRitchie, S.; Sumner, S. Omics Technologies Used in Systems Biology. In *Systems Biology in Toxicology and Environmental Health*; Elsevier, 2015; pp 57–83.

(61) Buck, A.; Balluff, B.; Voss, A.; Langer, R.; Zitzelsberger, H.; Aichler, M.; Walch, A. How Suitable Is Matrix-Assisted Laser Desorption/Ionization-Time-of-Flight for Metabolite Imaging from Clinical Formalin-Fixed and Paraffin-Embedded Tissue Samples in Comparison to Matrix-Assisted Laser Desorption/Ionization-Fourier Transform Ion Cyclotro. *Anal. Chem.* **2016**, *88* (10), 5281–5289.

(62) Dilillo, M.; Ait-Belkacem, R.; Esteve, C.; Pellegrini, D.; Nicolardi, S.; Costa, M.; Vannini, E.; Graaf, E. L. de; Caleo, M.; McDonnell, L. A. Ultra-High Mass Resolution MALDI Imaging Mass Spectrometry of Proteins and Metabolites in a Mouse Model of Glioblastoma. *Sci. Rep.* **2017**, *7* (1), 603.

(63) Kriegsmann, J.; Kriegsmann, M.; Casadonte, R. MALDI TOF Imaging Mass

Spectrometry in Clinical Pathology: A Valuable Tool for Cancer Diagnostics (Review). *Int. J. Oncol.* **2015**, *46* (3), 893–906.

(64) Https://ms-Imaging.org/wp/mmsit/.

(65) Clerens, S.; Ceuppens, R.; Arckens, L. CreateTarget and Analyze This!: New Software Assisting Imaging Mass Spectrometry on Bruker Reflex IV and Ultraflex II Instruments. *Rapid Commun. Mass Spectrom.* **2006**, *20* (20), 3061–3066.

(66) Https://ms-imaging.org/wp/4000-Series-Imaging/.

(67) Bruand, J.; Alexandrov, T.; Sistla, S.; Wisztorski, M.; Meriaux, C.; Becker, M.; Salzet, M.; Fournier, I.; Macagno, E.; Bafna, V. AMASS: Algorithm for MSI Analysis by Semi-Supervised Segmentation. *J. Proteome Res.* **2011**, *10* (10), 4734–4743.

(68) Https://ms-Imaging.org/wp/biomap/.

(69) Https://amolf.nl/download/datacubeexplorer.

(70) Wijetunge, C. D.; Saeed, I.; Boughton, B. A.; Spraggins, J. M.; Caprioli, R. M.; Bacic, A.; Roessner, U.; Halgamuge, S. K. EXIMS: An Improved Data Analysis Pipeline Based on a New Peak Picking Method for EXploring Imaging Mass Spectrometry Data. *Bioinformatics* **2015**, *31* (19), 3198–3206.

(71) Källback, P.; Nilsson, A.; Shariatgorji, M.; Andrén, P. E. msIQuant - Quantitation Software for Mass Spectrometry Imaging Enabling Fast Access, Visualization, and Analysis of Large Data Sets. *Anal. Chem.* **2016**, *88* (8), 4346–4353.

(72) Https://ms-Imaging.org/wp/imzml/software-Tools/cea-Spect-Viewer/.

(73) Https://ms-Imaging.org/wp/mitsutoshi-Setou/.

(74) Https://ms-Imaging.org/wp/imzml/software-Tools/raw-to-Imzml-Converter/.

(75) Bemis, K. D.; Harry, A.; Eberlin, L. S.; Ferreira, C.; van de Ven, S. M.; Mallick, P.; Stolowitz, M.; Vitek, O. Cardinal: An R Package for Statistical Analysis of Mass Spectrometry-Based Imaging Experiments. *Bioinformatics* **2015**, *31* (14), 2418–2420.

(76) Gibb, S.; Strimmer, K. MALDIquant: A Versatile R Package for the Analysis of

Mass Spectrometry Data. *Bioinformatics* **2012**, *28* (17), 2270–2271.

(77) Https://www.imabiotech.com/multimaging-Cloud/.

(78) Parry, R. M.; Galhena, A. S.; Gamage, C. M.; Bennett, R. V.; Wang, M. D.; Fernández, F. M. omniSpect: An Open MATLAB-Based Tool for Visualization and Analysis of Matrix-Assisted Laser Desorption/ionization and Desorption Electrospray Ionization Mass Spectrometry Images. *J. Am. Soc. Mass Spectrom.* **2013**, *24* (4), 646–649.

(79) Rübel, O.; Greiner, A.; Cholia, S.; Louie, K.; Bethel, E. W.; Northen, T. R.; Bowen, B. P. OpenMSI: A High-Performance Web-Based Platform for Mass Spectrometry Imaging. *Anal. Chem.* **2013**, *85* (21), 10354–10361.

(80) Klein, O.; Strohschein, K.; Nebrich, G.; Oetjen, J.; Trede, D.; Thiele, H.; Alexandrov, T.; Giavalisco, P.; Duda, G. N.; von Roth, P.; et al. MALDI Imaging Mass Spectrometry: Discrimination of Pathophysiological Regions in Traumatized Skeletal Muscle by Characteristic Peptide Signatures. *Proteomics* **2014**, *14* (20), 2249–2260.

(81) Palagi, P. M.; Walther, D.; Quadroni, M.; Catherinet, S.; Burgess, J.; Zimmermann-Ivol, C. G.; Sanchez, J.-C.; Binz, P.-A.; Hochstrasser, D. F.; Appel, R. D. MSight: An Image Analysis Software for Liquid Chromatography-Mass Spectrometry. *Proteomics* **2005**, *5* (9), 2381–2384.

(82) Strohalm, M.; Kavan, D.; Novák, P.; Volný, M.; Havlícek, V. mMass 3: A Cross-Platform Software Environment for Precise Analysis of Mass Spectrometric Data. *Anal. Chem.* **2010**, *82* (11), 4648–4651.

(83) Robichaud, G.; Garrard, K. P.; Barry, J. A.; Muddiman, D. C. MSiReader: An Open-Source Interface to View and Analyze High Resolving Power MS Imaging Files on Matlab Platform. *J. Am. Soc. Mass Spectrom.* **2013**, *24* (5), 718–721.

(84) Https://www.bruker.com/products/mass-Spectrometry-and-Separations/ms-Software/fleximaging/overview.html.

(85) https://www.thermofisher.com/order/catalog/product/10137985.

(86) Http://www.premierbiosoft.com/maldi-Tissue-Imaging/index.html.

(87) Jardin-Mathé, O.; Bonnel, D.; Franck, J.; Wisztorski, M.; Macagno, E.; Fournier,

I.; Salzet, M. MITICS (MALDI Imaging Team Imaging Computing System): A New Open Source Mass Spectrometry Imaging Software. *J. Proteomics* **2008**, *71* (3), 332–345.

(88) Gamboa-Becerra, R.; Ramírez-Chávez, E.; Molina-Torres, J.; Winkler, R. MSI.R Scripts Reveal Volatile and Semi-Volatile Features in Low-Temperature Plasma Mass Spectrometry Imaging (LTP-MSI) of Chilli (Capsicum Annuum). *Anal. Bioanal. Chem.* **2015**, *407* (19), 5673–5684.

(89) Https://ms-imaging.org/wp/2008/03/18/tissueview-10/.

(90) Https://ms-Imaging.org/wp/msimageview/.

(91) Durbin, K. R.; Fornelli, L.; Fellers, R. T.; Doubleday, P. F.; Narita, M.; Kelleher, N. L. Quantitation and Identification of Thousands of Human Proteoforms below 30 kDa. *J. Proteome Res.* **2016**, *15* (3), 976–982.

(92) Kelleher, N. L. Top-down Proteomics. *Anal. Chem.* **2004**, *76* (11), 197A–203A.

(93) Zhang, Y.; Fonslow, B. R.; Shan, B.; Baek, M.-C.; Yates, J. R. Protein Analysis by Shotgun/Bottom-up Proteomics. *Chem. Rev.* **2013**, *113* (4), 2343–2394.

(94) Tran, J. C.; Zamdborg, L.; Ahlf, D. R.; Lee, J. E.; Catherman, A. D.; Durbin, K. R.; Tipton, J. D.; Vellaichamy, A.; Kellie, J. F.; Li, M.; et al. Mapping Intact Protein Isoforms in Discovery Mode Using Top-down Proteomics. *Nature* **2011**, *480* (7376), 254–258.

(95) Olsen, J. V.; Ong, S.-E.; Mann, M. Trypsin Cleaves Exclusively C-Terminal to Arginine and Lysine Residues. *Mol. Cell. Proteomics* **2004**, *3* (6), 608–614.

(96) Groseclose, M. R.; Andersson, M.; Hardesty, W. M.; Caprioli, R. M. Identification of Proteins Directly from Tissue: In Situ Tryptic Digestions Coupled with Imaging Mass Spectrometry. *J. Mass Spectrom.* **2007**, *42* (2), 254–262.

(97) Deininger, L.; Patel, E.; Clench, M. R.; Sears, V.; Sammon, C.; Francese, S. Proteomics Goes Forensic: Detection and Mapping of Blood Signatures in Fingermarks. *Proteomics* **2016**, *16* (11–12), 1707–1717.

(98) Llombart, V.; Trejo, S. A.; Bronsoms, S.; Morancho, A.; Feifei, M.; Faura, J.; García-Berrocoso, T.; Simats, A.; Rosell, A.; Canals, F.; et al. Profiling and Identification of New Proteins Involved in Brain Ischemia Using MALDI-

Imaging-Mass-Spectrometry. *J. Proteomics* **2017**, *152*, 243–253.

(99) El Ayed, M.; Bonnel, D.; Longuespée, R.; Castelier, C.; Franck, J.; Vergara, D.; Desmons, A.; Tasiemski, A.; Kenani, A.; Vinatier, D.; et al. MALDI Imaging Mass Spectrometry in Ovarian Cancer for Tracking, Identifying, and Validating Biomarkers. *Med. Sci. Monit.* **2010**, *16* (8), BR233-45.

(100) Stoeckli, M.; Staab, D.; Schweitzer, A. Compound and Metabolite Distribution Measured by MALDI Mass Spectrometric Imaging in Whole-Body Tissue Sections. *Int. J. Mass Spectrom.* **2007**, *260* (2–3), 195–202.

(101) Lee, W. N. P. Characterizing Phenotype with Tracer Based Metabolomics. *Metabolomics* **2006**, *2* (1), 31–39.

(102) Carter, C. L.; Jones, J. W.; Farese, A. M.; MacVittie, T. J.; Kane, M. A. Inflation-Fixation Method for Lipidomic Mapping of Lung Biopsies by Matrix Assisted Laser Desorption/Ionization-Mass Spectrometry Imaging. *Anal. Chem.* **2016**, *88* (9), 4788–4794.

(103) Korte, A. R.; Yandeau-Nelson, M. D.; Nikolau, B. J.; Lee, Y. J. Subcellular-Level Resolution MALDI-MS Imaging of Maize Leaf Metabolites by MALDI-Linear Ion Trap-Orbitrap Mass Spectrometer. *Anal. Bioanal. Chem.* **2015**, *407* (8), 2301–2309.

(104) Buck, A.; Aichler, M.; Huber, K.; Walch, A. In Situ Metabolomics in Cancer by Mass Spectrometry Imaging. *Adv. Cancer Res.* **2017**, *134*, 117–132.

(105) Lou, S.; Balluff, B.; Cleven, A. H. G.; Bovée, J. V. M. G.; McDonnell, L. A. Prognostic Metabolite Biomarkers for Soft Tissue Sarcomas Discovered by Mass Spectrometry Imaging. *J. Am. Soc. Mass Spectrom.* **2017**, *28* (2), 376–383.

(106) Wu, S.; Lourette, N. M.; Tolić, N.; Zhao, R.; Robinson, E. W.; Tolmachev, A. V; Smith, R. D.; Pasa-Tolić, L. An Integrated Top-down and Bottom-up Strategy for Broadly Characterizing Protein Isoforms and Modifications. *J. Proteome Res.* **2009**, *8* (3), 1347–1357.

(107) Canadian Cancer Statistics 2017. Canadian Cancer Society's Advisory Committee on Cancer Statistics. Toronto, ON: Canadian Cancer Society; 2017. Available at: cancer.ca/Canadian-Cancer- Statistics-2017-EN.pdf.

(108) Morgan, T.; Palapattu, G.; Wei, J. Screening for Prostate Cancer-Beyond Total PSA, Utilization of Novel Biomarkers. *Curr. Urol. Rep.* **2015**, *16* (9), 63.

(109) Catalona, W. J.; Smith, D. S.; Ratliff, T. L.; Dodds, K. M.; Coplen, D. E.; Yuan, J. J. J.; Petros, J. A.; Andriole, G. L. Measurement of Prostate-Specific Antigen in Serum as a Screening Test for Prostate Cancer. *N. Engl. J. Med.* **1991**, *324* (17), 1156–1161.

(110) Loeb, S.; Bjurlin, M. A.; Nicholson, J.; Tammela, T. L.; Penson, D. F.; Carter, H. B.; Carroll, P.; Etzioni, R. Overdiagnosis and Overtreatment of Prostate Cancer. *Eur. Urol.* **2014**, *65* (6), 1046–1055.

(111) Care, C. T. F. on P. H. Recommendations on Screening for Prostate Cancer with the Prostate-Specific Antigen Test. *CMAJ* **2014**, *186* (16), 1201–1202.

(112) Han, J.; Danell, R. M.; Patel, J. R.; Gumerov, D. R.; Scarlett, C. O.; Speir, J. P.; Parker, C. E.; Rusyn, I.; Zeisel, S.; Borchers, C. H. Towards High-Throughput Metabolomics Using Ultrahigh-Field Fourier Transform Ion Cyclotron Resonance Mass Spectrometry. *Metabolomics* **2008**, *4* (2), 128–140.

(113) Xia, J.; Sinelnikov, I. V; Han, B.; Wishart, D. S. MetaboAnalyst 3.0--Making Metabolomics More Meaningful. *Nucleic Acids Res.* **2015**, *43* (W1), W251-7.

(114) R Core Team. *R: A Language and Environment for Statistical Computing*; R Foundation for Statistical Computing: Vienna, Austria, 2016.

(115) RStudio Team. *RStudio: Integrated Development for R.*; RStudio Inc.: Boston, MA, 2015.

(116) Shevchenko, G.; Musunuri, S.; Wetterhall, M.; Bergquist, J. Comparison of Extraction Methods for the Comprehensive Analysis of Mouse Brain Proteome Using Shotgun-Based Mass Spectrometry. *J. Proteome Res.* **2012**, *11* (4), 2441–2451.

(117) Harris, G. a.; Nicklay, J. J.; Caprioli, R. M. Localized in Situ Hydrogel-Mediated Protein Digestion and Extraction Technique for on-Tissue Analysis. *Anal. Chem.* **2013**, *85* (5), 2717–2723.

(118) Gilbert; Tata; Atkinson. *Metamorphosis: Postembryonic Reprogramming of Gene Expression in Amphibian and Insect Cells*; Academic Press, San Diegogilbert, 1996.

(119) Shi, Y.-B. *Amphibian Metamorphosis: From Morphology to Molecular Biology*; Wiley-Lissshi, New York, 2000.

(120) Dodd, M. H. I.; Dodd, J. M. *The Biology of Metamorphosis*, Vol 3.; Lofts, B., Ed.; Elsevier: New York, NY, 1976.

(121) Mullur, R.; Liu, Y.-Y.; Brent, G. A. Thyroid Hormone Regulation of Metabolism. *Physiol. Rev.* **2014**, *94* (2), 355–382.

(122) Ichu, T.-A.; Han, J.; Borchers, C. H.; Lesperance, M.; Helbing, C. C. Metabolomic Insights into System-Wide Coordination of Vertebrate Metamorphosis. *BMC Dev. Biol.* **2014**, *14* (1), 5.

(123) Suzuki, S.; Awai, K.; Ishihara, A.; Yamauchi, K. Cold Temperature Blocks Thyroid Hormone-Induced Changes in Lipid and Energy Metabolism in the Liver of Lithobates Catesbeianus Tadpoles. *Cell Biosci.* **2016**, *6*, 19.

(124) Rohner, T. C.; Staab, D.; Stoeckli, M. MALDI Mass Spectrometric Imaging of Biological Tissue Sections. *Mech. Ageing Dev.* **2005**, *126* (1), 177–185.

(125) Khatib-Shahidi, S.; Andersson, M.; Herman, J. L.; Gillespie, T. A.; Caprioli, R. M. Direct Molecular Analysis of Whole-Body Animal Tissue Sections by Imaging MALDI Mass Spectrometry. *Anal. Chem.* **2006**, *78* (18), 6448–6456.

(126) Reyzer, M. L.; Caprioli, R. M. MALDI-MS-Based Imaging of Small Molecules and Proteins in Tissues. *Curr. Opin. Chem. Biol.* **2007**, *11* (1), 29–35.

(127) Reyzer, M. L.; Chaurand, P.; Angel, P. M.; Caprioli, R. M. Direct Molecular Analysis of Whole-Body Animal Tissue Sections by MALDI Imaging Mass Spectrometry. *Methods Mol. Biol.* **2010**, *656* (18), 285–301.

(128) Takai, N.; Tanaka, Y.; Inazawa, K.; Saji, H. Quantitative Analysis of Pharmaceutical Drug Distribution in Multiple Organs by Imaging Mass Spectrometry. *Rapid Commun. Mass Spectrom.* **2012**, *26* (13), 1549–1556.

(129) Nelson, K. A.; Daniels, G. J.; Fournie, J. W.; Hemmer, M. J. Optimization of Whole-Body Zebrafish Sectioning Methods for Mass Spectrometry Imaging. *J. Biomol. Tech.* **2013**, *24* (3).

(130) Taylor, A.; Kollros, J. Stages in the Normal Development of Rana Pipiens Larvae. *Anat. Rec.* **1946**, *94*, 7–13.

(131) Suhre, K.; Schmitt-Kopplin, P. MassTRIX: Mass Translator into Pathways. *Nucleic Acids Res.* **2008**, *36* (Web Server issue), W481-4.

(132) Wägele, B.; Witting, M.; Schmitt-Kopplin, P.; Suhre, K. MassTRIX Reloaded: Combined Analysis and Visualization of Transcriptome and Metabolome Data. *PLoS One* **2012**, *7* (7), e39860.

(133) Maceyka, M.; Milstien, S.; Spiegel, S. Sphingosine-1-Phosphate: The Swiss Army Knife of Sphingolipid Signaling. *J. Lipid Res.* **2009**, *50 Suppl*, S272-6.

(134) Wang, Z.; Brown, D. D. Thyroid Hormone-Induced Gene Expression Program for Amphibian Tail Resorption. *J. Biol. Chem.* **1993**, *268* (22), 16270–16278.

(135) Skirrow, R. C.; Veldhoen, N.; Domanski, D.; Helbing, C. C. Roscovitine Inhibits Thyroid Hormone-Induced Tail Regression of the Frog Tadpole and Reveals a Role for Cyclin C/Cdk8 in the Establishment of the Metamorphic Gene Expression Program. *Dev. Dyn.* **2008**, *237* (12), 3787–3797.

(136) Helbing, C. C.; Atkinson, B. G. 3,5,3'-Triiodothyronine-Induced Carbamyl-Phosphate Synthetase Gene Expression Is Stabilized in the Liver of Rana Catesbeiana Tadpoles during Heat Shock. *J. Biol. Chem.* **1994**, *269* (16), 11743–11750.

(137) Hammond, S. A.; Veldhoen, N.; Helbing, C. C. Influence of Temperature on Thyroid Hormone Signaling and Endocrine Disruptor Action in Rana (Lithobates) Catesbeiana Tadpoles. *Gen. Comp. Endocrinol.* **2015**, *219*, 6–15.

(138) Danos, M. C.; Yost, H. J. Linkage of Cardiac Left-Right Asymmetry and Dorsal-Anterior Development in Xenopus. *Development* **1995**, *121* (5), 1467–1474.

(139) Stemple, D. L. Structure and Function of the Notochord: An Essential Organ for Chordate Development. *Development* **2005**, *132* (11), 2503–2512.

(140) Fleming, A.; Keynes, R. J.; Tannahill, D. The Role of the Notochord in Vertebral Column Formation. *J. Anat.* **2001**, *199*, 177–180.

(141) Obeid, L. M.; Linardic, C. M.; Karolak, L. A.; Hannun, Y. A. Programmed Cell Death Induced by Ceramide. *Science* **1993**, *259* (5102), 1769–1771.

(142) Zhou, H.; Summers, S. A.; Birnbaum, M. J.; Pittman, R. N. Inhibition of Akt Kinase by Cell-Permeable Ceramide and Its Implications for Ceramide-Induced Apoptosis. *J. Biol. Chem.* **1998**, *273* (26), 16568–16575.

(143) Frieden, E. Biochemical Adaptation and Anuran Metamorphosis. *Am. Zool.* **1961**,

1, 115–149.

(144) Cohen, P. P. Biochemical Aspects of Metamorphosis: Transition from Ammonotelism to Ureotelism. *Harvey Lect.* **1966**, *60*, 119–154.

(145) Partovi, S. H.; Miliano, R.; Roberts, B.; Veldhoen, N.; Lesperance, M.; Pyle, G.; van Aggelen, G.; Helbing, C. C. Transcriptomic Analysis of Rana (Lithobates) Catesbeiana Tadpole Tail Fin and Liver Tissues Following Exposure to Thyroid Hormones and Estrogen. *Submitted*.

(146) Okazaki, T.; Watanabe, E.; Suzuki, S.; Shukuya, R. Heme Oxygenase Activity in Liver Microsomes of the Bullfrog, Rana Catesbeiana, and Its Change during the Tadpole Development. *Comp. Biochem. Physiol. B.* **1983**, *74* (3), 533–537.

(147) Hannun, Y. A.; Obeid, L. M. Principles of Bioactive Lipid Signalling: Lessons from Sphingolipids. *Nat. Rev. Mol. Cell Biol.* **2008**, *9* (2), 139–150.

(148) Hetzel, B. S.; Mano, M. T. A Review of Experimental Studies of Iodine Deficiency during Fetal Development. *J. Nutr.* **1989**, *119* (2), 145–151.

(149) Bernal, J. *Thyroid Hormones in Brain Development and Function*; De Groot, L., Chrousos, G., Dungan, K., Eds.; Endotext[Internet]: South Dartmouth (MA), 2015.

(150) Statistics Canada. Canadian Cancer Statistics 2016 Special Topic: HPV-Associated Cancers. **2016**, 1–132.

(151) Canadian Cancer Society's Advisory Committee on Cancer Statistics. *Canadian Cancer Statistics 2015*. Canadian Cancer Society: Toronto, ON 2015, p 2015.

(152) Lech, G.; Słotwiński, R.; Słodkowski, M.; Krasnodębski, I. W. Colorectal Cancer Tumour Markers and Biomarkers: Recent Therapeutic Advances. *World J. Gastroenterol.* **2016**, *22* (5), 1745–1755.

(153) Noecker, C.; McNally, C. P.; Eng, A.; Borenstein, E. High-Resolution Characterization of the Human Microbiome. *Transl. Res.* **2017**, *179*, 7–23.

(154) Kunkel, G. R.; Mehrabian, M.; Martinson, H. G. Contact-Site Cross-Linking Agents. *Mol. Cell. Biochem.* **1981**, *34* (1), 3–13.

(155) Prieto, D. A.; Hood, B. L.; Darfler, M. M.; Guiel, T. G.; Lucas, D. A.; Conrads, T. P.; Veenstra, T. D.; Krizman, D. B. Liquid Tissue: Proteomic Profiling of

Formalin-Fixed Tissues. *Biotechniques* **2005**, *Suppl*, 32–35.

(156) Ronci, M.; Bonanno, E.; Colantoni, A.; Pieroni, L.; Di Ilio, C.; Spagnoli, L. G.; Federici, G.; Urbani, A. Protein Unlocking Procedures of Formalin-Fixed Paraffin-Embedded Tissues: Application to MALDI-TOF Imaging MS Investigations. *Proteomics* **2008**, *8* (18), 3702–3714.

(157) Buck, A.; Ly, A.; Balluff, B.; Sun, N.; Gorzolka, K.; Feuchtinger, A.; Janssen, K.-P.; Kuppen, P. J. K.; van de Velde, C. J. H.; Weirich, G.; et al. High-Resolution MALDI-FT-ICR MS Imaging for the Analysis of Metabolites from Formalin-Fixed, Paraffin-Embedded Clinical Tissue Samples. *J. Pathol.* **2015**, *237* (1), 123–132.

(158) Ly, A.; Buck, A.; Balluff, B.; Sun, N.; Gorzolka, K.; Feuchtinger, A.; Janssen, K.-P.; Kuppen, P. J. K.; van de Velde, C. J. H.; Weirich, G.; et al. High-Mass-Resolution MALDI Mass Spectrometry Imaging of Metabolites from Formalin-Fixed Paraffin-Embedded Tissue. *Nat. Protoc.* **2016**, *11* (8), 1428–1443.

(159) Cole, L. M.; Mahmoud, K.; Haywood-Small, S.; Tozer, G. M.; Smith, D. P.; Clench, M. R. Recombinant " IMS TAG" proteins--a New Method for Validating Bottom-up Matrix-Assisted Laser Desorption/ionisation Ion Mobility Separation Mass Spectrometry Imaging. *Rapid Commun. Mass Spectrom.* **2013**, *27* (21), 2355–2362.

(160) Diehl, H. C.; Beine, B.; Elm, J.; Trede, D.; Ahrens, M.; Eisenacher, M.; Marcus, K.; Meyer, H. E.; Henkel, C. The Challenge of on-Tissue Digestion for MALDI MSI- a Comparison of Different Protocols to Improve Imaging Experiments. *Anal. Bioanal. Chem.* **2015**, *407* (8), 2223–2243.

(161) Djidja, M.-C.; Francese, S.; Loadman, P. M.; Sutton, C. W.; Scriven, P.; Claude, E.; Snel, M. F.; Franck, J.; Salzet, M.; Clench, M. R. Detergent Addition to Tryptic Digests and Ion Mobility Separation prior to MS/MS Improves Peptide Yield and Protein Identification for in Situ Proteomic Investigation of Frozen and Formalin-Fixed Paraffin-Embedded Adenocarcinoma Tissue Sections. *Proteomics* **2009**, *9* (10), 2750–2763.

(162) Franck, J.; Arafah, K.; Barnes, A.; Wisztorski, M.; Salzet, M.; Fournier, I. Improving Tissue Preparation for Matrix-Assisted Laser Desorption Ionization Mass Spectrometry Imaging. Part 1: Using Microspotting. *Anal. Chem.* **2009**, *81* (19), 8193–8202.

(163) Quanico, J.; Franck, J.; Dauly, C.; Strupat, K.; Dupuy, J.; Day, R.; Salzet, M.;

Fournier, I.; Wisztorski, M. Development of Liquid Microjunction Extraction Strategy for Improving Protein Identification from Tissue Sections. *J. Proteomics* **2013**, *79*, 200–218.

(164) Schober, Y.; Schramm, T.; Spengler, B.; Römpp, A. Protein Identification by Accurate Mass Matrix-Assisted Laser Desorption/ionization Imaging of Tryptic Peptides. *Rapid Commun. Mass Spectrom.* **2011**, *25* (17), 2475–2483.

(165) Schober, Y.; Guenther, S.; Spengler, B.; Römpp, A. High-Resolution Matrix-Assisted Laser Desorption/ionization Imaging of Tryptic Peptides from Tissue. *Rapid Commun. Mass Spectrom.* **2012**, *26* (9), 1141–1146.

(166) Stauber, J.; MacAleese, L.; Franck, J.; Claude, E.; Snel, M.; Kaletas, B. K.; Wiel, I. M. V. D.; Wisztorski, M.; Fournier, I.; Heeren, R. M. A. On-Tissue Protein Identification and Imaging by MALDI-Ion Mobility Mass Spectrometry. *J. Am. Soc. Mass Spectrom.* **2010**, *21* (3), 338–347.

(167) Enthaler, B.; Trusch, M.; Fischer, M.; Rapp, C.; Pruns, J. K.; Vietzke, J.-P. P. MALDI Imaging in Human Skin Tissue Sections: Focus on Various Matrices and Enzymes. *Anal. Bioanal. Chem.* **2013**, *405* (4), 1159–1170.

(168) Ronci, M.; Sharma, S.; Chataway, T.; Burdon, K. P.; Martin, S.; Craig, J. E.; Voelcker, N. H. MALDI-MS-Imaging of Whole Human Lens Capsule. *J. Proteome Res.* **2011**, *10* (8), 3522–3529.

(169) Cillero-Pastor, B.; Eijkel, G. B.; Kiss, A.; Blanco, F. J.; Heeren, R. M. A. Matrix-Assisted Laser Desorption Ionization-Imaging Mass Spectrometry: A New Methodology to Study Human Osteoarthritic Cartilage. *Arthritis Rheum.* **2013**, *65* (3), 710–720.

(170) Peffers, M. J.; Cillero-Pastor, B.; Eijkel, G. B.; Clegg, P. D.; Heeren, R. M. A. Matrix Assisted Laser Desorption Ionization Mass Spectrometry Imaging Identifies Markers of Ageing and Osteoarthritic Cartilage. *Arthritis Res. Ther.* **2014**, *16* (3), R110.

(171) Andersson, M.; Groseclose, M. R.; Deutch, A. Y.; Caprioli, R. M. Imaging Mass Spectrometry of Proteins and Peptides: 3D Volume Reconstruction. *Nat. Methods* **2008**, *5* (1), 101–108.

(172) Walch, A.; Rauser, S.; Höfler, H. MALDI Imaging Mass Spectrometry on Formalin-Fixed Paraf N-Embedded Tissues. In *Guidelines for Molecular Analysis in Archive Tissues*; Stanta, G., Ed.; Springer-Verlag Berlin Heidelberg, 2011; pp

293–298.

(173) Casadonte, R.; Kriegsmann, M.; Deininger, S.; Amann, K.; Paape, R.; Belau, E.; Suckau, D.; Fuchser, J.; Beckmann, J.; Becker, M.; et al. Imaging Mass Spectrometry Analysis of Renal Amyloidosis Biopsies Reveals Protein Co-Localization with Amyloid Deposits. *Anal. Bioanal. Chem.* **2015**, *407* (18), 5323–5331.

(174) Casadonte, R.; Kriegsmann, M.; Zweynert, F.; Friedrich, K.; Baretton, G.; Bretton, G.; Otto, M.; Deininger, S.-O.; Paape, R.; Belau, E.; et al. Imaging Mass Spectrometry to Discriminate Breast from Pancreatic Cancer Metastasis in Formalin-Fixed Paraffin-Embedded Tissues. *Proteomics* **2014**, *14* (7–8), 956–964.

(175) Gravius, S.; Randau, T. M.; Casadonte, R.; Kriegsmann, M.; Friedrich, M. J.; Kriegsmann, J. Investigation of Neutrophilic Peptides in Periprosthetic Tissue by Matrix-Assisted Laser Desorption Ionisation Time-of-Flight Imaging Mass Spectrometry. *Int. Orthop.* **2015**, *39* (3), 559–567.

(176) Gustafsson, J. O. R.; Eddes, J. S.; Meding, S.; McColl, S. R.; Oehler, M. K.; Hoffmann, P. Matrix-Assisted Laser Desorption/ionization Imaging Protocol for in Situ Characterization of Tryptic Peptide Identity and Distribution in Formalin-Fixed Tissue. *Rapid Commun. Mass Spectrom.* **2013**, *27* (6), 655–670.

(177) Gustafsson, J. O. R.; Eddes, J. S.; Meding, S.; Koudelka, T.; Oehler, M. K.; McColl, S. R.; Hoffmann, P. Internal Calibrants Allow High Accuracy Peptide Matching between MALDI Imaging MS and LC-MS/MS. *J. Proteomics* **2012**, *75* (16), 5093–5105.

(178) Lemaire, R.; Desmons, A.; Tabet, J. C.; Day, R.; Salzet, M.; Fournier, I. Direct Analysis and MALDI Imaging of Formalin-Fixed, Paraffin-Embedded Tissue Sections. *J. Proteome Res.* **2007**, *6* (4), 1295–1305.

(179) O'Rourke, M. B.; Raymond, B. B. A.; Djordjevic, S. P.; Padula, M. P. A Versatile Cost-Effective Method for the Analysis of Fresh Frozen Tissue Sections via Matrix-Assisted Laser Desorption/ionisation Imaging Mass Spectrometry. *Rapid Commun. Mass Spectrom.* **2015**, *29* (7), 637–644.

(180) Stauber, J.; MacAleese, L.; Franck, J.; Claude, E.; Snel, M.; Kaletas, B. K.; Wiel, I. M. V. D.; Wisztorski, M.; Fournier, I.; Heeren, R. M. a. On-Tissue Protein Identification and Imaging by MALDI-Ion Mobility Mass Spectrometry. *J. Am. Soc. Mass Spectrom.* **2010**, *21* (3), 338–347.

(181) Stauber, J.; Lemaire, R.; Franck, J.; Bonnel, D.; Croix, D.; Day, R.; Wisztorski, M.; Fournier, I.; Salzet, M. MALDI Imaging of Formalin-Fixed Paraffin-Embedded Tissues: Application to Model Animals of Parkinson Disease for Biomarker Hunting. *J. Proteome Res.* **2008**, *7*, 969–978.

(182) Taverna, D.; Nanney, L. B.; Pollins, A. C.; Sindona, G.; Caprioli, R. M. Spatial Mapping by Imaging Mass Spectrometry Offers Advancements for Rapid Definition of Human Skin Proteomic Signatures. *Exp. Dermatol.* **2011**, *20* (8), 642–647.

(183) Nakanishi, T.; Ito, M.; Nirasawa, T.; Tsuji, M.; Takubo, T. Topologies of Amyloidogenic Proteins in Congo Red-Positive Sliced Sections of Formalin-Fixed Paraffin Embedded Tissues by MALDI-MS Imaging Coupled with on-Tissue Tryptic Digestion. *Clin. Biochem.* **2013**, *46* (15), 1595–1600.

(184) De Sio, G.; Smith, A. J.; Galli, M.; Garancini, M.; Chinello, C.; Bono, F.; Pagni, F.; Magni, F. A MALDI-Mass Spectrometry Imaging Method Applicable to Different Formalin-Fixed Paraffin-Embedded Human Tissues. *Mol. Biosyst.* **2015**, *11* (6), 1507–1514.

Appendix

Supplementary Table 1 – Summary of literature search for method protocol steps for preparing a tissue for bottom-up proteomic MALDI-MSI analysis.

Cut Tissue	Mount Tissue	Dry	Wash	Trypsin Deposition	Incubation	Matrix Deposition	Ref
10 µm	thaw-mounted			50 mM ammonium bicarbonate (pH 8.4) with 0.5% OcGlc deposited in 5 layers of 2 µL/ using SunCollect sprayer	o.n. at 37 ˚C with 5% carbon dioxide	5 mg/mL CHCA (equimolar aniline - 1 mL has 2.4 µL) using SunCollect. First two layers at 3 µL/minute and last three layers at 3.5 µL/minute	[159]
10 µm	RT slide	15 minutes in vacuum desiccator	1. 2x 70% EtOH 2. 100% EtOH	100 ng/µL in 50 mM ammonium bicarbonate with ImagePrep using standard protocol	2 hours, 4 hours, and o.n. at 37 ˚C in humidity chamber	DHB (30 mg/mL in 50:50 methanol/water/1% TFA) or CHCA (5 mg/mL in 50:50 ACN/water/2% TFA) using modified ImagePrep methods	[160]

10 µm	thaw-mounted		1. EtOH 50% to 90% 1 minute 2. chloroform 30 seconds	0.05 µg/µL in 0.1% OcGlc using Sun-Collect spotter	2 hours at 37 ˚C with 5% carbon dioxide	10 mg/mL CHCA with aniline in ACN:water:TFA 1:1:0.1	161
10 µm			1. 95% EtOH 15 seconds 2. chloroform 1 minute	20 µg/mL trypsin in 20 mM ammonium bicarbonate using printer	2 hours 37 ˚C in humid atmosphere	10 mg/mL CHCA in ACN 0.1% TFA (6:4) using printer	162
10 µm	thaw-mounted	10 minutes in vacuum desiccator	1. 70% EtOH 30 seconds 2. 95% EtOH 30 seconds 3. chloroform 30 seconds	20 µg/mL trypsin in 50mM ammonium bicarbonate total of 40 nL per spot with printer	1 hour of deposition, no additional incubation time	CHCA/aniline (1.5 eq aniline (36 µL for 5 mL) in 10 mg/mL 7:3 ACN/water/0.1% TFA	163
20 µm	thaw-mounted	30 minutes in desiccator	1. Aerni et al. method 2. EtOH:acetic	0.1 µg/µL in 30mM ammonium bicarbonate	2.5h at RT	30 mg/mL DHB in 50:50 acetone/water/0.5% TFA with pneumatic sprayer	164

			acid:water 90:9:1	manually deposited			
20 µm	thaw-mounted	30 minutes in desiccator	1. Aerni et al. method 2. EtOH:acetic acid:water 90:9:1 30 seconds 3. water to neutralize pH	0.05 µg/µL trypsin in 10mM ammonium bicarbonate with home-built pneumatic sprayer	incubated between trypsin deposition; at end incubated at 37 ˚C at 100% humidity o.n.	30 mg/mL DHB in 50:50 acetone/water/0.5% TFA with pneumatic sprayer	[165]
10 µm			chloroform 5 seconds	0.05 µg/µL in water with printer		10 mg/mL CHCA in ACN/TFA 0.1% (6:4) with ImagePrep then sonicated for 2 minutes	[166]
10 µm	corona-discharged adhesion		1. 2x 70% EtOH 1 minute 2. 100% EtOH 2 minutes	100 ng/µL prepared in 50mM acetic acid and activated in 80 mM ammonium bicarbonate. 200 µL	o.n. at 37 ˚C in humid atmosphere then dried in desiccator for 30 minutes	9-AA, SA, and CHCA using ImagePrep default concentrations and depositions (except 9-AA with DHB deposition)	[167]

				deposited with ImagePrep			
whole lens			1. water (extensively) 2. 70% EtOH 1 minute 3. 100% EtOH 1 minute	100 ng/µL in 10 mM ammonium bicarbonate with ImagePrep	1 hour	7 g/L CHCA in 50% acetonitrile (0.2% TFA) with ImagePrep	168
10 µm			1. 100% EtOH 30 seconds 2. 70% EtOH 2 minutes 3. chloroform 30 seconds	50 ng/µL in 0.01% OcGlc with printer	o.n. at 37 ˚C	10 g/L CHCA in 50% acetonitrile (0.1% TFA) with ImagePrep	169
12 µm	thaw-mounted	10 minutes in vacuum desiccator	1. 70% EtOH 30 sections 2. chloroform 30 seconds	50 ng/µL in 0.01% OcGlc with printer	o.n. at 37 ˚C	10 g/L CHCA in 50% acetonitrile (0.1% TFA) with ImagePrep	170
12 µm	thaw-mounted	30 minutes	1. 70% EtOH 2. 2x 95%	20 µg in 40 µL of 50 mM		CHCA or DHB	171

		in vacuum desiccator	EtOH 3. 90:9:1 EtOH acetic acid water 30 seconds (30 seconds each for protein analysis and 10 seconds each for peptide analysis)	acetic acid. Then 200 µL 100 mM ammonium bicarbonate (pH 8)				

Supplementary Table 2 – MALDI-MSI bottom-up proteomic analysis Mann-Whitney U test p-values.

Wash Optimization Experiment				
Peak Intensity	basic	basic + acetic	basic + bicarb	Carnoy's
basic + acetic	< 2e-16	-	-	-
basic + bicarb	< 2e-16	0.017	-	-
Carnoy's	0.017	< 2e-16	< 2e-16	-
no wash	0.08	< 2e-16	< 2e-16	1.90E-05
Peak Count	basic	basic + acetic	basic + bicarb	Carnoy's
basic + acetic	2.30E-10	-	-	-
basic + bicarb	8.80E-06	0.0034	-	-
Carnoy's	0.0034	3.50E-13	6.30E-10	-
no wash	0.0093	0.511	0.3678	0.0015
Trypsin Digestion Incubation Time Experiment			MCAEF Optimization Experiment	
Peak Intensity	Peak Count		Peak Intensity	Peak Count
< 2.2e-16	0.0004237		< 2.2e-16	5.91E-05

Supplementary Table 3 – Summary of recently published proteomic MALDI-MSI experiments on FFPE tissues.
RT – room temperature; ACN – acetonitrile; secs – seconds; min – minutes; hr – hours; TFA – trifluoroacetic acid

Ref	172	157	33	173	174	159
Cut Tissue	not described in detail	4 µm	5 µm	2 µm	5 µm	5 µm
Mount Tissue	not described in detail	not described in detail	water mount; first into RT, then into water at 47-50 ˚C	not described in detail	not described in detail	not described in detail
Heat Fix Tissue	10 min at 60˚C hotplate	70 ˚C for 1h	37 ˚C for 8 hours	not described in detail	not described in detail	stored at RT
Air Dry Tissue	not described in detail	not described in detail	not described in detail	not described in detail	not described in detail	not described in detail
Paraffin Removal	2x xylene for 20 min	2x xylene 8 min	2x xylene 3 min	2x xylene 3 min	2x xylene 3 min	not described in detail
Wash	1. 100% EtOH 5 min 2. 95% EtOH 5 min 3. 80% EtOH 5 min 4. 70% EtOH 5 min	not described in detail	1. 2x 100% EtOH 1 min 2. 1x 95% EtOH 1 min 3. 1x 70% EtOH 1 min 4. 2x water 3 min	1. 2x 100% EtOH 1 min 2. 96% EtOH 1 min 3. 70% EtOH 1 min	1. 2x 100% EtOH 1 min 2. 95% EtOH 1 min 3. 70% EtOH 1 min	1. water 2. dry 3. 70% EtOH 1 min 4. 90% EtOH 1 min 5. chloroform 15 secs
Antigen Retrieval	1. Warm up 10 mM Tris Base-1 M MEDTA pH 9.0 solution to boiling in microwave 2. transfer slide to solution	not described in detail	using 10 mM TRIS buffer and "decloaking chamber" program; allow to cool for 10 min on counter	10 mM Tris buffer (pH 9.0) at 95 C for 20 min	10 mM Tris buffer (pH 9.0) at 95 C for 20 min	heated for 4 minutes at 50% power in 0.01M trisodium citrate (pH 6.3) then cooled to RT

	3. boil for 20 min in the microwave					
Wash	water 5 min	not described in detail	rinse 5x by pouring out half of liquid and topping up with water; final rinse with 100% water	not described in detail	not described in detail	not described in detail
Dry	10 min at 40˚C hotplate	air dry	stand vertically on paper towel until completely dry; then vacuum desiccator until needed	not described in detail	not described in detail	air dry
Trypsin Deposition	Prepare 0.5 µg/µL trypsin in 50 mM acetic acid. Dilute 50 µL of stock with 500 µL 100 mM ammonium bicarbonate using microspotter	no trypsin digestion	100 µg in 200 µL 50 mM acetic acid. 100 µL of stock with 500 µL 100 mM ammonium bicarbonate then add 60 µL acetonitrile in water and vortex; deposition with printer	0.1 µg/µL in 40 mM ammonium bicarbonate and 10% acetonitrile ImagePrep (24 cycles)	0.1 µg/µL trypsin in 40 mM ammonium bicarbonate and 10% ACN using ImagePrep using standard protocol	50 mM ammonium bicarbonate (pH 8.4) with 0.5% OcGlc deposited in 5 layers of 2 µL/min using SunCollect sprayer
Trypsin Digestion	5 min at RT	no trypsin digestion	not described	37 C for 1.5h in humidity chamber	1.5 h at 37 C in humidity chamber	o.n. at 37 ˚C with 5% CO2
Matrix Deposition	CHCA (7 g/L in ACN/water 1:1	10 mg/mL 9-AA in 70%	CHCA (10 mg/mL in 50% ACN and 0.5%	CHCA (7 mg/mL in 50/50	CHCA (7 mg/mL in 50%	5 mg/mL CHCA (containing

	with 0.2% TFA) with ImagePrep with standard CHCA method	methanol with SunCollect sprayer	TFA sonicate for 10 minutes; deposition with printer	ACN/0.5% TFA using ImagePrep	acetonitrile and 0.5% TFA) using ImagePrep using standard protocol	equimolar aniline - 1 mL has 2.4 µL) using SunCollect. First two layers at 3 µL/min and last three layers at 3.5 µL/min

Supplementary Table 4 – Continuation of Supplementary Table 3 – Summary of recently published proteomic MALDI-MSI experiments on FFPE tissues.
RT – room temperature; ACN – acetonitrile; secs – seconds; min – minutes; hr – hours; TFA – trifluoroacetic acid

Ref	160	161	175	176	177	178
Cut Tissue	6 µm	10 µm	3 µm	6 µm	6 µm	10 µm
Mount Tissue	water mounted then dried at 37 C for 16 hr	thaw mounted	not described in detail	water mounted	water mounted	not described in detail
Heat Fix Tissue	60 C for 1 hr	not described in detail	not described in detail	in Coplin jar at RT; or Coplin jar incubated at 56 ˚C	not described in detail	not described in detail
Air Dry Tissue	not described in detail	not described in detail	not described in detail	tissue face up on heating block at 60 ˚C for 1 hr	not described in detail	not described in detail
Paraffin Removal	2x xylene 5 min	2x xylene 5 min	not described in detail	2x 100% xylene for 5 min	not described in detail	2x xylene 5 min
Wash	1. 2x 100% EtOH 2 minutes 2. 2x 10mM ammonium bicarbonate 3 minutes	1. EtOH from 100% to 70% 2 min 2. CHCl3 30 seconds	not described in detail	2x 100 EtOH 2 min	not described in detail	1. 100% EtOH 2. 95% EtOH 3. 70% EtOH
Antigen Retrieval	1. 10 mM citric acid (pH 6.0) pulse boiled in a microwave for 10 min 2. 30 min at 98 C water bath 3. cooled for 5 min	not described in detail	"antigen retrieved"	1. place slide in Coplin jar 2. 2x 10mM ammonium bicarbonate 5 min	not described in detail	not described in detail

				3. 10mM citric acid monohydrate at pH 6, microwave until boiling, maintain near boiling point for 10 min 4. transfer Coplin jar to heating block at 98 ˚C for 30 min; allow to cool to RT when done		
Wash	2x 10 mM ammonium bicarbonate 1 min	not described in detail	not described in detail	2x 10mM ammonium bicarbonate 1 min	not described in detail	not described in detail
Dry	vacuum desiccator 5 minutes	not described in detail	not described in detail	5-10 min in desiccator no vacuum	not described in detail	RT
Trypsin Deposition	100 ng/µL in 50 mM Tris base (pH 8.3) with ImagePrep using standard protocol	0.05 µg/µL in 0.1% OcGlc using Sun-Collect spotter	0.5 µg/µL with ImagePrep	1. 100 µg trypsin + 200 µL 5 mM sodium bicarbonate 2.40 µL above + 160 µL 26 mM sodium bicarbonate	200 µL 100 ng/µL in 25 mM ammonium bicarbonate using ImagePrep	0.1 µg/µL trypsin in 25 mM ammonium bicarbonate filtered microspotter

				3. 200 µL into ImagePrep		
Trypsin Digestion	2 hr at 37 C in humidity chamber	2hr at 37 ˚C with 5% CO2	1.5hr at 37 C in humidity chamber	immediately into humid environment at 37 ˚C for 2hr	2 hr in humid box at 37 C	not described in detail
Matrix Deposition	DHB (30 mg/mL in 50:50 methanol/water/1% TFA) or CHCA (5 mg/mL in 50:50 ACN/water/2% TFA) with ImagePrep with modified matrix deposition methods	10 mg/mL CHCA with ANI in ACN:water:TFA 1:1:0.1	CHCA (7 mg/mL in 50/50 ACN/0.5% TFA) with ImagePrep	7 mg/mL CHCA (> 5mL) with default CHCA method	CHCA (7 mg/mL in 50% acetonitrile and 0.2% TFA) using ImagePrep	CHCA

Supplementary Table 5 – Continuation of Supplementary Table 3 and Supplementary Table 4 - Summary of recently published proteomic MALDI-MSI experiments on FFPE tissues.
RT – room temperature; ACN – acetonitrile; secs – seconds; min – minutes; hr – hours; TFA – trifluoroacetic acid

Ref	179	180	181	182	183	184
Cut Tissue	5 µm	10 µm	10 µm	12 µm	12 µm	5 µm
Mount Tissue	water mounted	not described in detail	not described in detail	thaw mounted	not described in detail	not described in detail
Heat Fix Tissue	80 ˚C for 20 min	not described in detail	not described in detail	not described in detail	not described in detail	1 hr at 65 C
Air Dry Tissue	not described in detail	not described in detail	not described in detail	10 min in desiccator	not described in detail	not described in detail
Paraffin Removal	2x xylene 2 min	2x toluene 5 min	2x toluene 5 min		not described in detail	3x xylene 2 min
Wash	1. 70% EtOH 30 secs 2. 95% EtOH 30 secs 3. Carnoy's fluid 2 min 4. 100% EtOH 30 secs 5. water 30 secs 6. 100% EtOH 30 secs	1. 100% EtOH 2. 96% EtOH 3. 70% EtOH 4. 30% EtOH	1. 100% EtOH 2. 96% EtOH 3. 70% EtOH 4. 30% EtOH	1. 70% isopropanol 30 secs 2. 95% isopropanol 30 secs	not described in detail	1. 2x 100% EtOH 3 min 2. 70% EtOH 3 min 3. 2x water 2 min
Antigen Retrieval	submerged in 20mmol Tris-HCl (pH 8.8) then in pressure cooker for 15 min	not described in detail	not described in detail	not described in detail	not described in detail	10 mM citric acid at 97 C for 30 min
Wash	not described in detail	not described in detail	not described in detail	not described in detail	not described in detail	Coplin jar with water

						for 2 minutes
Dry	cool and dried at RT	RT	RT	not described in detail	not described in detail	not described in detail
Trypsin Deposition	1. 10 mL of 1 mg/mL trypsin in water pipetted onto tissue 2. dried at 25 ˚C with filter 3. 650 µL 50:50 50mM ammonium bicarbonate/100% ACN	0.05 µg/µL in water with printer	0.033 µg/µL trypsin in 25 mM Tris buffer (pH 7.4)	Prepare trypsin in 50 mM acetic acid. Dilute stock with 500 µL 100 mM ammonium bicarbonate for final conc. Of 0.038 µg/µL using microspotter	20 µg in 200 µL 50 mM ammonium bicarbonate buffer (pH 8) for final concentration of 0.5 µg/µL with ImagePrep	100 ng/µL with ImagePrep
Trypsin Digestion	Vapour chamber at 37 ˚C overnight	not described in detail	RT, trypsin spotted ever 10 min. Stopped by rinsing in 80% cold ethanol; allowed to dry at RT	RT for 3 hr	3hr at 37 C in humid conditions	2 hr at 45 C
Matrix Deposition	1. CHCA sublimated onto slide to achieve ideal coverage of 0.2 mg/cm2 2. 650 µL of 50% CAN/0.1% TFA pipetted onto tissue	10 mg/mL CHCA in ACN/TFA 0.1% (6:4) with ImagePrep then sonicated for 2 min	CHCA (10 mg/mL in ACN/water, TFA 0.1% (6:4) with 1 eq aniline); sonicated for 2 min	CHCA (10 mg/mL in 1:1 ACN/0.5% TFA	7 g/L CHCA with ImagePrep	CHCA (7 mg/mL) with ImagePrep

	3. Vapour chamber at 37 ˚C for 1hr					

Supplementary Table 6 – Summary of all bottom-up proteomic m/z values found in prostate cancer by MALD-MSI accurate mass matched to LC-MS/MS data for peptide identification and corresponding protein assignments for fresh frozen prostate cancer

Protein	Protein Accession Number	Obs. m/z
Calmodulin OS=Homo sapiens GN=CALM1 PE=1 SV=2 - [CALM_HUMAN]	P62158	805.4189
-	No protein ID	806.3283
Transgelin OS=Homo sapiens GN=TAGLN PE=1 SV=4 - [TAGL_HUMAN]	Q01995	806.3818
-	No protein ID	806.4262
Lysozyme C OS=Homo sapiens GN=LYZ PE=1 SV=1 - [LYSC_HUMAN]	P61626	811.3777
-	No protein ID	815.4378
Histone H2B type 1-O OS=Homo sapiens GN=HIST1H2BO PE=1 SV=3 - [H2B1O_HUMAN]; Histone H2B type 1-K OS=Homo sapiens GN=HIST1H2BK PE=1 SV=3 - [H2B1K_HUMAN]	P23527;O60814	816.4570
Hemoglobin subunit alpha OS=Homo sapiens GN=HBA1 PE=1 SV=2 - [HBA_HUMAN]; HCG1745306, isoform CRA_a OS=Homo sapiens GN=HBA2 PE=3 SV=1 - [G3V1N2_HUMAN]; SWISS-PROT:P01966 (Bos taurus) Hemoglobin subunit alpha	P69905; G3V1N2; P01966	818.4402
Histone H1.0 OS=Homo sapiens GN=H1F0 PE=1 SV=3 - [H10_HUMAN]	P07305	837.4211
Histone H1.3 OS=Homo sapiens GN=HIST1H1D PE=1 SV=2 - [H13_HUMAN]	P16402	842.5088
Calponin-1 OS=Homo sapiens GN=CNN1 PE=1 SV=2 - [CNN1_HUMAN]	P51911; K7ENC5	846.4807

Histone H2A (Fragment) OS=Homo sapiens GN=H2AFJ PE=3 SV=1 - [H0YFX9_HUMAN]	H0YFX9	850.5260
Transgelin OS=Homo sapiens GN=TAGLN PE=1 SV=4 - [TAGL_HUMAN]	Q01995	854.3818
Prostate-specific antigen OS=Homo sapiens GN=KLK3 PE=1 SV=2 - [KLK3_HUMAN]	P07288	854.4022
-	No protein ID	856.5244
Calponin-1 OS=Homo sapiens GN=CNN1 PE=1 SV=2 - [CNN1_HUMAN]	P51911	860.3998
Collagen alpha-2(I) chain OS=Homo sapiens GN=COL1A2 PE=1 SV=7 - [CO1A2_HUMAN]	P08123	868.4632
-	No protein ID	870.5407
-	No protein ID	874.4816
Tropomyosin 1 (Alpha) isoform 3 OS=Homo sapiens GN=TPM1 PE=3 SV=1 - [D9YZV3_HUMAN]	D9YZV3;P09493-7;Q6ZN40;P06753	875.4494
Serum albumin OS=Homo sapiens GN=ALB PE=1 SV=2 - [ALBU_HUMAN]	P02768	875.5108
Cathepsin B (Fragment) OS=Homo sapiens GN=CTSB PE=4 SV=1 - [E9PJ67_HUMAN]	E9PJ67	876.4537
Creatine kinase B-type OS=Homo sapiens GN=CKB PE=1 SV=1 - [KCRB_HUMAN]	P12277	878.5060
Serum albumin OS=Homo sapiens GN=ALB PE=1 SV=2 - [ALBU_HUMAN]	P02768	880.4397
Actin, gamma-enteric smooth muscle OS=Homo sapiens GN=ACTG2 PE=1 SV=1 - [ACTH_HUMAN]; Nuclease-sensitive	P63267;P60709	880.5002

element-binding protein 1 OS=Homo sapiens GN=YBX1 PE=1 SV=3 - [YBOX1_HUMAN]		
Tropomyosin 1 (Alpha) isoform 3 OS=Homo sapiens GN=TPM1 PE=3 SV=1 - [D9YZV3_HUMAN]	D9YZV8;P09493-3;D9YZV3;P09493-7;Q6ZN40;J3KN67;P06753;P07951-2;P07951-3;P67936;P67936-2	894.4687
Myosin, heavy chain 11, smooth muscle OS=Homo sapiens GN=MYH11 PE=2 SV=1 - [Q3MIV8_HUMAN]	Q3MIV8	901.5003
Myosin, heavy chain 11, smooth muscle OS=Homo sapiens GN=MYH11 PE=2 SV=1 - [Q3MIV8_HUMAN]	Q3MIV8	903.5122
Isoform 2 of Tropomyosin beta chain OS=Homo sapiens GN=TPM2 - [TPM2_HUMAN]	P07951-2;P07951-3	916.4738
Complement C3 OS=Homo sapiens GN=C3 PE=1 SV=2 - [CO3_HUMAN]	P01024	917.5620
High mobility group protein B1 OS=Homo sapiens GN=HMGB1 PE=2 SV=1 - [Q5T7C4_HUMAN]	Q5T7C4	925.4492
-	No protein ID	926.5052
Serum albumin OS=Homo sapiens GN=ALB PE=1 SV=2 - [ALBU_HUMAN]	P02768	927.4935
Thiosulfate sulfurtransferase/rhodanese-like domain-containing protein 1 OS=Homo sapiens GN=TSTD1 PE=1 SV=3 - [TSTD1_HUMAN]	Q8NFU3	930.5520
-	No protein ID	930.5640
Hemoglobin subunit beta OS=Homo sapiens GN=HBB PE=1 SV=2 - [HBB_HUMAN]; Hemoglobin subunit delta OS=Homo sapiens GN=HBD PE=1 SV=2 - [HBD_HUMAN]	P68871	932.5198

Serum albumin OS=Homo sapiens GN=ALB PE=1 SV=2 - [ALBU_HUMAN]	P02768	940.4482
Synemin OS=Homo sapiens GN=SYNM PE=1 SV=2 - [SYNEM_HUMAN]	O15061	943.4992
Histone H2A OS=Homo sapiens GN=H2AFV PE=3 SV=3 - [A8MQC5_HUMAN]	A8MQC5	944.5313
-	No protein ID	948.5359
-	No protein ID	948.5371
Vitamin D-binding protein OS=Homo sapiens GN=GC PE=1 SV=1 - [VTDB_HUMAN]	P02774	952.5094
Hemoglobin subunit beta OS=Homo sapiens GN=HBB PE=1 SV=2 - [HBB_HUMAN]	P68871; P02042	952.5098
Hemoglobin subunit delta OS=Homo sapiens GN=HBD PE=1 SV=2 - [HBD_HUMAN]	P02042	959.5292
Serum albumin OS=Homo sapiens GN=ALB PE=1 SV=2 - [ALBU_HUMAN]	P02768	960.5628
-	No protein ID	961.4336
-	No protein ID	974.4922
Calponin-1 OS=Homo sapiens GN=CNN1 PE=1 SV=2 - [CNN1_HUMAN]	P51911; K7ENC5	974.5785
Actin, gamma-enteric smooth muscle OS=Homo sapiens GN=ACTG2 PE=1 SV=1 - [ACTH_HUMAN]; Nuclease-sensitive element-binding protein 1 OS=Homo sapiens GN=YBX1 PE=1 SV=3 - [YBOX1_HUMAN]	P63267; P60709	976.4475

Serum albumin OS=Homo sapiens GN=ALB PE=1 SV=2 - [ALBU_HUMAN]	P02768	984.4885
Isoform 2 of Nucleophosmin OS=Homo sapiens GN=NPM1 - [NPM_HUMAN]	P06748-2	985.5685
Heat shock protein beta-1 OS=Homo sapiens GN=HSPB1 PE=1 SV=2 - [HSPB1_HUMAN]	P04792	987.6087
Histone H4 OS=Homo sapiens GN=HIST1H4A PE=1 SV=2 - [H4_HUMAN]	P62805	989.5786
Calponin-1 OS=Homo sapiens GN=CNN1 PE=1 SV=2 - [CNN1_HUMAN]	P51911	993.5182
-	No protein ID	999.5111
Superoxide dismutase OS=Homo sapiens GN=SOD2 PE=2 SV=1 - [B3KUK2_HUMAN]	B3KUK2	1004.5524
Calponin-1 OS=Homo sapiens GN=CNN1 PE=1 SV=2 - [CNN1_HUMAN]	P51911	1009.5142
Apolipoprotein A-I OS=Homo sapiens GN=APOA1 PE=1 SV=1 - [APOA1_HUMAN]	P02647	1012.5771
Serum albumin OS=Homo sapiens GN=ALB PE=1 SV=2 - [ALBU_HUMAN]	P02768	1013.6001
Isoform 2 of Alpha-1-antitrypsin OS=Homo sapiens GN=SERPINA1 - [A1AT_HUMAN]	P01009-2	1015.6156
Serum albumin OS=Homo sapiens GN=ALB PE=1 SV=2 - [ALBU_HUMAN]	P02768	1019.5796
Profilin-1 OS=Homo sapiens GN=PFN1 PE=1 SV=2 - [PROF1_HUMAN]	P07737	1023.5584

Selenium-binding protein 1 OS=Homo sapiens GN=SELENBP1 PE=1 SV=2 - [SBP1_HUMAN]	Q13228	1025.5993
Protein cramped-like OS=Homo sapiens GN=CRAMP1L PE=4 SV=1 - [J3KR07_HUMAN]	J3KR07	1028.6004
Desmin OS=Homo sapiens GN=DES PE=1 SV=3 - [DESM_HUMAN]	P17661	1032.5416
Mimecan OS=Homo sapiens GN=OGN PE=1 SV=1 - [MIME_HUMAN]	P20774	1039.6145
Prolargin OS=Homo sapiens GN=PRELP PE=1 SV=1 - [PRELP_HUMAN]	P51888	1044.5218
Tropomyosin 1 (Alpha) isoform 3 OS=Homo sapiens GN=TPM1 PE=3 SV=1 - [D9YZV3_HUMAN]	D9YZV8;P09493-7;P07951-3	1045.5299
Trypsin - Sus scrofa (Pig). - [TRYP_PIG]	P00761 SWISS-PROT:P00761	1045.5639
Calponin-1 OS=Homo sapiens GN=CNN1 PE=1 SV=2 - [CNN1_HUMAN]	P51911	1046.5259
-	No protein ID	1060.4695
Mimecan OS=Homo sapiens GN=OGN PE=1 SV=1 - [MIME_HUMAN]	P20774	1060.5427
Ubiquitin (Fragment) OS=Homo sapiens GN=RPS27A PE=4 SV=1 - [J3QTR3_HUMAN]	J3QTR3	1067.6206
CD99 antigen OS=Homo sapiens GN=CD99 PE=4 SV=1 - [A6NIW1_HUMAN]	A6NIW1	1069.5368
Hemoglobin subunit alpha OS=Homo sapiens GN=HBA1 PE=1 SV=2 - [HBA_HUMAN]; HCG1745306, isoform CRA_a OS=Homo	P69905; G3V1N2; P01966	1071.5542

sapiens GN=HBA2 PE=3 SV=1 - [G3V1N2_HUMAN]; SWISS-PROT:P01966 (Bos taurus) Hemoglobin subunit alpha		
Isoform 2 of Tropomyosin beta chain OS=Homo sapiens GN=TPM2 - [TPM2_HUMAN]	P07951-2;P67936-2;P09493-3;D9YZV3;D9YZV8;J3KN67;P06753;P09493-7;Q6ZN40	1073.5598
-	No protein ID	1078.5371
Histone H2B type 1-M OS=Homo sapiens GN=HIST1H2BM PE=1 SV=3 - [H2B1M_HUMAN]	Q99879	1078.5636
-	No protein ID	1080.5428
Transgelin OS=Homo sapiens GN=TAGLN PE=1 SV=4 - [TAGL_HUMAN]	Q01995	1082.4636
Isoform 2 of Hamartin OS=Homo sapiens GN=TSC1 - [TSC1_HUMAN]	Q92574-2	1082.4636
Hemoglobin subunit alpha OS=Homo sapiens GN=HBA1 PE=1 SV=2 - [HBA_HUMAN]; HCG1745306, isoform CRA_a OS=Homo sapiens GN=HBA2 PE=3 SV=1 - [G3V1N2_HUMAN]; SWISS-PROT:P01966 (Bos taurus) Hemoglobin subunit alpha	P69905;G3V1N2	1087.5477
-	No protein ID	1090.5688
Purkinje cell protein 4 OS=Homo sapiens GN=PCP4 PE=2 SV=3 - [PCP4_HUMAN]	P48539	1090.6004
Hemoglobin subunit beta OS=Homo sapiens GN=HBB PE=1 SV=2 - [HBB_HUMAN]; Hemoglobin subunit delta OS=Homo sapiens GN=HBD PE=1 SV=2 - [HBD_HUMAN]	P68871; P02042	1101.5498
-	No protein ID	1104.6289
-	No protein ID	1105.5528

Hemoglobin subunit beta OS=Homo sapiens GN=HBB PE=1 SV=2 - [HBB_HUMAN]; Hemoglobin subunit delta OS=Homo sapiens GN=HBD PE=1 SV=2 - [HBD_HUMAN]	P68871; P02042	1126.5643
Zinc-alpha-2-glycoprotein OS=Homo sapiens GN=AZGP1 PE=1 SV=2 - [ZA2G_HUMAN]	P25311	1127.5656
Isoform 2 of Lactotransferrin OS=Homo sapiens GN=LTF - [TRFL_HUMAN]	P02788-2	1129.6015
High mobility group protein B1 OS=Homo sapiens GN=HMGB1 PE=2 SV=1 - [Q5T7C4_HUMAN]	Q5T7C4	1133.6271
Dermatopontin OS=Homo sapiens GN=DPT PE=2 SV=2 - [DERM_HUMAN]	Q07507	1139.5719
Creatine kinase B-type OS=Homo sapiens GN=CKB PE=1 SV=1 - [KCRB_HUMAN]	P12724	1143.5271
Isoform 3B of Myosin light chain kinase, smooth muscle OS=Homo sapiens GN=MYLK - [MYLK_HUMAN]	Q15746-4	1145.5752
Serum albumin OS=Homo sapiens GN=ALB PE=1 SV=2 - [ALBU_HUMAN]	P02768	1149.6144
Hemoglobin subunit beta OS=Homo sapiens GN=HBB PE=1 SV=2 - [HBB_HUMAN]; Hemoglobin subunit delta OS=Homo sapiens GN=HBD PE=1 SV=2 - [HBD_HUMAN]	P68871; P02042	1149.6737
Heat shock protein beta-1 OS=Homo sapiens GN=HSPB1 PE=1 SV=2 - [HSPB1_HUMAN]	P04792	1163.6220
Isoform 2 of Collagen alpha-1(IV) chain OS=Homo sapiens GN=COL4A1 - [CO4A1_HUMAN]	P02545-2	1165.5479

Isoform 2 of Tropomyosin beta chain OS=Homo sapiens GN=TPM2 - [TPM2_HUMAN]	P07951-2;P07951-3;P67936;P67936-2	1170.6736
Actin, gamma-enteric smooth muscle OS=Homo sapiens GN=ACTG2 PE=1 SV=1 - [ACTH_HUMAN]; Nuclease-sensitive element-binding protein 1 OS=Homo sapiens GN=YBX1 PE=1 SV=3 - [YBOX1_HUMAN]	P63267;P60709	1171.5710
Histone H4 OS=Homo sapiens GN=HIST1H4A PE=1 SV=2 - [H4_HUMAN]	P62805	1180.6212
Tropomyosin 1 (Alpha) isoform 3 OS=Homo sapiens GN=TPM1 PE=3 SV=1 - [D9YZV3_HUMAN]	D9YZV8;P09493-3;D9YZV3;P09493-7;Q6ZN40	1186.6682
Tropomyosin 1 (Alpha) isoform 3 OS=Homo sapiens GN=TPM1 PE=3 SV=1 - [D9YZV3_HUMAN]	D9YZV8;P09493-3;D9YZV3;P09493-7;Q6ZN40	1187.5624
-	No protein ID	1193.6511
Isoform 2 of Small ubiquitin-related modifier 2 OS=Homo sapiens GN=SUMO2 - [SUMO2_HUMAN]	P61956-2	1197.5846
Actin, gamma-enteric smooth muscle OS=Homo sapiens GN=ACTG2 PE=1 SV=1 - [ACTH_HUMAN]; Nuclease-sensitive element-binding protein 1 OS=Homo sapiens GN=YBX1 PE=1 SV=3 - [YBOX1_HUMAN]	P63267	1198.7054
Actin, gamma-enteric smooth muscle OS=Homo sapiens GN=ACTG2 PE=1 SV=1 - [ACTH_HUMAN]; Nuclease-sensitive element-binding protein 1 OS=Homo sapiens GN=YBX1 PE=1 SV=3 - [YBOX1_HUMAN]	P63267;P60709	1198.7054
Actin, gamma-enteric smooth muscle OS=Homo sapiens GN=ACTG2 PE=1 SV=1 - [ACTH_HUMAN]; Nuclease-sensitive	P63267;P60709	1198.7057

element-binding protein 1 OS=Homo sapiens GN=YBX1 PE=1 SV=3 - [YBOX1_HUMAN]		
Tropomyosin 1 (Alpha) isoform 3 OS=Homo sapiens GN=TPM1 PE=3 SV=1 - [D9YZV3_HUMAN]	D9YZV8;P09493-7;P07951-3	1201.6214
Isoform 3 of Synaptopodin-2 OS=Homo sapiens GN=SYNPO2 - [SYNP2_HUMAN]	Q9UMS6-3	1203.5577
-	No protein ID	1205.5938
Tropomyosin 1 (Alpha) isoform 3 OS=Homo sapiens GN=TPM1 PE=3 SV=1 - [D9YZV3_HUMAN]	D9YZV8;P09493-3;D9YZV3;P09493-7;Q6ZN40	1210.5553
Transgelin OS=Homo sapiens GN=TAGLN PE=1 SV=4 - [TAGL_HUMAN]	Q01995	1210.5553
Transgelin OS=Homo sapiens GN=TAGLN PE=1 SV=4 - [TAGL_HUMAN]	Q01995	1211.6297
Myosin, heavy chain 11, smooth muscle OS=Homo sapiens GN=MYH11 PE=2 SV=1 - [Q3MIV8_HUMAN]	Q3MIV8	1214.5567
Apolipoprotein A-I OS=Homo sapiens GN=APOA1 PE=1 SV=1 - [APOA1_HUMAN]	P02647	1215.6227
Purkinje cell protein 4 OS=Homo sapiens GN=PCP4 PE=2 SV=3 - [PCP4_HUMAN]	P48539	1218.6959
Cytochrome b-c1 complex subunit 6, mitochondrial OS=Homo sapiens GN=UQCRH PE=1 SV=2 - [QCR6_HUMAN]	P07919	1219.5666
Cold-inducible RNA-binding protein OS=Homo sapiens GN=CIRBP PE=1 SV=1 - [CIRBP_HUMAN]	Q14011	1220.6874
Transgelin OS=Homo sapiens GN=TAGLN PE=1 SV=4 - [TAGL_HUMAN]	Q01995	1221.6375

Transgelin OS=Homo sapiens GN=TAGLN PE=1 SV=4 - [TAGL_HUMAN]	Q01995	1227.6240
Decorin OS=Homo sapiens GN=DCN PE=1 SV=1 - [PGS2_HUMAN]	P07585	1233.6118
Collagen alpha-2(I) chain OS=Homo sapiens GN=COL1A2 PE=1 SV=7 - [CO1A2_HUMAN]	P08123	1235.6086
Tropomyosin 1 (Alpha) isoform 3 OS=Homo sapiens GN=TPM1 PE=3 SV=1 - [D9YZV3_HUMAN]	D9YZV8;P09493-3;D9YZV3;J3KN67;P06753;P07951-2;P07951-3;P09493-7;P67936;P67936-2;Q6ZN40	1243.6535
-	No protein ID	1247.6863
Vitamin D-binding protein OS=Homo sapiens GN=GC PE=1 SV=1 - [VTDB_HUMAN]	P02787	1249.6125
-	No protein ID	1252.5736
Hemoglobin subunit delta OS=Homo sapiens GN=HBD PE=1 SV=2 - [HBD_HUMAN]	P02042	1256.6615
60S ribosomal protein L35a OS=Homo sapiens GN=RPL35A PE=4 SV=1 - [F8WBS5_HUMAN]	F8WBS5	1257.6196
Transgelin OS=Homo sapiens GN=TAGLN PE=1 SV=4 - [TAGL_HUMAN]	Q01995	1260.6238
Musculoskeletal embryonic nuclear protein 1 OS=Homo sapiens GN=MUSTN1 PE=2 SV=2 - [MSTN1_HUMAN]	Q8IVN3	1269.6806
Hemoglobin subunit beta OS=Homo sapiens GN=HBB PE=1 SV=2 - [HBB_HUMAN]; Hemoglobin subunit delta OS=Homo sapiens GN=HBD PE=1 SV=2 - [HBD_HUMAN]	P68871; P02042	1274.7263
14-3-3 protein zeta/delta OS=Homo sapiens GN=YWHAZ PE=2 SV=1 - [B0AZS6_HUMAN]	B0AZS6	1279.6444

Dynein light chain 1, cytoplasmic OS=Homo sapiens GN=DYNLL1 PE=1 SV=1 - [DYL1_HUMAN]	P63167	1282.6140
Caldesmon OS=Homo sapiens GN=CALD1 PE=1 SV=3 - [CALD1_HUMAN]	Q05682	1288.7079
-	No protein ID	1290.6903
Dihydropyrimidinase-related protein 3 (Fragment) OS=Homo sapiens GN=DPYSL3 PE=4 SV=1 - [H0YBT4_HUMAN]	H0YBT4	1295.7588
Serum albumin OS=Homo sapiens GN=ALB PE=1 SV=2 - [ALBU_HUMAN]	P02768	1296.7070
Isoform 2 of Tropomyosin beta chain OS=Homo sapiens GN=TPM2 - [TPM2_HUMAN]	P07951-2;P07951-3;P67936;P67936-2	1298.7695
Apolipoprotein A-I OS=Homo sapiens GN=APOA1 PE=1 SV=1 - [APOA1_HUMAN]	P02647;Q09666	1301.6489
Gamma-synuclein OS=Homo sapiens GN=SNCG PE=4 SV=1 - [F8W754_HUMAN]	F8W754	1302.6076
Isoform 2 of Tropomyosin beta chain OS=Homo sapiens GN=TPM2 - [TPM2_HUMAN]	P07951-2	1302.6469
Serum albumin OS=Homo sapiens GN=ALB PE=1 SV=2 - [ALBU_HUMAN]	P02768	1311.7419
Biglycan OS=Homo sapiens GN=BGN PE=2 SV=1 - [A6NLG9_HUMAN]	A6NLG9	1312.7457
Peptidyl-prolyl cis-trans isomerase FKBP1A OS=Homo sapiens GN=FKBP1A PE=1 SV=2 - [FKB1A_HUMAN]	P62942	1314.6648

Hemoglobin subunit beta OS=Homo sapiens GN=HBB PE=1 SV=2 - [HBB_HUMAN]; Hemoglobin subunit delta OS=Homo sapiens GN=HBD PE=1 SV=2 - [HBD_HUMAN]	P68871	1314.6648
Tropomyosin 1 (Alpha) isoform 3 OS=Homo sapiens GN=TPM1 PE=3 SV=1 - [D9YZV3_HUMAN]	D9YZV8;P09493-3;D9YZV3;P09493-7;Q6ZN40	1314.7644
-	No protein ID	1316.7423
Vitamin D-binding protein OS=Homo sapiens GN=GC PE=1 SV=1 - [VTDB_HUMAN]	P02787	1317.5938
Calmodulin OS=Homo sapiens GN=CALM1 PE=1 SV=2 - [CALM_HUMAN]	P62328	1320.5981
Isoform 3B of Myosin light chain kinase, smooth muscle OS=Homo sapiens GN=MYLK - [MYLK_HUMAN]	Q15746-4	1321.7271
Histone H4 OS=Homo sapiens GN=HIST1H4A PE=1 SV=2 - [H4_HUMAN]	P62805	1325.7544
Histone H4 OS=Homo sapiens GN=HIST1H4A PE=1 SV=2 - [H4_HUMAN]	P62805	1325.7544
Hemoglobin subunit delta OS=Homo sapiens GN=HBD PE=1 SV=2 - [HBD_HUMAN]	P02042	1326.8023
Isoform 2 of Tropomyosin beta chain OS=Homo sapiens GN=TPM2 - [TPM2_HUMAN]	P09493-3;D9YZV3;P07951-2;Q6ZN40	1332.6404
Thioredoxin OS=Homo sapiens GN=TXN PE=4 SV=1 - [B1ALW1_HUMAN]	B1ALW1	1336.6468
Extracellular superoxide dismutase [Cu-Zn] OS=Homo sapiens GN=SOD3 PE=1 SV=2 - [SODE_HUMAN]	P08294	1337.6842

Caldesmon OS=Homo sapiens GN=CALD1 PE=1 SV=3 - [CALD1_HUMAN]	Q05682	1340.5935
Caldesmon OS=Homo sapiens GN=CALD1 PE=1 SV=3 - [CALD1_HUMAN]	Q05682	1341.6421
Serum albumin OS=Homo sapiens GN=ALB PE=1 SV=2 - [ALBU_HUMAN]	P02768	1342.6432
Isoform 2 of Tropomyosin beta chain OS=Homo sapiens GN=TPM2 - [TPM2_HUMAN]	P07951-2	1343.6826
Tubulin-specific chaperone A OS=Homo sapiens GN=TBCA PE=4 SV=1 - [E5RIW3_HUMAN]	E5RIW3	1347.7383
Apolipoprotein A-IV OS=Homo sapiens GN=APOA4 PE=1 SV=3 - [APOA4_HUMAN]	P06727	1352.6584
Actin, gamma-enteric smooth muscle OS=Homo sapiens GN=ACTG2 PE=1 SV=1 - [ACTH_HUMAN]; Nuclease-sensitive element-binding protein 1 OS=Homo sapiens GN=YBX1 PE=1 SV=3 - [YBOX1_HUMAN]	P63267; P60709	1354.6181
Serum albumin OS=Homo sapiens GN=ALB PE=1 SV=2 - [ALBU_HUMAN]	P02768	1358.6228
Caldesmon OS=Homo sapiens GN=CALD1 PE=1 SV=3 - [CALD1_HUMAN]	Q05682	1358.6551
Isoform 2 of Nucleophosmin OS=Homo sapiens GN=NPM1 - [NPM_HUMAN]	P06748-2	1360.6737
-	No protein ID	1364.6450
-	No protein ID	1365.6618
-	No protein ID	1373.6362

Isoform 2 of Collagen alpha-1(IV) chain OS=Homo sapiens GN=COL4A1 - [CO4A1_HUMAN]	P02462-2	1373.6429
Uncharacterized protein C6orf163 OS=Homo sapiens GN=C6orf163 PE=1 SV=2 - [CF163_HUMAN]	Q5TEZ5	1373.6429
-	No protein ID	1373.6538
Isoform 2 of Tropomyosin beta chain OS=Homo sapiens GN=TPM2 - [TPM2_HUMAN]	P07951-2;P07951-3	1374.6014
Hemoglobin subunit beta OS=Homo sapiens GN=HBB PE=1 SV=2 - [HBB_HUMAN]; Hemoglobin subunit delta OS=Homo sapiens GN=HBD PE=1 SV=2 - [HBD_HUMAN]	P68871	1378.7015
-	No protein ID	1392.6527
Caldesmon OS=Homo sapiens GN=CALD1 PE=1 SV=3 - [CALD1_HUMAN]	Q05682	1395.6107
-	No protein ID	1406.6687
Transgelin OS=Homo sapiens GN=TAGLN PE=1 SV=4 - [TAGL_HUMAN]	Q01995	1408.6737
60S ribosomal protein L4 (Fragment) OS=Homo sapiens GN=RPL4 PE=4 SV=1 - [H3BU31_HUMAN]	H3BU31	1415.7466
-	No protein ID	1415.7553
Calponin-1 OS=Homo sapiens GN=CNN1 PE=1 SV=2 - [CNN1_HUMAN]	P51911	1417.6506
Cystatin-B OS=Homo sapiens GN=CSTB PE=1 SV=2 - [CYTB_HUMAN]	P04080	1422.7149
Transgelin OS=Homo sapiens GN=TAGLN PE=1 SV=4 - [TAGL_HUMAN]	Q01995	1424.6697

N-terminal form OS=Homo sapiens GN=SOGA1 PE=4 SV=1 - [J3KN88_HUMAN]	J3KN88	1430.6572
Hemoglobin subunit delta OS=Homo sapiens GN=HBD PE=1 SV=2 - [HBD_HUMAN]	P02042	1441.6806
Hemoglobin subunit beta OS=Homo sapiens GN=HBB PE=1 SV=2 - [HBB_HUMAN]; Hemoglobin subunit delta OS=Homo sapiens GN=HBD PE=1 SV=2 - [HBD_HUMAN]	P68871;P02042	1449.7960
Cytochrome c OS=Homo sapiens GN=CYCS PE=1 SV=2 - [CYC_HUMAN]	P99999	1449.7960
-	No protein ID	1465.6905
Serum albumin OS=Homo sapiens GN=ALB PE=1 SV=2 - [ALBU_HUMAN]	P02768	1467.8448
Isoform 2 of Tropomyosin beta chain OS=Homo sapiens GN=TPM2 - [TPM2_HUMAN]	P07951-2	1471.7750
Tubulin-specific chaperone A OS=Homo sapiens GN=TBCA PE=4 SV=1 - [E5RIW3_HUMAN]	E5RIW3	1481.6736
Rho GDP-dissociation inhibitor 2 (Fragment) OS=Homo sapiens GN=ARHGDIB PE=4 SV=1 - [F5H2R5_HUMAN]	F5H2R5	1481.8539
Histone H4 OS=Homo sapiens GN=HIST1H4A PE=1 SV=2 - [H4_HUMAN]	P62805	1481.8539
Histone H1.3 OS=Homo sapiens GN=HIST1H1D PE=1 SV=2 - [H13_HUMAN]	P16402	1482.8597
Actin, gamma-enteric smooth muscle OS=Homo sapiens GN=ACTG2 PE=1 SV=1 - [ACTH_HUMAN]; Nuclease-sensitive	P63267	1501.7334

element-binding protein 1 OS=Homo sapiens GN=YBX1 PE=1 SV=3 - [YBOX1_HUMAN]		
Serum albumin OS=Homo sapiens GN=ALB PE=1 SV=2 - [ALBU_HUMAN]	P02768	1511.8435
Hemoglobin subunit alpha OS=Homo sapiens GN=HBA1 PE=1 SV=2 - [HBA_HUMAN]; HCG1745306, isoform CRA_a OS=Homo sapiens GN=HBA2 PE=3 SV=1 - [G3V1N2_HUMAN]; SWISS-PROT:P01966 (Bos taurus) Hemoglobin subunit alpha	P69905	1529.7363
-	No protein ID	1536.7358
Serum albumin OS=Homo sapiens GN=ALB PE=1 SV=2 - [ALBU_HUMAN]	P02768	1546.7971
Protein S100-A8 OS=Homo sapiens GN=S100A8 PE=1 SV=1 - [S10A8_HUMAN]	P05109	1549.8033
Hemoglobin subunit delta OS=Homo sapiens GN=HBD PE=1 SV=2 - [HBD_HUMAN]	P02452	1553.7710
Histone H1.2 OS=Homo sapiens GN=HIST1H1C PE=1 SV=2 - [H12_HUMAN]	P16403	1558.7145
Collagen alpha-2(I) chain OS=Homo sapiens GN=COL1A2 PE=1 SV=7 - [CO1A2_HUMAN]	P08123	1562.7888
-	No protein ID	1567.7557
-	No protein ID	1569.7840
Non-histone chromosomal protein HMG-17 OS=Homo sapiens GN=HMGN2 PE=1 SV=3 - [HMGN2_HUMAN]	P05204	1584.9480

Isoform 2 of High mobility group nucleosome-binding domain-containing protein 3 OS=Homo sapiens GN=HMGN3 - [HMGN3_HUMAN]	Q15651-2	1612.9514
Ferritin heavy chain OS=Homo sapiens GN=FTH1 PE=1 SV=2 - [FRIH_HUMAN]	P02794	1627.7567
Serum albumin OS=Homo sapiens GN=ALB PE=1 SV=2 - [ALBU_HUMAN]	P02768	1639.7832
Serum albumin OS=Homo sapiens GN=ALB PE=1 SV=2 - [ALBU_HUMAN]	P02768; P02769	1639.9398
Hemoglobin subunit beta OS=Homo sapiens GN=HBB PE=1 SV=2 - [HBB_HUMAN]; Hemoglobin subunit delta OS=Homo sapiens GN=HBD PE=1 SV=2 - [HBD_HUMAN]	P68871; P02042	1669.8888
Vitamin D-binding protein OS=Homo sapiens GN=GC PE=1 SV=1 - [VTDB_HUMAN]	P02787	1706.7718
Alpha-1-acid glycoprotein 1 OS=Homo sapiens GN=ORM1 PE=1 SV=1 - [A1AG1_HUMAN]	P02763	1708.8493
Serum albumin OS=Homo sapiens GN=ALB PE=1 SV=2 - [ALBU_HUMAN]	P02768	1714.7916
-	No protein ID	1728.7861
Isoform 4 of Protein phosphatase 1 regulatory subunit 12B OS=Homo sapiens GN=PPP1R12B - [MYPT2_HUMAN]	O60237-4	1742.7350
Histone H2B type 1-M OS=Homo sapiens GN=HIST1H2BM PE=1 SV=3 - [H2B1M_HUMAN]	Q99879	1743.8147
Caldesmon OS=Homo sapiens GN=CALD1 PE=1 SV=3 - [CALD1_HUMAN]	Q05682	1748.8784

Histone H2B type 1-O OS=Homo sapiens GN=HIST1H2BO PE=1 SV=3 - [H2B1O_HUMAN]; Histone H2B type 1-K OS=Homo sapiens GN=HIST1H2BK PE=1 SV=3 - [H2B1K_HUMAN]	P23527; O60814	1751.0484
Caldesmon OS=Homo sapiens GN=CALD1 PE=1 SV=3 - [CALD1_HUMAN]	Q05682	1775.8205
Zinc-alpha-2-glycoprotein OS=Homo sapiens GN=AZGP1 PE=1 SV=2 - [ZA2G_HUMAN]	P25311	1775.8817
Actin, gamma-enteric smooth muscle OS=Homo sapiens GN=ACTG2 PE=1 SV=1 - [ACTH_HUMAN]; Nuclease-sensitive element-binding protein 1 OS=Homo sapiens GN=YBX1 PE=1 SV=3 - [YBOX1_HUMAN]	P63267;P60709	1790.8913
Isoform 2 of Tropomyosin beta chain OS=Homo sapiens GN=TPM2 - [TPM2_HUMAN]	P07951-2;P07951-3;O60237-4	1794.9059
Extracellular superoxide dismutase [Cu-Zn] OS=Homo sapiens GN=SOD3 PE=1 SV=2 - [SODE_HUMAN]	P08294	1832.8567
Hemoglobin subunit alpha OS=Homo sapiens GN=HBA1 PE=1 SV=2 - [HBA_HUMAN]; HCG1745306, isoform CRA_a OS=Homo sapiens GN=HBA2 PE=3 SV=1 - [G3V1N2_HUMAN]; SWISS-PROT:P01966 (Bos taurus) Hemoglobin subunit alpha	P69905;G3V1N2	1833.8869
Hemoglobin subunit alpha OS=Homo sapiens GN=HBA1 PE=1 SV=2 - [HBA_HUMAN]; HCG1745306, isoform CRA_a OS=Homo sapiens GN=HBA2 PE=3 SV=1 - [G3V1N2_HUMAN]; SWISS-PROT:P01966 (Bos taurus) Hemoglobin subunit alpha	P69905; G3V1N2; P01966	1833.8897
-	No protein ID	1833.9027

Cysteine and glycine-rich protein 1 OS=Homo sapiens GN=CSRP1 PE=1 SV=3 - [CSRP1_HUMAN]	P21291	1842.8818
Transgelin OS=Homo sapiens GN=TAGLN PE=1 SV=4 - [TAGL_HUMAN]	Q01995	1849.9326
Calmodulin OS=Homo sapiens GN=CALM1 PE=1 SV=2 - [CALM_HUMAN]	P62158	1871.8496
-	No protein ID	1888.8941
-	No protein ID	1902.8692
Caldesmon OS=Homo sapiens GN=CALD1 PE=1 SV=3 - [CALD1_HUMAN]	Q05682	1912.8169
Fibrinogen beta chain OS=Homo sapiens GN=FGB PE=1 SV=2 - [FIBB_HUMAN]	P02675	1951.0053
-	No protein ID	1955.8788
Lactoylglutathione lyase OS=Homo sapiens GN=GLO1 PE=1 SV=4 - [LGUL_HUMAN]	Q04760	1962.9837
-	No protein ID	2022.9396
Collagen alpha-2(I) chain OS=Homo sapiens GN=COL1A2 PE=1 SV=7 - [CO1A2_HUMAN]	P08123	2027.0262
-	No protein ID	2057.9748
Desmin OS=Homo sapiens GN=DES PE=1 SV=3 - [DESM_HUMAN]	P17661	2088.0874
Caldesmon OS=Homo sapiens GN=CALD1 PE=1 SV=3 - [CALD1_HUMAN]	Q05682	2097.9670
-	No protein ID	2101.1501
-	No protein ID	2125.1267

Trypsin - Sus scrofa (Pig). - [TRYP_PIG]	P00761 SWISS-PROT:P00761	2212.1018

Supplementary Table 7 – Complete list of metabolite mass features found from MALDI-MSI in a minimum of three control and three thyroid hormone treated tadpoles that showed significant ($p<0.05$) difference between control and treatment tadpoles with corresponding putative identifications, if found. The medians ± median absolute deviations(MAD) are indicated for each treatment condition

Tissue	Observed m/z value	Median Peak Intensity of Control Tadpoles	MAD of Control Tadpoles	Median Peak Intensity of Treatment Tadpoles	MAD of Treatment Tadpoles	MWU p-value	Database Matched m/z value	Putative ID
brain	380.2911	102354	19890	42785	7089	0.014		
brain	483.1284	38077	4556	64761	10514	0.037	483.1286	Silychristin (C25H22O10) [M+H]+
brain	516.2845	49760	584	34172	3919	0.022	516.2851	glycerophosphoethanolamine (C24H48NO6P) [M+K]+
brain	603.5343	109165	8595	142495	11335	0.008	603.5347	1-acyl,2-alkylglycerol (C39H70O4) {M+H]+
brain	623.5033	172090	25055	217610	27660	0.031		
brain	630.1592	53613	2773	77336	13992	0.030		
brain	798.3834	73673	2842	83850	1125	0.037		
brain	799.2421	86882	4826	103769	12816	0.036		
brain	813.1205	123440	18604	140070	7970	0.045		
brain	813.6852	111480	38453	255785	132370	0.036	813.6844	SM(32:2) [M+H]+
brain	830.5176	265490	36240	186700	14010	0.037		
brain	835.652	383165	72970	205650	53060	0.036		
brain	836.6223	114050	1540	146070	16340	0.037		
brain	943.6536	157030	41550	213745	20215	0.020		
brain	973.5698	293750	12760	467560	51450	0.037		
brain	1001.4962	127460	11640	94384	8774	0.037		
eye	388.9161	30476	782	38039	351	0.037		

eye	459.2486	59897	3725	47360	4601	0.045	459.2482	PA(18:1) [M+Na]+
eye	476.3139	68145	6429	82523	3244	0.008		
eye	549.4901	393800	102060	524380	17700	0.037		
eye	577.5192	481505	204245	1152350	80750	0.014		
eye	655.1386	186995	27145	105975	13621	0.030	655.1405	Heme [M+K]+
eye	667.4297	126990	5270	100547	7343	0.014	667.4309	PA(32:2) [M+Na]+
eye	697.4257	66648	2809	51881	3324	0.037	697.4259	NAc-L4Y-amide [M+Na]+
eye	702.877	70744	5093	115795	27105	0.037		
eye	739.571	305600	99490	171415	57455	0.036	739.5724	SM(35:1) [M+Na]+
eye	760.4427	74980	9394	98430	3915	0.030		
eye	770.6097	177130	25880	113405	9895	0.030		
eye	785.6507	113130	9990	71451	10947	0.037		
eye	787.4686	190200	8655	154520	14760	0.020	787.4675	PA(40:6) [M+K]+
eye	801.5191	98529	3136	84659	5835	0.012	801.5195	PA(42:6) [M+K]+
eye	841.4774	138740	13300	83833	2381	0.030	841.4780	alkylglycerophosphoglycerols $C_{46}H_{75}O_9P$ [M+K]+
eye	842.5669	342615	78780	212160	44030	0.037	842.5670	PE(42:6) [M+Na]+
eye	876.5513	238680	89350	120940	34445	0.036	876.5514	PC(42:10) [M+Na]+
eye	927.5745	120710	16935	221570	32495	0.020		
eye	947.1254	241335	19685	122425	35299	0.030		
eye	989.5328	207165	12945	88396	8945	0.037		
eye	1009.5024	306980	85670	177590	44060	0.037		
eye	1011.5186	285520	30640	172765	33515	0.020		
eye	1025.4993	157220	39170	96505	5135	0.020		
eye	1176.5021	79108	4373	59549	6748	0.030		
eye	1538.1394	232840	30990	326380	13410	0.037		
liver	630.6198	182740	7530	60780	9462	0.037		
liver	655.139	496810	54440	223530	59950	0.037	655.1405	Heme [M+K]+

liver	755.5018	113530	9576	82295	7155	0.030	755.5011	DG(44:10) [M+K]+
liver	780.1589	235900	8155	175350	37540	0.020		
liver	786.5473	121335	7915	177140	23735	0.030		
liver	978.0882	117535	7525	68094	7953	0.030		
liver	979.5131	68017	1173	141355	12505	0.037		
liver	1009.4937	143910	21250	92121	9982	0.020		
notochord	332.967	1792800	385600	855595	114670	0.020		
notochord	354.9488	87917	18220	40079	5058	0.043		
notochord	364.9391	417180	98270	168050	30845	0.008		
notochord	549.4871	162860	57221	369355	138840	0.043		
notochord	577.5194	418955	101955	1067300	140200	0.022		
notochord	645.4857	47514	3747	59348	6692	0.043	645.4854	PA(33:1) [M+H]+
notochord	675.5435	468860	160565	166595	8935	0.045	675.5436	SM(30:1) [M+H]+
notochord	695.4631	256245	98400	682175	211270	0.031	695.4622	PA(36:5) [M+H]+
notochord	706.5356	894350	234600	1554500	183600	0.020		
notochord	706.539	1112950	75700	1328500	114600	0.045	706.5381	PC(30:0) [M+H]+
notochord	710.4931	58698	3781	99807	5508	0.020		
notochord	711.4341	332050	64220	1055650	118425	0.020	711.4362	PA(34:2) [M+K]+
notochord	723.4932	711445	179655	1787150	318950	0.031	723.4935	PA(36:2) [M+Na]+
notochord	728.5191	328700	61240	583225	59615	0.022	728.5201	PC(30:0) [M+Na]+
notochord	730.5767	189010	15820	123545	15850	0.014	730.5745	PE(36:1) [M+H]+
notochord	734.5687	2462150	734450	3817850	557900	0.045	734.5694	PC(32:0) [M+H]+
notochord	739.4666	1056260	342855	2477900	530300	0.020	739.4675	PA(36:2) [M+K]+
notochord	760.583	15648000	5029650	29902000	212000	0.036	760.5851	PC(34:1) [M+H]+
notochord	768.5524	376850	42945	689645	139540	0.020	768.5514	PE(38:4) [M+H]+
notochord	769.4772	180880	53990	330460	83890	0.022	769.4779	PG(34:2) [M+K]+
notochord	769.5604	339185	88745	569580	14960	0.022	769.5620	SM(36:1) [M+K]+
notochord	772.5267	1131250	260595	2403700	397550	0.045	772.5252	PE(38:5) [M+Na]+

notochord	774.5515	92862	11889	117180	16050	0.037		
notochord	774.6011	701360	102830	1776400	123200	0.031	774.6007	PE(38:1) [M+H]+
notochord	782.5681	6049800	660000	9649100	1582900	0.008	782.5670	PC(36:4) [M+H]+
notochord	784.555	618685	114040	900340	53280	0.037		
notochord	786.5988	4638000	297900	3749000	371900	0.022	786.6007	PC(36:2) [M+H]+
notochord	788.5662	171545	30665	116935	10150	0.030		
notochord	788.6171	1221920	585830	2108800	352400	0.031	788.6164	PC(36:1) [M+H]+
notochord	792.5549	345490	14630	290190	31670	0.037	792.5538	PE(40:6) [M+H]+
notochord	797.1785	123605	34325	322350	114045	0.030		
notochord	798.5406	4764300	465950	11963000	3353150	0.045	798.5408	PE(40:6) [M+Na]+
notochord	801.5436	188130	30040	357810	52670	0.020	801.5429	PA(44:8) [M+H]+
notochord	806.5683	3016950	737200	4354650	558150	0.045	806.5670	PC(38:6) [M+H]+
notochord	810.6009	1093750	115485	1588650	142400	0.008	810.6007	PC(38:4) [M+H]+
notochord	815.1353	134480	19990	267780	52820	0.037		
notochord	817.6467	105905	3275	183635	25325	0.030		
notochord	818.5743	207870	49110	147725	9600	0.036		
notochord	822.5405	1680350	391200	1012015	207245	0.045	822.5410	PC(36:3) [M+K]+
notochord	826.5724	409675	194555	984785	138915	0.043	826.5721	PE(42:6) [M+Na]+
notochord	828.5508	632930	38850	990380	124170	0.036	828.5514	PC(38:6) [M+Na]+
notochord	828.5554	544590	103730	962565	193535	0.036	828.5538	PC(40:9) [M+H]+
notochord	854.5676	172550	33570	264615	20885	0.036	854.5670	PC(42:10) [M+H]+
notochord	856.5811	143305	29323	229600	8910	0.037	856.5827	PC(40:6) [M+Na]+
notochord	856.5905	122905	1260	199890	7040	0.020		
notochord	882.5613	165115	16065	98153	18363	0.043	882.5621	PS(40:2) [M+K]+
notochord	890.4882	86829	6818	144810	27955	0.037	890.4872	Solanine [M+Na]+
notochord	899.5411	116640	42047	409120	151270	0.037	899.5410	PI(37:2) [M+K]+
notochord	947.55	499500	23155	894490	130720	0.030		
notochord	949.5662	346425	63885	845850	89250	0.030		

notochord	973.5669	269690	105985	985390	52425	0.030		
notochord	975.5831	186330	48400	439545	35295	0.030		
notochord	987.5082	440220	54500	220520	18970	0.037		
notochord	999.5861	71832	14785	271930	20720	0.030		
tail muscle	364.9373	231940	13210	179780	29230	0.037		
tail muscle	370.921	291570	122040	43849	4226	0.020		
tail muscle	424.0069	52777	6596	37817	4731	0.031		
tail muscle	433.9912	53869	9575	38190	1000	0.020		
tail muscle	465.9626	82563	24298	47168	3754	0.014		
tail muscle	497.9351	160395	45620	88255	15215	0.036		
tail muscle	499.9501	60071	6472	47522	5002	0.043		
tail muscle	516.0281	49747	6523	34992	3239	0.030	516.0269	4-Methoxyglucobrassicin [M+K]+
tail muscle	713.5002	247680	3680	166545	28045	0.030	713.4994	SM(32:1) [M+K]+
tail muscle	726.5048	64597	2081	57751	3456	0.037	726.5044	PC(32:4) [M+H]+
tail muscle	768.4923	260825	12120	221620	22910	0.045	768.4939	PC(32:2) [M+K]+
tail muscle	770.6072	163070	14260	119000	19020	0.037	770.6058	PC(36:2) [M+H]+
tail muscle	772.526	780285	33305	550880	91780	0.031	772.5252	PE(38:5) [M+Na]+
tail muscle	776.4626	210610	16820	119800	33933	0.037	776.4627	PE(36:5) [M+K]+
tail muscle	813.1729	101035	3795	74431	3425	0.030		
tail muscle	814.4772	166460	8620	102148	12876	0.020	814.4784	PC(36:7) [M+K]+
tail muscle	828.4973	437140	78220	252245	33615	0.036		
tail muscle	830.5138	401230	31760	266205	54105	0.036		
tail muscle	840.498	327980	57170	137300	42920	0.022		
tail muscle	852.4983	141915	12595	110775	14799	0.020		
tail muscle	858.5399	150240	13400	114330	2910	0.037	858.5410	PE(42:6) [M+K]+
tail muscle	866.5099	180220	21530	104390	27520	0.036	866.5097	PC(40:9) [M+K]+
tail muscle	876.4963	156655	8855	106850	26340	0.036	876.4940	PE(44:11) [M+K]+

tail muscle	891.572	129900	32864	190565	38800	0.045	891.5723	PI(O-36:0) [M+K]+
tail muscle	911.5394	117335	6770	136500	8165	0.030	911.5410	PI(38:4) [M+K]+
tail muscle	911.6807	212440	8990	69800	11492	0.037		
tail muscle	924.4091	311780	45620	143350	17540	0.022		
tail muscle	935.6864	87597	7200	62605	2118	0.030		
tail muscle	939.5706	173810	7200	277570	14980	0.020	939.5723	PI(40:3) [M+K]+
tail muscle	948.4107	202750	21260	88208	16477	0.037	948.4107	Cyanopeptolin S [M+Na]+
tail muscle	973.5516	1233100	190300	1596100	49300	0.037		
tail muscle	1162.5369	72032	15572	109960	1370	0.037		